University of Southampton

Faculty of Physical Sciences and Engineering

Electronics and Computer Science

ANALYSIS AND DESIGN OF SOI MEMS STEP UP VOLTAGE CONVERTERS

By Rachel Gleeson

Thesis for the degree of Doctor of Philosophy

October, 2013

UNIVERSITY OF SOUTHAMPTON

ABSTRACT

FACULTY OF PHYSICALS SCIENCES AND ENGINEERING

Doctor of Philosophy

ANALYSIS AND DESIGN OF SOI MEMS STEP UP VOLTAGE CONVERTERS

By Rachel Gleeson

Energy harvesting systems are becoming an increasingly popular area for research as they present themselves as a clean, renewable source of energy. There are currently some key design issues facing the development of these energy harvesting systems. In particular, these harvesters often produce relatively low voltages compared to the requirements of the intended application. For example, scientific apparatus aboard orbital satellites require relatively high voltage levels for operation (kV) but are powered from solar panels providing substantially lower output voltages (24 V). In contrast, for low power energy harvesting, such as micro scale vibration energy harvesters, a harvested voltage level of ≈0.5V is often required to power a low power sensor circuit which requires 2-5V.

Voltage multiplication is commonly achieved using charge pump multiplier circuits. However, these circuits are quite limited in both the range of multiplication (per unit area) and the maximum voltage level. This work aims to take advantage of a noticeable gap in the research field and is specifically targeted towards energy harvesting application areas

This thesis presents a comprehensive analysis of novel bi-stable and resonant MEMS voltage step-up converters. The operation is based on isolating the charge of a mechanically variable capacitor and varying the gap between the electrodes by an appropriate method of actuation force. As the electrode gap varies, so does the voltage level across the electrodes. In the case of the bi-stable devices, electrostatic actuation is employed while the resonant devices rely on ambient vibration force. These have been specifically designed for integration with static and vibration energy harvesters respectively.

Prototype devices were fabricated using a dicing-free Silicon-on-Insulator (SOI) process developed at the Southampton Nanofabrication Centre. For the bi-stable device, a maximum output voltage of 35.7V was measured, using a 100MΩ load resistance, from a 24V input voltage. Further improvements in the design of the MEMS variable capacitor can be made in order to increase the capacitance level of the devices while reducing the parasitic fringing capacitance. Optimisation of the MEMS device would enable the output to reach a level near the theoretical maximum limit set at 120V.

Contents

List of Figures

List of Tables

List of Abbreviations

3D	three dimensional
AC	alternating current
ABM	analogue behavioural model
BOX	buried oxide
DC	direct current
CMOS	complimentary metal-oxide-semiconductor
DRIE	deep reactive ion etch
FEM	finite element modelling
FNA	fuming nitric acid
HF	hydrofluoric acid
ICP	inductively controlled plasma
MEMS	micro-electro-mechanical systems
MOSFET	metal-oxide-semiconductor field-effect transistor
PCB	printed circuit board
PECVD	plasma-enhanced chemical vapour deposition
PR	photo resist
RF	radio frequency
RMS	root mean square
SAMPSON	self-aligned micro-machined polysilicon on nitride
sccm	standard cubic centimetre per minute
SEM	single electron microscope
SOI	silicon on insulator
SOG	silicon on glass
SoP	system on package
TEOS	tetraethyl orthosilicate
UV	ultra violet
VPE	vapour phase etch

List of Symbols

a	acceleration
A	electrode area
b	damping coefficient
$C_{coupling}$	coupling capacitance
C_{comb}	capacitance of comb structure
C_{jo}	junction capacitance
C_L	load capacitor
C_{MAX}	maximum capacitance of variable capacitor
C_{MEMS}	MEMS variable capacitor
C_{MIN}	minimum capacitance of variable capacitor
C_P	parasitic capacitance
C_{plate}	capacitance of parallel plate structure
C_S	stray capacitance
C_{var}	variable capacitor
D_s	density of silicon
ε_0	permittivity of free space
f_0	resonant frequency
f_{clk}	frequency of clock
f_{el}	electrostatic force
f_{el_comb}	electrostatic force of comb structure
f_{el_plate}	electrostatic force of parallel plate structure

f_{ext}	external force
g	electrode gap
g_0	electrode gap at rest position
g_{MAX}	maximum electrode gap
g_{MIN}	minimum electrode gap
h	thickness of structural layer
k	spring constant
m	mass
M	multiplication factor
$MEMS$	micro electro mechanical systems
N	number of electrodes
η	electrical efficiency
$\Phi, /\Phi$	non-overlapping signals
$P_{cap/act}$	power of capacitor/actuator
P_{out}	output power
Q	capacitor charge
R_L	load resistance
R_S	Thevenin equivalent source resistance
V	volume
V_{act}	actuator input voltage
V_{in}	input voltage
Vo	Thevenin equivalent output voltage

V_{out}	output voltage
$V_{pull\text{-}in}$	pull-in voltage
ω	angular frequency
x	electrode overlap distance
Y	amplitude of vibration

Declaration of Authorship

I, Rachel Gleeson declare that this thesis and the work presented in it are my own and has been generated by me as a result of my own original research.

Analysis and Design of SOI MEMS Step Up Voltage Converters

I confirm that:

1. This work was done wholly or mainly while in candidature for a research degree at this University
2. Where any part of this thesis has been previously submitted for a degree or any other qualification at this University of any other institution, this has been clearly stated
3. Where I have consulted published work of others, this is always clearly attributed
4. Where I have quoted from the work of others, the source is always given. With the exception of such quotations, this thesis is entirely my own work
5. I have acknowledges all main sources of help
6. Where the thesis is based on work done by myself jointly with others, I have made clear exactly what was done by others and what I have contributed myself
7. Either none of this work has been published before submission, or parts of this work have been published as: [please see references below]

Journal Publication:

1. R. Gleeson, M. Kraft and N. M. White "Design and analysis of an SOI MEMS step up voltage converter", **J. Mircomech. Microeng**, October 2013.

Conference Publication:

1. R. Gleeson, M. Kraft and N.M. White, "Design and analysis of two types of MEMS DC-DC step-up voltage converters", **Conf. Proc. MME**, Tønsberg, Norway, June 2011.
2. R. Gleeson, M. Kraft and N. M. White "Design and analysis of MEMS step up voltage converters", **Conf. Proc. IEEE Sensors**, Taipei, October 2012.

3. R. Gleeson, M. Kraft and N. M. White “Design and analysis of MEMS step up voltage converters”, **Conf. Proc. PowerMEMS**, Atlanta, December 2012.

Signed:

Date:

Acknowledgement

Apart from my own efforts, the success of any project depends largely on the encouragement and guidelines of many others. First and foremost, I would like to express my gratitude to my supervisors Professor Michael Kraft and Professor Neil White. Without their constant guidance and support, this thesis would not have been possible.

Also, I would like to take this opportunity to express my gratitude to my colleagues in the Nano research group who have been instrumental in the successful completion of this project. In particular I would like to thank Dr. Ibrahim Sari, Dr. Ioannis Karakonstantinos, Dr. Owain Clarke, Dr. Kian Kiang, Bader Almutairi, Ali Alshehri, Hwanjit Rattanasonti, Maria Theresa Gussad De Leon and Rares Bodnar. Special thanks are reserved for Dr. Feras Alkhalil, his help and encouragement has seen me through the toughest times of this thesis and made this one of the most enjoyable experiences I will ever have.

Last but not least, I would like to thank my parents and siblings for their unconditional support, both financially and emotionally throughout my degree. Their patience and understanding is greatly appreciated and I would have never made it this far without them.

Chapter 1 Introduction

1.1 Background and Motivation

As miniaturisation and portability of modern electronic devices becomes an increasingly popular area of development, so does the need for these devices to operate from a miniaturised, portable voltage source. In the past, battery technology would be the clear choice to power small electronic devices due to its ease of integration and commercial availability. However, even rechargeable batteries require eventual replacement and so this technology does not present itself as a permanent power solution. In addition to this, some electronic devices may be used for remote environment monitoring where regular replacement of batteries is not an option [1].

In recent times, environmental impact has become one of the most important considerations in the design of modern electronic systems. This has resulted in an increased research interest in the area of energy harvesting to create a fully self-sufficient power solution by eliminating the need for an external power source. Energy harvesters generate power from their surrounding environment [2].

Table 1-1 - Comparison of harvested power levels with the corresponding ambient source power level (after Vullers et al, 2009, [3]).

Source	Source Power	Harvested Power
Ambient Light		
Indoor	0.1mW/cm^2	10μW/cm^2
outdoor	100mW/cm^2	10mW/cm^2
Vibration/Motion		
Human	0.5m @1Hz 1m/s^2 @50Hz	4μW/cm^2
Industrial	1m @5Hz 10m/s^2 @1kHz	100μW/cm^2
Thermal Energy		
Human	20mW/cm^2	30μW/cm^2
Industrial	100mW/cm^2	1-10mW/cm^2
RF		
Cell phone	0.3μW/cm^2	0.1μW/cm^2

A reliable generator can remain functional for the entire lifetime of an electronic sensor node without the need for replacement, providing a long term solution to making a system self-sufficient [3]. An issue exists, however, in matching the supply voltage to the voltage level required for the intended application. These harvesters output relatively low voltages and are often cascaded in series to achieve the desired voltage range. To address these issues in voltage discrepancies, various voltage multiplication techniques for energy harvesting systems have been introduced [4-7].

Existing multiplier technology is quite limited in the range of multiplication it can achieve per unit area. Charge pump circuits are the most common multiplication technique used for voltage step-up conversion [8]. However several issues exist with these circuits. For Dickson charge pumps, the multiplication factor achieved by charge pumps depends on the number of capacitor stages cascaded in series. For higher levels of multiplication, the corresponding number of stages required increases as does the area requirement for that circuit becomes. In the case of MOSFET charge pump circuits, electrical breakdown is a limiting factor for the multiplication of high voltages while relatively high threshold voltages render them unsuitable for multiplication of low voltages (<0.5V).

Within the past two decades, a lot of research has been conducted in the field of micro-electro mechanical systems (MEMS). It is now possible to resolve issues that would have previously been impossible to achieve with standard design techniques. In particular, inertial sensors, such as accelerometers and gyroscopes, have received a significant amount of attention in recent years [9]. These sensors are becoming increasingly popular and are featured in many mainstream commercial electronic products today e.g. mobile phones, gaming consoles, laptops etc. In these devices, ambient acceleration causes a displacement in an internal suspended proof mass. In the case of a capacitive inertial sensor, this displacement of the proof mass results in a change in capacitance levels of the device. For this work, the same methodology of mechanically varying capacitance levels is investigated to create a new form of voltage multiplier.

There have been previous investigations [10-13] into MEMS voltage converter devices; however, these have remained mainly theoretical with few reports of prototype devices being fabricated. The theoretical analyses of these devices have provided the background theory for which the devices in this thesis are based. These papers also report issues that may affect the output voltage and electrical efficiency of fabricated end devices. In particular, parasitic

capacitance presents itself as a factor of significant attenuation in the output voltage of the converters [12]. The fabrication of converter devices using an SOIMUMPS process has previously been presented [13]. However, little information was reported with regards to the impact of parasitic elements, electrical efficiency etc.

1.2 Objectives

This work presents MEMS voltage step up converters based on a mechanically variable capacitor. By maintaining a constant charge, Q, across the capacitor and decreasing the capacitance, C, the voltage, V, across the capacitor will then increase ($Q=C*V$). This decrease in capacitance is achieved by increasing the gap between electrodes through some form of mechanical actuation.

This work aims to take advantage of a noticeable gap in this research field by presenting fabricated devices which are specifically targeted towards integration with energy harvesting applications. Two core voltage conversion devices are presented in this thesis; a bi-stable and a resonant device. The key difference between these devices is the method of mechanical actuation of the capacitor electrode gap. The bi-stable device uses a separate electrostatic actuator element while the resonant device uses the force generated from ambient vibrations. The use of ambient vibrations to vary capacitance is common practice in the design of accelerometers, gyroscopes and capacitive energy harvesters; however, the concept of voltage multiplication is a novel re-imagining of a capacitive energy harvester. The bi-stable and resonant devices have been specifically designed for the purpose of integration with static and vibration energy harvesters respectively. As vibration energy harvesters tend to generate low power levels, the lack of an electrostatic actuating element in the resonant converter design should increase the overall electrical efficiency of the system.

Further novel contributions are demonstrated in the design of modified versions of each core device. The modified bi-stable device features a curved beam zipping actuator to generate an electrostatic force/electrode displacement from a lower driving voltage than in the case of a conventional parallel plate actuator. The advantage of using such an actuator is to allow for an increase in capacitance area/force without the need to proportionally increase the area of the actuation element. While the standard bi-stable design has been presented in previous

published articles related to this work, a zipping actuator has not been considered until this point. This structure can solve the issue of low capacitance levels per unit area in the core design.

The modified resonant device features additional enhancements over the core resonant devices. The principal innovative change, however, is the introduction of integrated ohmic MEMS switches are introduced. This is a unique approach in overcoming the issue of diode parasitic capacitance in the control circuit. Other minor improvements have also been made e.g. increased capacitance level.

The key challenges lie in designing converters that can meet the low voltage, high efficiency requirements of the energy harvesters while maintaining the highest possible multiplication factor. Energy harvesters tend to generate low levels of power and therefore, it is of the utmost importance that the end devices are designed to exhibit high levels of power efficiency and relatively low levels of parasitic capacitance to compete with charge pump circuits. This is the focus of this research.

The innovative designs presented in this thesis are fabricated using a dicing free SOI process and their performance is evaluated.

1.3 Document Structure

A comprehensive review of the literature relevant to this work is presented in chapter 2. This review chapter reports on various energy harvesting systems and the current multiplication techniques employed to convert the output voltage to a higher level required for the intended applications. This chapter also refers to papers detailing the optimization of the control circuitry required to control the charging/discharging of the MEMS variable capacitor converter in addition to previous studies on the design of the MEMS converter. These previous studies are essential to the design of the devices in this work presented in this thesis.

Chapters 3 and 4 describe the theoretical work carried out to develop the bi-stable and resonant converter devices respectively. Initial introductory background theory is provided for each design and device parameters are optimised through system level Simulink modelling. A 3D model was then created using MEMS+ software and finite element

modelling (FEM) simulations were carried out using Coventorware. These models provide the patterns for mask design and prototype development. The design of the control circuit for the MEMS variable capacitor is also detailed in these chapters. Using a similar mass-spring-damper system block as in the Simulink model, and including parasitic capacitances found from the FEM simulations, it was possible to develop an accurate circuit level representation of the MEMS converter in Multisim. This enables the simulation of output voltage and electrical efficiency.

Chapter 5 presents fabrication process flow for the development of the prototype converter devices. This fabrication was conducted using a well-established Silicon-On-Insulator (SOI) process developed at the University of Southampton's Nano Fabrication Centre. This is a unique dicing free processes where the devices are etched from the wafer using a HF vapour phase etch. The silicon handle wafer under the suspended devices is also removed in an effort to reduce parasitic capacitances between the capacitive structure and the handle layer.

The evaluation of the bi-stable and resonant devices is reported in chapters 6. Initial characterisation was carried out using PolyTech's MSA-400. A CV analysis of the devices was then conducted using an Agilent 4279A CV analyser. Finally the devices were integrated into a control circuit and the output voltage and electrical efficiency was measured.

Chapter 7 concludes the work presented and offers suggestions for how this work may be progressed for future work and development.

Chapter 2 MEMS Voltage Converters: A Comprehensive Review

2.1 Introduction

A self-sufficient system is one which produces an output without the need for an external input. Generally they are comprised of an energy harvester generating a voltage from ambient energy, e.g. vibration, and a multiplier to increase this voltage to a useable level. To date multiplication has been provided through the use of charge pump circuits [16-21]. However, these circuits offer low levels of energy density per unit area. This work aims to optimise the self-sufficient system by replacing the multiplier unit with a MEMS device.

MEMS voltage converter operation is based on a mechanically variable capacitor. When the capacitor is held at a constant charge and the electrodes are separated to a distance of minimum capacitance, the voltage across the capacitor will increase, $Q=CV$. The force required to separate the electrodes has been electrostatic in the case of previous investigations into these devices, however, capacitive vibration harvesters use ambient vibrations to provide the actuation force [11-15] which provides an alternative actuation method which uses less energy. MEMS converters have the advantage of being single stage devices, easily fabricated using an SOI process and can multiply a wide range of voltage inputs, including low voltages (≈0.5V).

In addition to the MEMS device, a suitable control circuit must also be implemented to achieve the maximum energy efficiency and output voltage of the system. A typical layout of such a control circuit is given in figure 2-1. The variable capacitor (C_{MEMS}) is charged from the input voltage V_{in}. The diodes D1 and D2 isolate the variable capacitor from the RC load circuit. This prevents the load capacitor from back charging the variable capacitor. The parasitic capacitor C_P is related to the capacitive fringing fields of the variable capacitor as

discussed in [4]. This circuit alternates between charging the capacitor and discharging to the load after the electrodes have been separated.

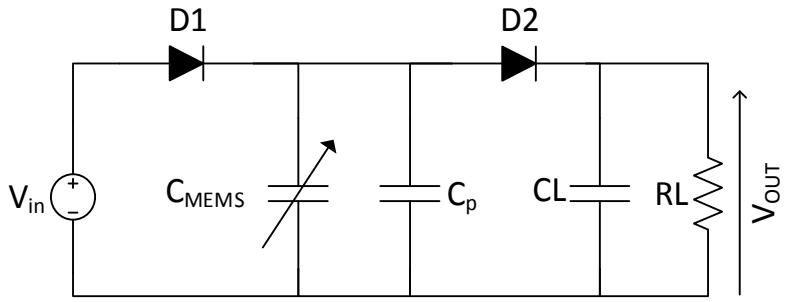

Figure 2-1 MEMS voltage converter circuit. C_{MEMS} is the mechanically varying capacitor and C_P is the parasitic capacitance. Diodes D1 and D2 isolate the charge on the capacitor.

This chapter serves to provide a complete review of the background research that has previously been conducted in all areas relevant to this work.

2.2 Energy Harvesting

The focus of this work is to integrate the voltage multipliers presented in this report, with energy harvesting devices. Energy harvesting systems convert ambient energy to electrical energy. A comprehensive review of energy sources which can be harvested is given in [14]. Energy harvesting systems can generally be classed into two groups, static harvesters, which feature no mechanical moving parts and vibration harvesters which convert kinetic energy to electrical energy. These harvesters produce a maximum power level at their resonant frequency.

2.2.1. Static Harvesters

Static energy harvesters do not feature moveable mechanical structures. These systems generate electrical energy from ambient sunlight and temperature variation using solar cell panels and thermoelectric generators.

Thermoelectric generators convert temperature differences to electrical energy through the “Seebeck effect”. Current will flow when there is a temperature difference between two connected, dissimilar conductors. In general the greater the temperature difference, the

greater the current generated. A review of thermoelectric generator theory and applications is presented in [15]. Typically these generators are used to convert wasted heat to electricity [16, 17]. The efficiencies of these generators are also quite low (5-10%) [18]. However, efforts are being made to increase the efficiency of these generators [19].

A solar cell converts energy from sunlight into electricity by the photovoltaic effect. When a P-N junction is exposed to light, the electrons within the p-side absorb the photon energy from the light and move to the n-side causing a movement of holes to the p-side. While the conversion efficiency of solar cells is relatively low (≈30%) [20, 21], they can provide higher levels of power density compared to other forms of energy harvesters as can be seen in table 1-1**Error! Reference source not found.**. As such, they are the most popular choice for power generation in areas that exhibit reasonable levels of sunshine.

Advances are constantly being made in solar cell materials in order to improve the electrical efficiency. The first solar cell produced in 1941 produced an efficiency of only 1% [22]. Substantial improvements in silicon cell performance resulted in an increase to 28% by 2011 [23].

Solar cells are also attractive as power sources for MEMS since they are easily integrated and, therefore, can be fabricated as a self-contained on-board power supply. In addition, solar cells are very well characterized and developed in many industrial and commercial applications. However, solar cells often require to be cascaded in series to reach the output voltage levels required for voltage applications such as supplying power to the electric grid (220V) [24] or powering high voltage scientific apparatus on-board orbital satellites (+/-15kV) [25] . A typical solar cell configuration will output 12-24V and so a significant level of amplification is required for these high voltage applications. In this thesis, the bi-stable voltage converter will be designed specifically for multiplying the same level of output voltage as normally produced by a solar cell harvester (24V).

2.2.2. Vibration Harvesters

In cases where it is not feasible to use optical or thermal energy harvesters due to environmental constraints, vibration energy harvesters can be employed to convert mechanical energy into electrical energy. Piezoelectric, electromagnetic and electrostatic energy harvesters all convert energy from ambient vibrations to electrical energy through the movement of a mechanical component within the structure.

Piezoelectric materials produce electrical signals under mechanical stress (and vice versa) due to the induced polarization, by a strong electric field, of the ferroelectric material. Piezoelectric generators are the most commonly researched of all these structures due to this inherent mechanical-electrical domain coupling. In addition to this, these generators require no external pre-charging voltage, unlike electrostatic generators, and their energy density scales well with size, unlike electromagnetic generators [26-30]. Due to the high energy density of piezoelectric materials, they typically do not require any addition voltage step-up conversion.

If a magnetic mass is moved relative to a coil, a voltage is induced through the coil. This is the basic principle of operation of electromagnetic vibration harvesters. A simplified model of these generators is shown in figure 2-2 below.

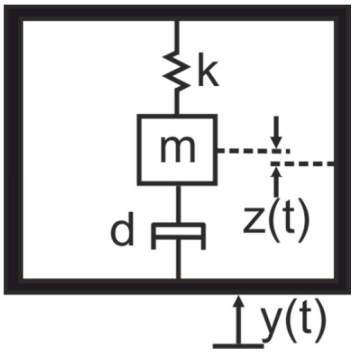

Figure 2-2 Simple mass-spring-damper model of an electromagnetic generator (after Williams and Yates, 1996, [31])

External vibrations on the generator frame cause the mass to oscillate relative to the frame. This mass can be tuned to resonant at the same frequency as the average frequency of the ambient vibrations using the following formula:

$$f_0 = \frac{1}{2\pi}\sqrt{\frac{k}{m}} \qquad 2\text{-}1$$

Maximum power transfer occurs at the resonant frequency of these devices [31]. These generators will produce much more power in areas where there is high frequency of vibration as the generated power is proportional to the cube of the vibration frequency. To design for maximum power generation, the mass should be made as large as possible, the maximum displacement of the mass should also be as large as possible, the spring should be designed according to resonant frequency matching and the load impedance should be designed to give

a low enough damping factor to maximise mass displacement. For applications where a continuous supply is required, the harvester must output a minimum of 0.1mW; otherwise it would only be suitable to trickle charge a battery for later use.

Optimum damping and load conditions are explored for generator design in [32]. A macro-sale model was then constructed to test these conditions. It was shown that, in addition to allowing the device to oscillate at it resonant frequency, by setting the parasitic damping to equal the normal mechanical damping of the system, maximum power output can be achieved. A generator based on this analysis is then fabricated in [33]. A 3D layout of this generator is shown in figure 2-3.

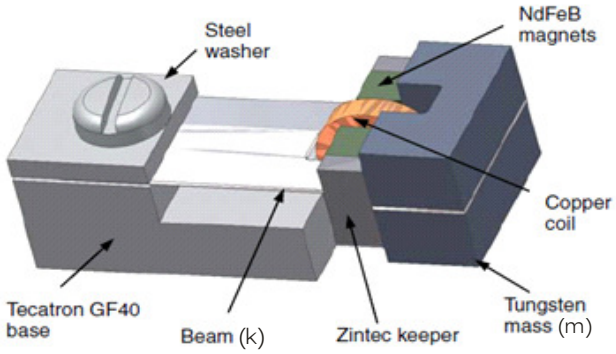

Figure 2-3 Micro scale cantilever generator using NdFeB magnets to induce a current in the copper coil. The base holds the spring beam, *k*, which is connected to the tungsten mass, *m*. (after Beeby et al, 2007, [33])

This micro scale "VIBES" generator is 0.15cm^3. For 53Hz, the recorded voltage output is 428mVrms based on load resistance of 4kΩ and an ambient acceleration of 3.7ms^{-2}. The output voltage produced by this device is too low to power even low voltage circuits independently. This is an ideal example of an energy harvesting system which requires a multiplication circuit to amplify the output voltage to a level where it can power an IC circuit (≈2V). As such, this generator will provide the basis of the vibration energy harvester supply for the resonant voltage converter design presented in this thesis.

Following on from this design, a 0.1cm^3 generator was designed in [34]; however, the maximum output voltage was recorded as ≈8.5mVrms at a similar frequency as output voltage scales with the dimensions of the harvester. A review of current electromagnetic energy harvesting devices is found in [35]

Electrostatic energy harvesters are based on a mechanically variable capacitor [36]. Ambient vibrations provide the necessary force to vary the gap between the electrodes. When a capacitor is charged, the plates are separated and when the capacitor reaches its minimum capacitance position, the voltage is transferred to a load, this is based on the fundamental capacitor-charge equation $Q=C*V$. Clearly these devices are not fully autonomous energy harvesters as an initial charge is required for the capacitor to initiate the voltage transfer. This involves the use of an external voltage source (typically a battery). An example of such a system is given in figure 2-4. Similar devices are presented in [37-40] featuring different capacitor and control circuit designs.

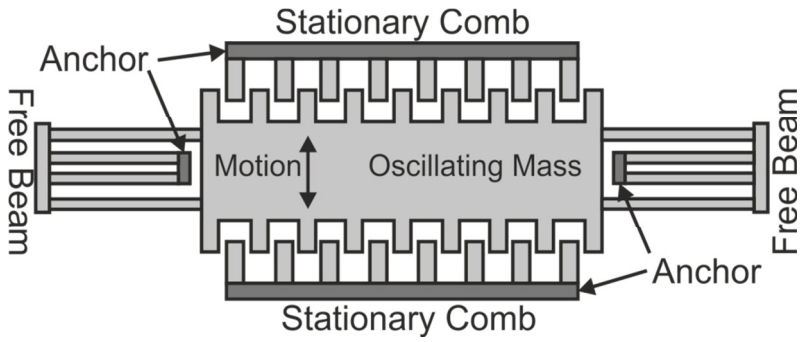

Figure 2-4 Capacitive harvester device. The oscillating mass moves with vibration, varying the capacitance of the comb drives and increasing voltage (after Meninger et al, 2001, [34])

2.3 Voltage Multiplication Techniques

The previous section in this review detailed a variety of energy harvesting methods. The need for a voltage multiplication circuit is obvious in the case of electromagnetic harvesters which often output voltages too low for their intended application (≈0.5V). However, even with solar cells, which feature the highest levels of energy density per unit area, voltage multiplication circuits are necessary for high voltage applications. This section investigates current methods employed to step-up the voltage from energy harvesting systems.

2.3.1. Voltage Converters for Energy Harvesters

In its simplest form, an energy harvesting circuit consists of a rectifier circuit to convert an AC output voltage to a DC voltage, a DC-DC converter to boost the DC voltage and a storage

element such as a capacitor or battery which delivers continuous power to the intended application device. A block diagram representing a converter system is shown in figure 2-5.

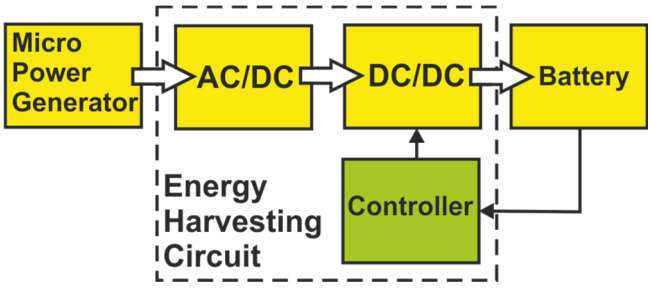

Figure 2-5 Energy harvesting circuit block diagram (after Priya and Inman, 2008, [41])

Charge pumps and boost converters, made from discrete electronic components, are the most commonly DC-DC converter circuit for energy harvesting systems. Charge pumps operate by pumping charge along a chain of capacitors during alternating. A boost converter typically uses an inductor to charge a switched capacitor and boost the output voltage. The uses of boost converters for energy harvesting systems is well documented [42-45] often providing relatively high electrical efficiencies through the use of a MOSEFT and crystal oscillator in place of the switch component. However, the inductor element make these devices less appealing, in terms of miniaturisation, than their charge pump counterparts and, therefore, charge pumps will be the focus of this section.

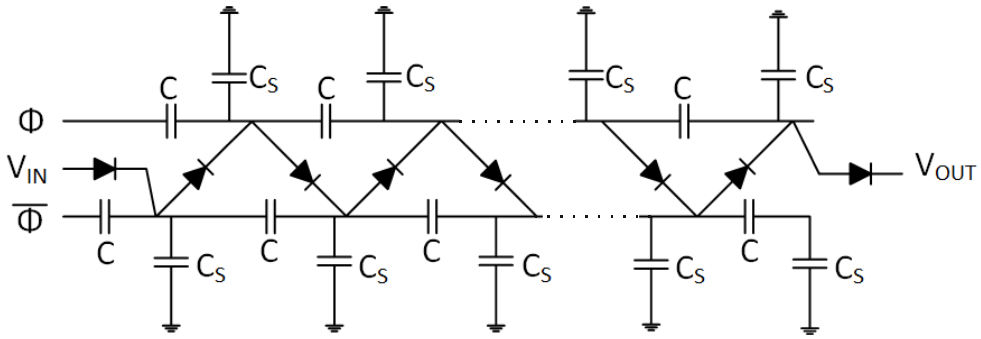

Figure 2-6 Basic Cockcroft-Walton voltage multiplier (after Dickson, 1976, [46])

The original charge pump was developed by Cockcroft and Walton for use in their particle accelerator research. In this circuit, shown in figure 2-6, the active clock signal charges up the relevant coupling capacitors and passes this charge down the diode chain. The greater number of stages, the greater the multiplication of the input voltage V_{IN}. However, a critical number of stages exist for this multiplier which is determined by the ratio of coupling capacitance C

to the stray capacitance C_s. If the number of stages is increased beyond this critical number, the output ceases to increase and actually drops due to the voltage drop across the diodes. To rectify this issue a variation on this multiplier is presented in [46] and is shown in figure 2-7 below.

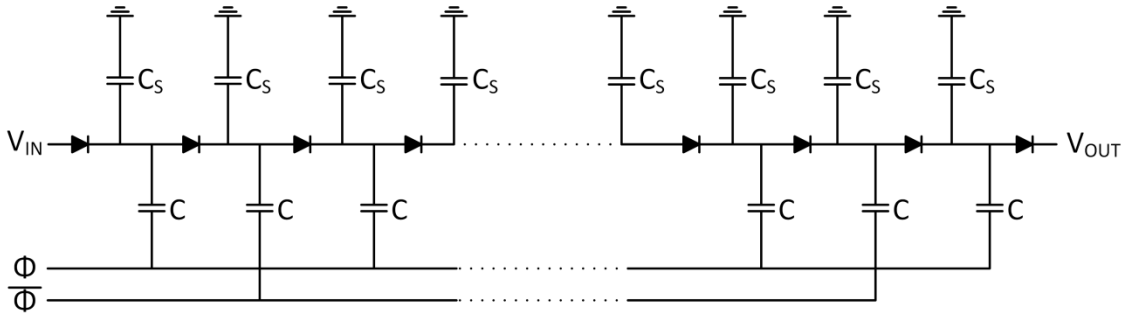

Figure 2-7 Dickson voltage multiplier circuit (after Dickson, 1976, [16])

Here, the nodes of the diode chain are connected in parallel to the coupling capacitors. There is no theoretical limit to the number of stages in this multiplier. This circuit has been optimised further in research work carried out since its first conception in 1976. An overview of the evolution of charge pumps is found in presented in [47, 48].

The number of capacitor stages, in a basic Dickson charge pump, determines the overall multiplication factor of the device; hence an issue exists for large multiplication factors requiring greater areas for an increased number of stages. The non-overlapping signals which control capacitor charging were generated by switching the signals hi and low, a further issue lies in the power loss caused by switching. In the case of energy harvesting devices where power efficiency is a critical factor, this is not an ideal multiplication circuit.

MOSFET charge pumps were first introduced in an attempt to address the insensitivity of the Dickson charge pump to parasitic capacitance. Here, the isolating diodes in the Dickson circuit are replaced by diode-connected-MOSFETS. The constant diode voltage, V_d, is thus replaced by the threshold voltage of these transistors, V_{th} which is influenced by the source-substrate voltage (body effect). This effect becomes more pronounced with a greater number stages and results in a lower output voltage than in the case of the diode circuit [49, 50].

The gain of this pump is given by:

$$GV = \Delta V - Vth \qquad 2\text{-}2$$

Where ΔV is the voltage fluctuation at each pumping node. Unfortunately, as the supply voltage decreases, so too does ΔV and, consequently, the pumping gain also decreases. Therefore, it is evident that this Dickson charge pump is not suitable for low voltage operation.

Another charge pump, based on switched capacitor circuits, is the voltage doubler charge pump [51]. The devices are suitable for high performance, low-voltage operation. A voltage doubler charge pump cell can be seen in figure 2-8.

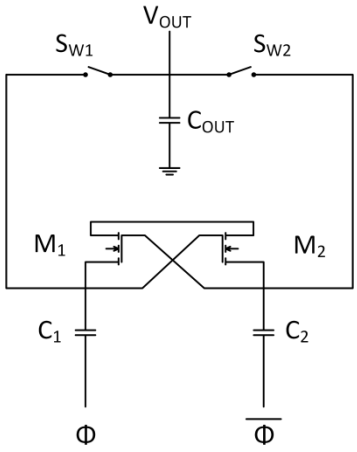

Figure 2-8 A single basic cell of a voltage doubler charge pump (after Phang, 2001, [51])

The non-overlapping clocks are of amplitude $V_{DD.}$ The transistors are switched on and off successively to charge capacitors C_1 and C_2. If $V_{in} = V_{DD}$, then the output voltage is given by the following expression

$$V_{OUT} = 2V_{DD} \qquad 2\text{-}3$$

In the case of the voltage doubler presented in [52], a maximum theoretical efficiency of 75% is achieved using integrated capacitors while an efficiency of 95% is achieved using external capacitors. Voltage doublers may seem the obvious choice for multiplication as they offer improved area and electrical efficiency over Dickson charge pumps; however, limitations such as the problem of electrical breakdown still remain for transistor circuits. Modern MOS components have become so small that they are now prone to electrical breakdown for voltages in the order of tens of volts. This renders them inept in providing multiplication for these higher voltage levels.

Both MOS and discrete charge pumps have been used to step up the voltage of energy harvesters. In [53] a MOS charge pump is used to both rectify the AC voltage output of an energy harvesting system into DC, but also multiply that voltage so a maximum output of

$4*(V_P-V_{TH})$ is achieved, where V_P is the peak of the AC input and V_{TH} is the threshold drop of the MOS transistors. An output of 1.8V DC is achieved for an input AC voltage of 1V.

A discrete component charge pump is utilised in [54] to boost the voltage of a low voltage piezoelectric generator. The charge pump is similar in design to a Dickson charge pump, where capacitors and diodes are cascaded in stages to achieve multiplication; this can be seen in figure 2-9.

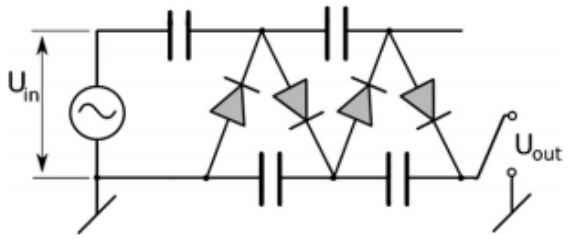

Figure 2-9 Discrete charge pump with two multiplication levels (after Marzencki et al, 2007, [54])

The paper presents a fully integrated energy harvesting solution. The system is created as a System on Package (SoP) with the generator, power conditioning circuit and rectifier fabricated on a single chip. DTMOS (dynamic threshold voltage MOSFET) transistors are set up in diode-configuration to achieve a low threshold voltage (<200mV). For a 1V input, the overall output of the system was 3V at 30nW. The system achieves an electrical efficiency of ≈30% at this level.

Recently a step-up converter was made commercially available with the specification of being a step-up converter to integrate directly with low-voltage energy harvesting systems [55]. This device can accept input voltages as low as 20mV and uses an external transformer to step it up to one of four selectable output voltages (2.35V, 3.3V, 4.1V or 5V). This device operates particularly well at low input voltages (<100mV) where electrical efficiency is at a maximum (40-60% depending on transformer ratio). For higher input voltages (>200mV), this efficiency range is much lower (5-20%). In its basic form, this device is a capacitive charge pump with an external transformer to initially boost the voltage. This is an impressive advancement in the area power management for energy harvesting devices.

2.3.2. MEMS Voltage Converters

This section features the work that has been previously conducted in the topic of MEMS voltage converters. These studies form the foundation on which the designs, presented later in

this report, are based. The systems presented in each of these previous investigations are related by the mechanically variable capacitor. While the majority of the papers reviewed in this section are purely theoretical in their analyses, with no devices being fabricated, the devices which have been fabricated have reported little information regarding parasitic capacitances encountered or electrical efficiency obtained, which is a critical factor for energy harvesting systems. Therefore, while this is not a new topic of research, there is still sufficient scope for future work.

A power converter based on a mechanically variable capacitor is first presented in [56]. Here, the circuit is electrically driven into resonance by an active bridge circuit on the primary side of the circuit. This mechanical energy created on the primary side is transferred to the load on the secondary side by the mechanical coupling of the capacitors. This work was continued by Norowolski in [57], where an electromechanical boost converter is presented. The circuit diagram for this converter is shown in figure 2-10.

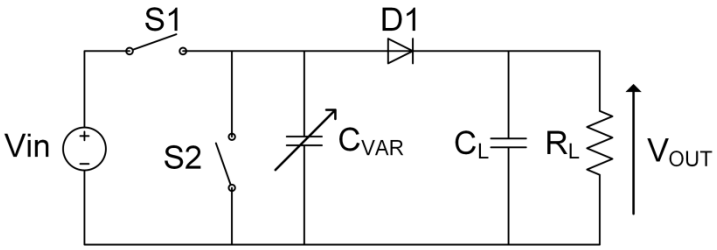

Figure 2-10 A simplified schematic of the electromechanical boost convertor (after Noworolski, 1998, [57])

The operation of this device is divided into “pumping” and “boost” stages. In the pumping stage, S1 and S2 are non-overlapping switches which are run at the resonant frequency of the system. The switch S1 is turned on when the capacitor reaches a point of minimum capacitance i.e. electrodes are furthest apart. At the point of maximum capacitance, S2 is turned on. This cycle repeats until the desired output power and voltage level is obtained. The boost cycle then begins. The switch S2 is held open in order to apply a constant charge constraint to the capacitors decreasing capacitance. This causes the voltage across the variable capacitor to increase. When it reaches the output voltage, V_{out}, the diode begins to conduct and transfer the stored energy to the RL load circuit. The switch S1 then opens, allowing the capacitance to increase, thus decreasing the voltage across the capacitor until the next pump cycle starts.

The multiplication level depends on the ratio of maximum to minimum capacitance. This device was fabricated using a SAMPSON process which offers low parasitic capacitance but also low aspect ratios. The full details of this process are details in the thesis. The fabricated device achieved a maximum multiplication factor of 1.7 with a 20MΩ load, despite being designed for a multiplication factor of 3. This limitation is due to the parasitic capacitances.

In [58], this idea is continued, but an actuator element is added to provide the necessary force required to separate the capacitor electrodes.

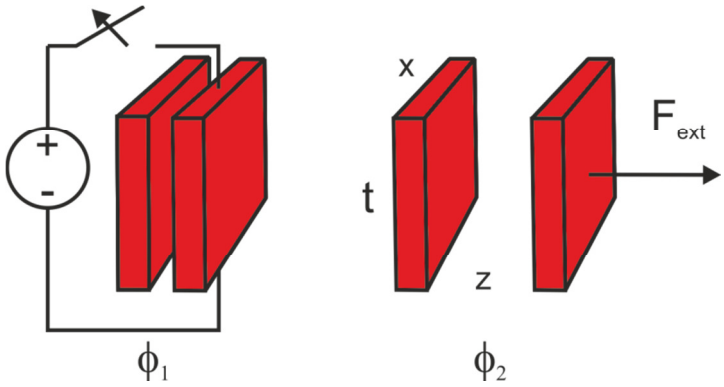

Figure 2-11 Conceptual diagram of single stage mechanical voltage pump (after Otis and Lu, 2001, [58])

The operation of this device is shown in figure 2-11. During Φ_1 a voltage is applied to the capacitor, the electrostatic force between the plates causes the moveable plate to move towards the fixed plate. This reduces the gap between the plates and so the capacitor is charging to a maximum level. During Φ_2 an external actuation force pulls the plates apart. The capacitor which has been kept at a constant charge, now has a lower capacitance value from the increased gap and therefore, from the relationship $Q=CV$, the voltage across the capacitor must increase. The amount by which the voltage increases depends on the gap between the electrode at maximum and minimum capacitance. The multiplication factor is given by:

$$M = \frac{C_{MAX}}{C_{MIN}} = \frac{V_{OUT}}{V_{IN}} \qquad 2\text{-}4$$

An SOI process is suggested for this device as it offers a high aspect ratio (50µm device layer) which allows for a high capacitance level with a lower surface area. A single mask device also simplifies the fabrication process. In the sample layout shown in figure 2-12, there are many actuator fingers to generate a high actuation force required to overcome the electrostatic force generated by the capacitors when the minimum gap is achieved. The

springs are connected to mechanical stoppers which limit the motion of the electrodes and prevent the plates from collapsing when the pull in voltage is reached.

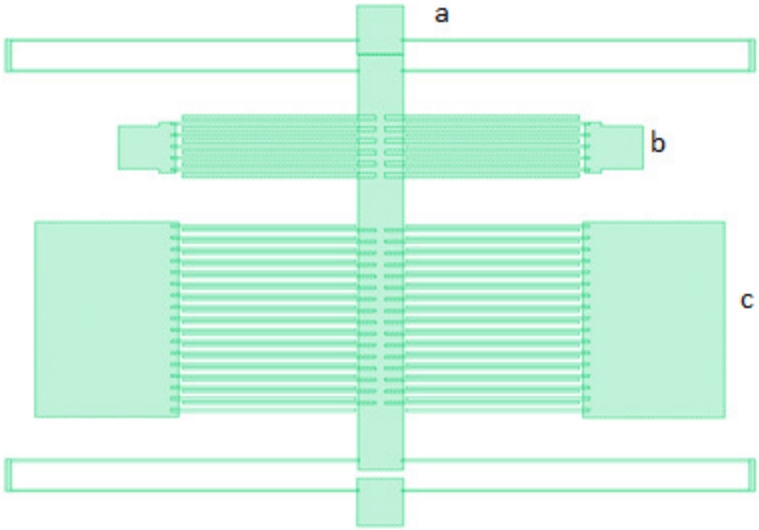

Figure 2-12 Proposed mask layout of single stage SOI mechanical voltage pump featuring a parallel plate configuration for actuator and capacitor (a) spring and stopper, (b) capacitor, (c) actuator (after Otis and Lu, 2001, [58])

Despite this layout being provided, no devices were fabricated from this work. This paper provided a basic theoretical background and did not feature any simulation results. In [10, 59] this work is further investigated and verified through system level Simulink simulations. The basic circuit for this device is shown in figure 2-13.

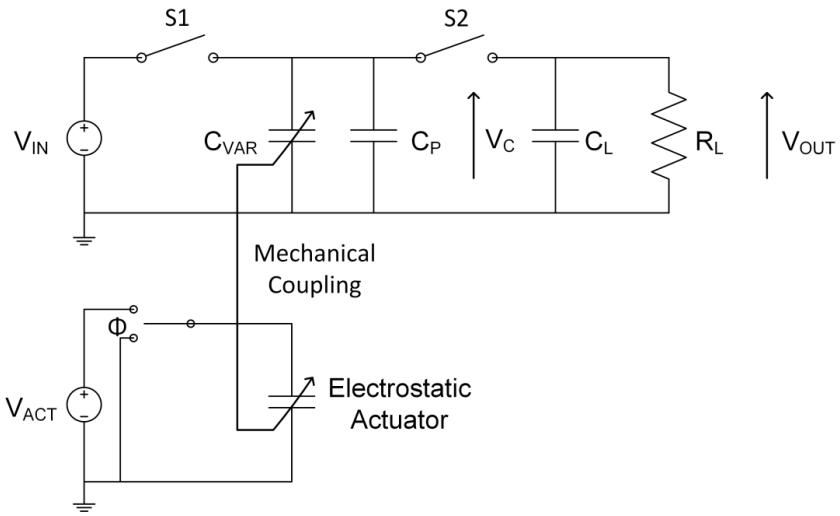

Figure 2-13 Circuit diagram for voltage converter system. Mechanical variable capacitor is coupled to the electrostatic actuator (after Haas and Kraft, 2003, [10])

The operation of this circuit is similar to that discussed in [58]; the electrodes of C(x) initially move to a maximum capacitance level by their attractive electrostatic force and once the capacitor is fully charged, the switch Φ will then turn on and the actuator pulls the capacitor electrodes apart. The switches S1 and S2 of this circuit are taken to be PIN diodes as these would be sufficient to isolate the charge on the capacitor. An equivalent circuit is made of the above schematic and illustrated in figure 2-14. From this, it is possible to derive expressions for the input series resistance R_S and the equivalent voltage source V_O.

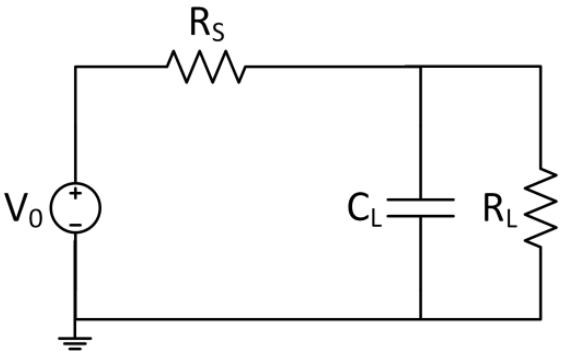

Figure 2-14 Thevenin equivalent circuit of the system shown in figure 2-13 (after Haas and Kraft, 2003, [10])

$$V_0 = \frac{MC_{MIN} + C_P}{C_{MIN} + C_P} . V_{IN} \quad 2\text{-}5$$

$$R_S = \frac{1}{(C_{MIN} + C_P) f_{clk}} \quad 2\text{-}6$$

The minimum capacitance (C_{MIN}) and parasitic capacitance (C_P) are expected to be of the same magnitude (≈1pF). The frequency of the clock is limited by the mechanical system (1…10kHz). This results in a high resistance value for R_S (typically 1GΩ), which means the load resistance must be even higher for effective voltage multiplication. This would result in an unrealistically large value of load resistance for continuous power operation. It would be well suited to charge an energy reservoir for a system requiring intermittent power.

Simulink models were developed for the capacitor, actuator and mass-spring-damper system and results are shown in figure 2-15. These results represent the steady state outputs (after 10ms) of the device. The output voltage is not entirely stationary. This is due to an output ripple caused by the load resistor R_L which can be clearly seen in the diagram.

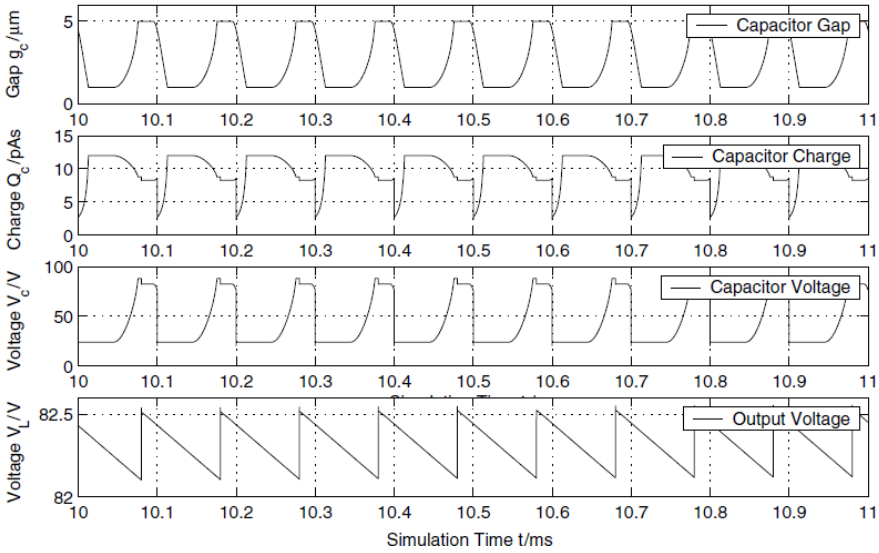

Figure 2-15 Stationary output waveforms of MEMS converter using Simulink models. Actuator and capacitor are modelled as parallel plate devices. F_{CLK} = 10kHz, C_{MIN} = 0.1pF, V_{IN} = 24V, M = 5 (after Haas and Kraft, 2003, [10])

While this paper presents no fabricated devices, the author presents a sample layout of a device if it were to be carried out using an SOI fabrication process. This is shown in figure 2-16.

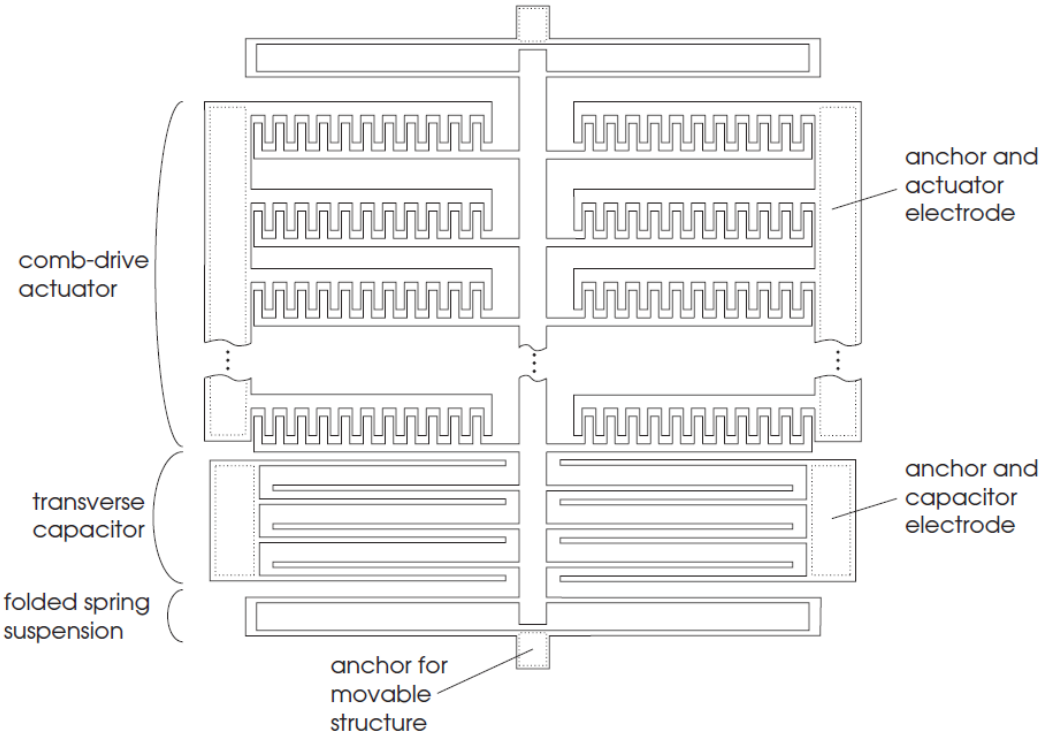

Figure 2-16 Proposed mask layout for prototype SOI device fabrication utilising comb drive actuation and parallel plate capacitor (after Haas and Kraft, 2003, [59])

The maximum efficiency obtained from system level simulations was found to be less than 20%. If parasitic capacitive elements in the circuit i.e. C_P are too high, then this will adversely affect the efficiency. In [12], a further analysis of MEMS converters is conducted but this time the focus is on the effect that the parasitic elements of the device and control circuit have on the overall operation of the multiplier. A layout of this converter is given in figure 2-17.

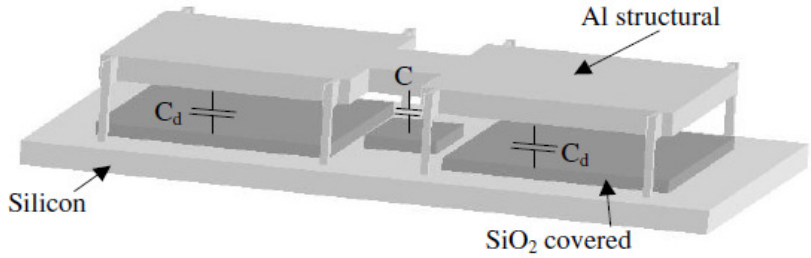

Figure 2-17 A 3D view of the MEMS voltage pump designed for an aluminium fabrication process (after O'Mahoney and Hill, 2006, [12])

The operation and design of this device is different to the previous two papers. An SOI process is not used so the results cannot be expected to exactly match the previous papers designs. However, the key point conveyed by this paper is that by using diodes isolate charge on the capacitor, the capacitance of the MEMS capacitor must exceed the value of the diodes junction capacitance at zero bias (C_{jo}). In this paper, D1N4148 diodes are being used which exhibit a junction capacitance of 4pF, this is a typical value for PIN diodes, while C_{VAR} = 500fF. This will result in a negligible gain. Increasing the capacitor area is suggested as a possible solution to this issue; however, this would also result in an increase in required actuation force. Another solution is to use MEMS switches in place of the diodes, these would contribute a much lower parasitic capacitance e.g. 1fF.

A design using a small value of variable capacitance is carried out in [13]. Here, two variable 500fF comb capacitors are actuated using an electrostatic comb actuator. The control circuit is shown in figure 2-18. The diodes used in this circuit are D1N4148. In testing this device, a DC input of 5V was applied to the control circuit while the device is driven at its resonant frequency by applying a 10V sinusoidal input voltage to the actuator. This is a high frequency (≈8kHz) so despite the capacitors being small, it can retain its charge from one cycle to the next without the issue of leakage. After 50ms, the capacitor reaches a steady state and the voltage across one capacitor is 6.8V while the voltage across the other capacitor is 9V. This is

a relatively low gain and rather impractical given that there must be a 10V input to drive the actuator. The necessity of a high resonant frequency also means that this system would be unsuitable for integration with electromechanical energy harvesters which exhibit low resonant frequencies (≈300Hz). This paper also does not report on energy efficiency. An FEM analysis, using MEMS+ and Cadence, of this device is given in [60].

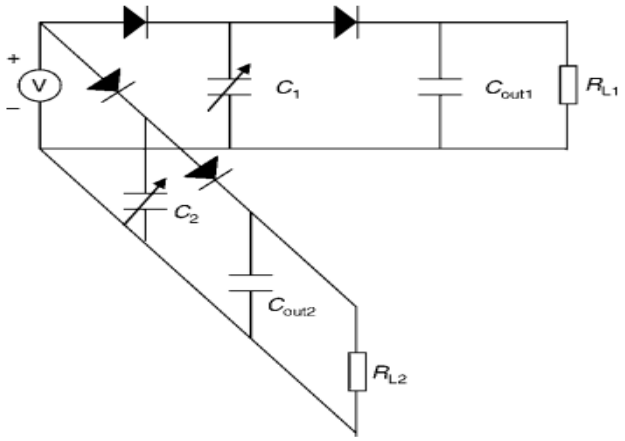

Figure 2-18 Circuit diagram for single output, dual output MEMS converter (after Li et al, 2007, [60])

Recent work investigating electrical efficiency of MEMS converters is given in [11]. A step-down converter is discussed in this paper. The circuit diagram is shown in figure 2-19.

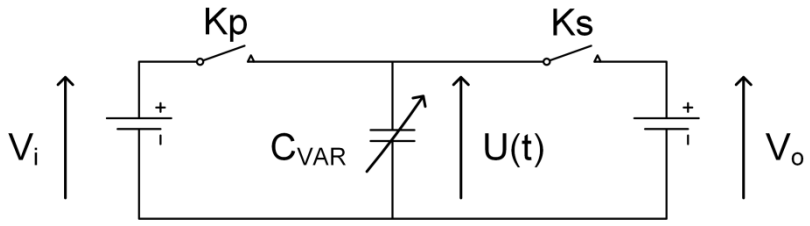

Figure 2-19 Elementary circuit of voltage step down MEMS converter (after Ghandour et al, 2009, [11])

The conversion cycle starts with C_{VAR} charging to V_i by closing the switch K_p. Once it is charged, the capacitor is isolated by opening both switches. The gap between capacitor plates is then decreased so the capacitance increases while the voltage decreases. At the point where $u(t) = V_O$, the switch K_s opens and the charge on C_{VAR} is transferred to the output. Timed switches replace blocking diodes from [10] in the circuit schematic. It is found that by operating these switches at the resonant frequency of the variable capacitor, results in maximum energy transfer and efficiency of the system. This gives greater oscillation

amplitudes so a maximum displacement (beyond the static pull-in limit of 1/3rd the electrode gap) can be reached with a voltage less than that of the pull-in voltage. This is another purely theoretical investigation.

This work is further developed in [61] where another step-down converter is presented. This converter supposedly will step down a 20V supply to 10V with a maximum electrical efficiency of 76%. This again is a theoretical investigation; the listed results are obtained from Simulink simulations. Silicon on Glass (SOG) fabrication process has been proposed for the future fabrication of the variable capacitor. However, while this paper is claiming to feature 76% efficiency, there are 3 switching elements which are seemingly unaccounted for as no mention is made to the type of switch used. Therefore, it can only be assumed that this 76% efficiency is obtained using an ideal switching model. In reality, mechanical switches can be a key source of efficiency degradation.

According to the previous investigations into these MEMS voltage converters, the isolating switches are a strong limiting factor. It was evident in these investigations that, to date, diodes have been the popular choice for isolating the charge in the variable capacitor. Typically, diodes exhibit a significant junction capacitance (≈1-5pF) when compared with the capacitance of the mechanically variable capacitor. Diodes also feature a relatively low "off-state" resistance (≈MΩ) so it is possible for the variable capacitor to discharge through the diode rather than hold its charge from cycle to cycles if the frequency of the input charging signal is too low. Dynamic or zero thresholds MOSFET diodes were also previously mentioned, which would offer a low forward voltage drop but still feature quite a high junction capacitance level [62].

MEMS switches move under an applied actuation force to make/break a circuit. In most cases the actuation is provided by an electrostatic force between switch contacts, although, in the case of an inertial MEMS switch, this actuation is provided from ambient vibration. MEMS switches promise to combine the advantageous properties of both mechanical and semiconductor switches. They offer high RF performance and low DC power consumption of mechanical switches but with the small size, weight and low cost features of semiconductor switches [63]. An overview of MEMS switch technology is given in [64-70]. Many commercially available MEMS switches already exist [70, 71], but would not integrate well with the MEMS voltage converter circuit due to actuation voltage levels.

Inertial switches utilise ambient vibrations to provide this actuation force thus eliminating the need for an actuation voltage supply which saves on resources and power consumption. The principle of operation is similar to that of the capacitive energy harvester discussed previously. A proof mass electrode oscillates under ambient vibrations making and breaking contact with a fixed electrode as it does so. Recent papers on this topic include [73, 74]. The advantages of inertial switches are that they require no external power to operate and they can be directly integrated with other inertial MEMS devices e.g. electrostatic energy harvesters [75]. Therefore they provide an interesting solution the switching element issue.

2.4 Summary

Charge pumps are a well-researched area and have been the dominating technology for voltage multiplication in past years. High voltage multiplication can be achieved using a discrete capacitor-diode network but switching loses make this an inefficient system in terms of electrical power. The efficiency can be somewhat improved by using diode configured MOSFET transistors in place of regular PIN diodes, however, the switching elements still exist and will still require power to perform switching. In addition to this issue, MOSFET charge pumps are limited in the level of voltage they can multiply. As previously mentioned, electrical breakdown can occur at a lower voltage with the continuing size reduction in transistor technology.

The limitations of charge pumps leads to room for researching new converter technologies which will provide the same functionality (i.e. voltage multiplication) while improving on the electrical efficiency and voltage limitations of the original charge pumps.

In comparison with other MEMS technologies, e.g. switches, accelerometers, MEMS voltage converters are a relatively unnoticed research area. Several papers exist, as is evident from the review in this section, but many of these papers are purely theoretical. Although there have been fabricated devices reported, there is still much room for development in this area. In particular, the combination of existing energy harvesting technology with developed MEMS voltage converters has not previously been investigated. While this integration of technologies may appear undemanding, in the case of solar panel harvesters which output

relatively high voltage levels, the design process becomes more complicated for vibration energy harvesters which output much lower voltages.

This work aims to replace these charge pump circuits with a MEMS voltage converter for energy harvesting systems. The MEMS converter is a single stage capacitor multiplier so less area is consumed than a multistage charge pump, particularly for higher voltage multiplication. The interface circuit of the converter will be optimised in an attempt to achieve higher electrical efficiencies than charge pumps for the same level of multiplication. A MEMS converter can also be developed to multiply the low voltage output of a vibration energy harvester without compromising the level of power output. This thesis will focus on the development of two types of MEMS converter which will be designed to be integrated with both relatively high (24V) and low voltage (0.5V) energy harvesters i.e. solar and vibration.

A bi-stable converter will be developed for use with high voltage solar energy harvesters. An electrostatic force from the variable capacitor and mechanically coupled actuator will manipulate the position of the capacitor electrodes to provide an increase in voltage during constant charge. A second converter will also be developed for the low voltage vibration energy harvesters. These harvesters also tend to produce low levels of power (µW range) and so a structure must be designed which will minimise the amount of power consumed. For this reason, a resonant device is presented. This converter replaces the actuator of the bi-stable devices with a proof mass. The displacement of this proof mass due to vibration will cause a corresponding displacement in capacitor electrodes. By varying either the dimensions of the mass or the length of the springs, the resonant frequency of this system can be tuned to match the resonant frequency of the energy harvester. This concept is similar to that of an electrostatic energy harvester. These harvesters usually feature a pre-charged capacitor and inductive fly-back circuit which is unnecessary in this case as the input voltage would come directly from the vibration harvester.

The next section of this thesis details the theoretical modelling and initial simulations conducted. The theoretical models presented in [10] will be developed; further system level and FEM simulations will be carried out to create an accurate circuit level model of the entire MEMS and interface circuit system. Prototype devices will then be fabricated using an SOI process and their performance will be evaluated in terms of output voltage and electrical efficiency.

Chapter 3 Models and Performance of Bi-stable MEMS Voltage Converters

3.1 Introduction

This chapter presents the theoretical work conducted in the designing of the bi-stable MEMS voltage converters. The operation of the devices is as follows; when a mechanically variable capacitor is held at a constant charge and the electrodes are separated to a distance of minimum capacitance, the voltage across the capacitor will increase, $Q=CV$. The bi-stable device presents itself as a solution to voltage conversion for static energy harvesting system as an electrostatic actuator is employed to separate the capacitor electrodes. MEMS converters have the advantage of being single stage devices, easily fabricated using an SOI process and can multiply a wide range of voltage inputs, including low voltages (≈0.5V).

The bi-stable device presented in this thesis is designed with a solar cell in mind as the harvester providing the voltage to be multiplied. A typical output of such a system would be 24V. In addition to the design of the MEMS device, a suitable control circuit must also be created to manage the charging/discharging of the capacitor device and to achieve the maximum energy efficiency and output voltage of the system.

A circuit level implementation for this device is shown in figure 3-1. The variable capacitor (C_{MEMS}) is charged from the input voltage V_{in}. The diodes D1 and D2 isolate the variable capacitor from the RC load circuit. This prevents the load capacitor from back charging the variable capacitor. The parasitic capacitor C_P is related to the capacitive fringing fields of the variable capacitor.

The operation of this circuit was first verified using system level Simulink and Spice simulations. These models are then used to construct a printed circuit board (PCB) prototype

interface circuit using commercial off the shelf components. The evaluation of both MEMS device and circuit is discussed in further chapters of this thesis.

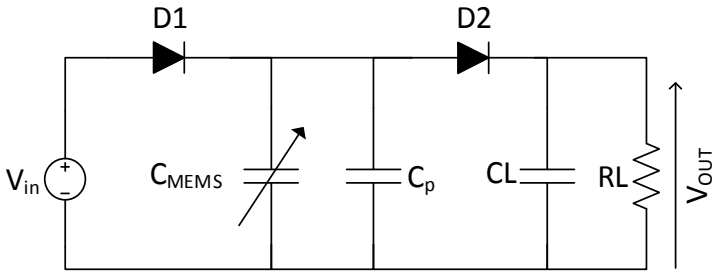

Figure 3-1 MEMS voltage converter circuit. C_{MEMS} is the mechanically varying capacitor and C_P is the parasitic capacitance. Diodes D1 and D2 isolate the charge on the capacitor.

This section focuses solely on the design and operation of the bi-stable MEMS variable capacitor unit. The design and analysis of the resonant MEMS capacitor device will be presented in the next chapter of this thesis.

3.2 Principle of Operation

The main component of the designs for the MEMS voltage converter is the mechanically variable capacitor. The value of capacitance is changed by varying the gap between the capacitor's electrodes. This is done by the application of an external force which can be generated using the electrostatic force of an additional actuating mechanically variable capacitor or from ambient vibrations. A conceptual diagram of this operation is given in figure 3-2.

The variable capacitor is initially at a rest position (g_0) before a voltage is applied and the capacitor starts to charge. Electrostatic attraction between the electrodes will pull the moveable electrodes towards the fixed electrodes until a minimum gap position is reached (g_{MIN}), this corresponds to a point of maximum capacitance (C_{MAX}). The actuator then applies a force in the opposing direction to the capacitors electrostatic force causing the electrodes to separate to a point of maximum gap and minimum capacitance (g_{MAX}, C_{MIN}). The actuation force is then removed and the cycle repeats. As the capacitance level is being decreased through actuation, the voltage across the capacitor is increasing resulting in a step up conversion of the input voltage when discharged to a load. The factor of multiplication is

given as a ratio of maximum to minimum capacitance as given in equation 2-4. The variable capacitor and electrostatic actuator can take one of two structures; a comb drive or a parallel plate. In this section, the behaviour of these capacitors will be examined.

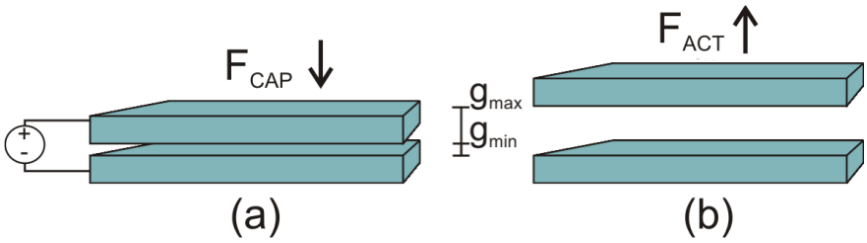

Figure 3-2 Conceptual diagram of a MEMS voltage converter, (a) Initally a capacitor is allowed to charge at a position (g_{MIN}) of maximum capacitance (C_{MAX}), (b) an external actuating force, F_{ACT}, is then applied to pull the electrodes apart to a position (g_{MAX}) of minimum capacitance (C_{MIN}).

3.2.1 Comb drive structure

A comb drive capacitor consists of multiple inter-digitated electrodes as can be seen in figure 3-3. By applying a voltage between fixed and moveable electrodes, an electrostatic force is generated and motion is induced. The thickness of the fingers is kept small relative to length and width, therefore this electrostatic force is mainly due to fringing fields between electrodes [76]

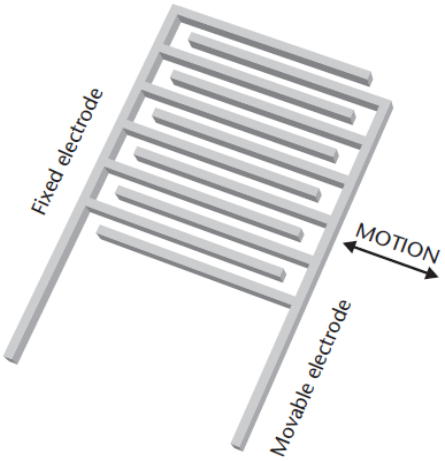

Figure 3-3 Variable comb-drive capacitor (after Beeby, Ensell, Kraft and White, 2004, [76])

The capacitance and electrostatic force generated by this form of capacitor are given by the following equations [77]:

$$C_{comb} = \frac{2Nhx\varepsilon_0}{g} \quad 3\text{-}1$$

$$F_{comb} = \frac{Nh\varepsilon_0 V^2}{g} \quad 3\text{-}2$$

Where g is the gap between electrodes, A is the electrode area, N is the number of comb fingers, h is the thickness of these fingers, x is the length of the electrode overlap and V is the applied input voltage. It can be seen from equation 3-2 that the electrostatic force is independent of electrode displacement and is based on the electrostatic shear force. Due to these properties, comb drives are typically used where displacement is required without the need to generate a large electrostatic force.

3.2.2 Parallel plate structure

This structure consists of a two parallel electrode plates which, unlike the comb structure have relatively large lengths and widths compared to their thickness. This can be seen in figure 3-4. This means that fringing fields contribute little to the electrostatic force generated between the moveable and fixed plate. The force mainly consists of parallel fields.

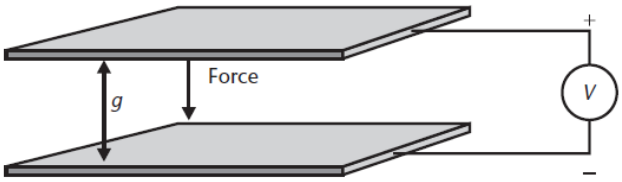

Figure 3-4 Variable parallel plate capacitor (after Beeby, Ensell, Kraft and White, 2004, [76]).

The capacitance and electrostatic force generated by this form of capacitor are given by the following equations [78]:

$$C_{plate} = \frac{\varepsilon_0 A}{g} \quad 3\text{-}3$$

$$F_{plate} = \frac{\varepsilon_0 A V^2}{2g^2} \quad 3\text{-}4$$

In contrast to the comb drive capacitor, the electrostatic force of the parallel plate capacitor does depend on the gap between electrodes and is generated through the major electrostatic field lines. As the gap between electrodes alters, so does the electrostatic force. This implies that a parallel plate actuator will generate a large electrostatic force only when the stroke distance is relatively low.

3.3 Dynamic Response

In the case of the bi-stable converter device, electrostatic force from an additional actuating capacitor element provides the actuating force necessary to change the gap between the main capacitors electrodes. A concept diagram is given in figure 3-5. A comb structure was chosen for the variable capacitor as its electrostatic force is independent of electrode gap. Therefore at the position of maximum capacitance, it will not require as much actuation force to pull the electrodes to the minimum capacitance position as would be required in the case of a parallel plate capacitor, which generates a gap-dependent force. A parallel plate structure is used for the actuator. The force generated by the actuator will increase as it pulls the capacitor electrodes apart.

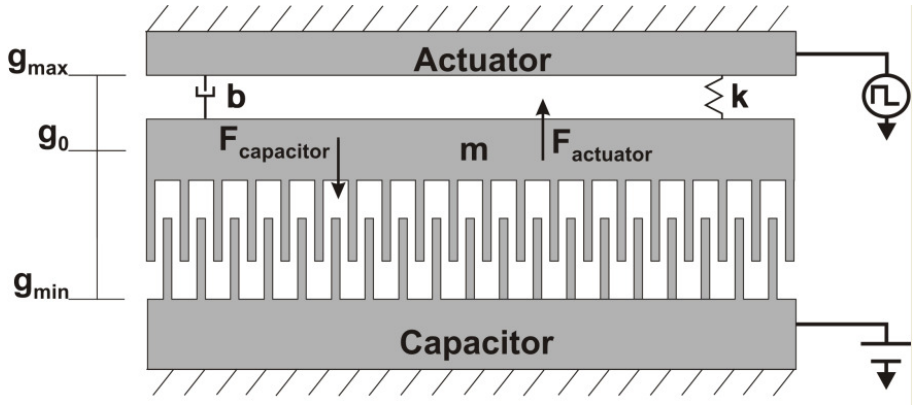

Figure 3-5 Bi-stable converter conceptual diagram. A constant DC voltage is supplied to the comb drive capacitor and an electrostatic force, *F*, is generated between the moveable mass electrodes and the capacitor electrodes resulting in a displacement of the mass to the minimum gap point, g_{MIN}. The actuator then switches on and the electrostatic force between the moveable electrode and actuator, in addition to the restoring spring force *k*, causes the mass to move in the opposite direction to the maximum gap point, g_{MAX}. The actuator then turns off and the cycle repeats.

The 2nd order equation dictating this motion is given by:

$$mg'' + bg' + k(g_0 - g) = F_{EL} \qquad 3\text{-}5$$

Where *k* represents the spring constant, *b* is the damping co-efficient, *g* is the displacement, g_0 is the "at rest gap", *m* is mass and F_{EL} is the electrostatic force which is given as the difference between the force generated by the capacitor and the actuator (equation (3-2, 3-4)).

The bi-stable converter consists of two moving electrodes that are mechanically coupled. For this reason, some form of combined mechanical backbone and suspension system is needed to facilitate this movement. An example of such an arrangement is shown in figure 3-6 whereby a central beam holds the moveable capacitor and actuator electrodes. This beam is suspended by springs which are anchored to the substrate. This layout allows for any type of capacitor and actuator to be added to the beam in a modular way. This is illustrated in figure 2-16.

3.4 Design Considerations

3.4.1 Spring Constant

The spring constant k provides a restoring force for the moveable electrode of the capacitor once it has been displaced by a force. For the devices in this work, a double crab leg suspension is used to provide the spring force [59]. This can achieve full deflection given a wide travel range. It consists of two springs in series to lower the overall spring constant of the system. The bumpers mechanically limit the displacement of the beam so pull-in of the parallel plate electrodes is not an issue.

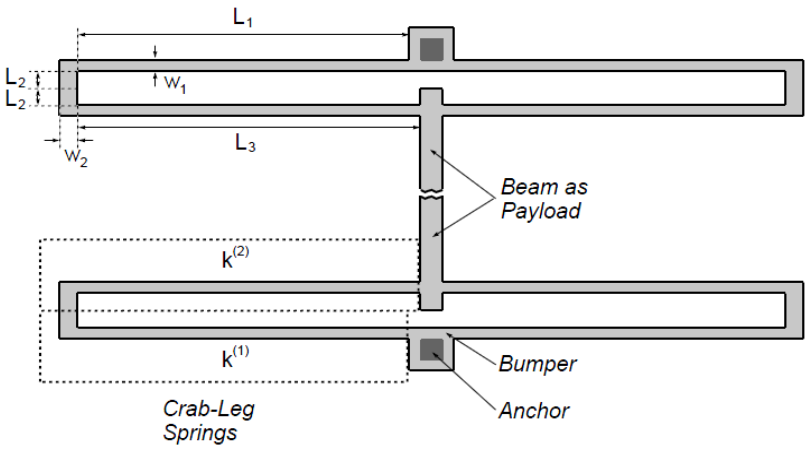

Figure 3-6 Crab leg spring suspension. The bumper and anchor parts act as mechanical toppers limiting the range of motion of the payload beam (after Haas, 2003, [59]).

The spring constant is given by:

$$k_y^1 = 4E_{Si}t\left(\frac{w_1}{L_1}\right)^3 \frac{L_1 w_2^3 + L_2 w_1^3}{L_1 w_2^3 + 4L_2 w_1^3} \qquad 3\text{-}6$$

$$k_y^2 = 4E_{Si}t\left(\frac{w_2}{L_2}\right)^3 \frac{L_1 w_2^3 + L_2 w_1^3}{4L_1 w_2^3 + 4L_2 w_1^3} \quad 3\text{-}7$$

$$k_y = \left(\frac{1}{k_y^1} + \frac{1}{k_y^2}\right) \quad 3\text{-}8$$

It is necessary to design a spring which is sufficiently flexible to allow for full deflections of the capacitor/actuator electrodes, but not so flexible that the structure of the spring becomes fragile and difficult to fabricate successfully. The spring must also be stiff enough reducing the effect of displacement due to gravity. For this reason, a spring constant of 5N/m was targeted for the bi-stable design. This will result in an in plane deflection in the y-axis of 0.53µm under gravity.

The resonant design features a lower value of spring constant as the system operates from low frequency, low amplitude ambient vibrations. For the resonant design, this was chosen to be 2N/m but this was further reduced to 1N/m in the modified resonant design. Reducing the spring constant, while maintaining the same proof mass dimensions, lowers the level of vibration amplitude required to achieve full electrode displacement. However, despite the spring constant for the modified resonant device being relatively low (1N/m), the vibration amplitude required to drive the device is $15ms^{-2}$ which is higher than the resource available from the VIBES generator. This is due to the distance of travel between the electrodes (21µm from g_{MAX} to g_{MIN}). A lower distance of travel results in a lower multiplication value; this is a key design trade off. As a proof of concept, $15ms^{-2}$ was considered to be an acceptable level of acceleration.

3.4.2 Electrostatic Force

The electrostatic force generated by parallel plate and comb drive capacitors is given by equations 3-2 and 3-4. The overall electrostatic force generated is given by:

$$F_{EL} = F_{plate} - F_{comb} \quad 3\text{-}9$$

For the capacitor, it is necessary to not only create a structure which can offer sufficient electrostatic force under an applied voltage, but that can also minimise the effect of parasitic capacitance on the overall capacitance level. In the FEM modelling section of this report, it can be seen how the structure of electrodes were chosen based on varying the length and simulating the corresponding capacitance levels.

The force generated by both capacitor and actuator must be sufficient to pull the electrodes between the minimum and maximum gap positions respectively while overcoming the restoring spring force. Once the capacitor has been designed and is capable of moving to a position of g_{MIN}, the actuator must simply be large enough to pull the electrodes back to a position of g_{MAX}.

3.4.3 Damping

Damping *b* is a force which acts as a resistance to the motion of the mechanical system. The damping factor determines the speed at which the system can operate at. If the system is under damped, the motion of the electrodes from g_{MIN} to g_{MAX} will be fast but may oscillate about the displacement limits. This will impact the output voltage. Therefore a critically damped system is desirable but will depend on the structure of the device. It is difficult to obtain an exact calculation of the damping coefficient as the dominant damping forces depend on the structure of the device. In the case of comb drive capacitors, where the electrodes move parallel to each other, slide film damping [79] is the main damping component. In a parallel plate capacitor, where electrodes move towards each other, squeeze film damping [80-83] is the dominant damping component. For the purposes of the system level simulations the formulas have been taken from [84] as the structure is similar to the designs presented in this report.

$$b = (0.8)\mu_{eff} hN \left(\frac{L}{g_0}\right)^3 \left(\frac{c^2}{c^2+1} + \frac{2c^2}{9(c^2+9)}\right) \quad 3\text{-}10$$

Where $c = W/L$ i.e. ratio of electrode width to length, μ_{eff} is the effective dynamic viscosity of air and *h* is the thickness of electrodes. Once the damping coefficient has been calculated it is possible to obtain the damping ratio using the formula below

$$\zeta = \frac{b}{2\sqrt{km}} \quad 3\text{-}11$$

$$if\ \zeta \begin{cases} < 1, underdamped \\ = 1, critically\ damped \\ > 1, overdamped \end{cases}$$

3.4.4 Mass

The mass of the system is classified as the mass of the moving components i.e. the mass of the capacitor and actuator stator parts are not included. The formula for calculating the mass is given as:

$$m = D_S V \quad (3\text{-}12)$$

Where D_S is the density of silicon (≈2330 kg/m^3) and V is the volume of the mass i.e. surface area*thickness of the structural silicon layer.

3.4.5 Resonant Frequency

The resonant frequency gives the optimum time to operate the interface circuit switching at to ensure maximum power transfer. The resonant frequency depends on the mass and spring constant of the device.

$$f = \sqrt{\frac{k}{m}} \quad (3\text{-}13)$$

3.5 Performance

Using the equations given in the above section, it is possible to design the system based on these calculated parameters. A table of fixed and calculated parameters used in the design of the bi-stable device is given in Table 3-1. This table was generated using Matlab code which is located in Appendix A of this thesis.

Table 3-1 - System parameters and dimensions for bi-stable converter device based on Matlab file (see appendix A).

Parameter	Value	Unit	Description
			Fixed Variables
g_{min}	7	µm	Minimum overlap distance between capacitor electrodes
g_{max}	35	µm	Maximum overlap distance between capacitor electrodes
g_0	21	µm	Overlap distance between capacitor electrodes at rest
$g_{overlap}$	3	µm	Gap between capacitor electrodes.
L_{comb}	70	µm	Length of capacitor comb fingers
L_{plate}	1000	µm	Length of actuator parallel plates
W_{comb}	7	µm	Width of capacitor comb fingers
			Calculated Variables
m	2.67e-7	kg	Mass of moveable structure
k	4.28	N/m	Spring constant

f	646	Hz	Resonant frequency of device

The performance of the MEMS devices is analysed using system level and 3D Finite Element Modelling (FEM) simulations. The 3D model of the devices is constructed using MEMS+ software. This model is then exported to Conventorware for analysis. The system level simulations are carried out using SIMULINK and verify the basic operation of the devices i.e. electrode displacement to capacitance variation.

3.5.1 Simulink System Level Analysis

From the parameters in Table 2 and the 2nd order differential equation describing the motion of the MEMS converter system, it is possible to construct a system level model. A Simulink mass-spring-damper model has been presented in [59]. This model used complex function blocks to achieve a value for electrode displacement from an input force. However, recent editions of Simulink feature a Simscape library which enables the modelling of mechanical components without the need for complex subsystems [85]. Figure 3-7 shows such a model in Simulink.

An external force is applied to the system which results in a displacement of the system with a, certain velocity and acceleration. The acceleration is found by the fundamental equation $F=ma$. This force F includes the effect of the electrostatic forces F_{EL} of both the capacitor and actuator, spring constant k and damping b; m is the mass of the system. The hard stop element models the mechanical stopper in the MEMS device which limits the motion of the electrodes between g_{MAX} and g_{MIN}.

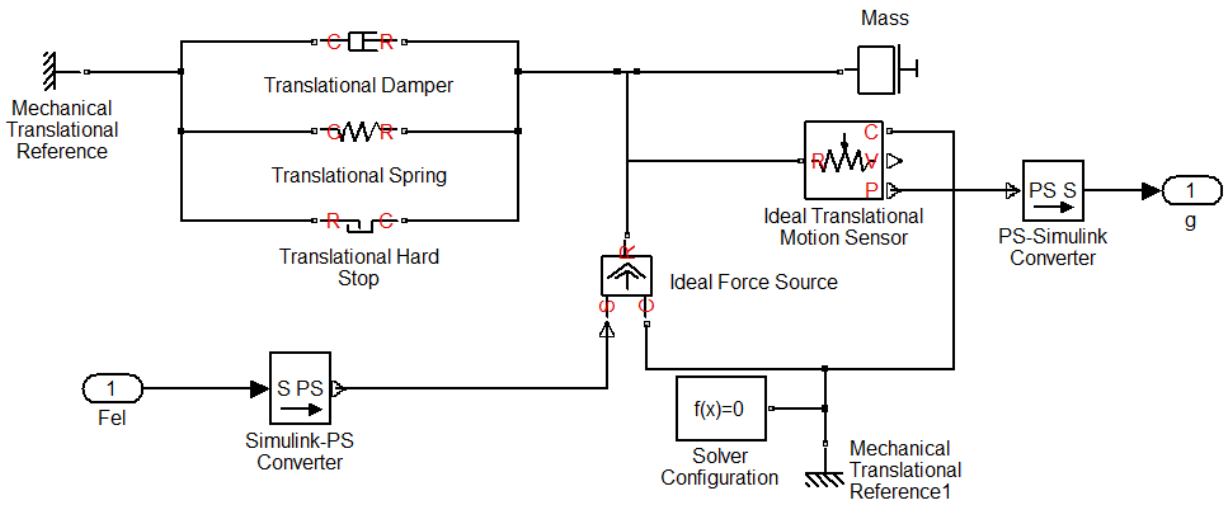

Figure 3-7 Simulink model of mass-spring-damper subsystem of MEMS converter system.

The electrostatic force input of is the difference between the electrostatic forces created by the capacitor and actuator elements. This is illustrated in figure 3-8, where the model is expanded to show capacitor and actuator blocks. The displacement produced by the mass-spring-damper subsystem forms a feedback loop to provide the electrode gap needed to calculate electrostatic force.

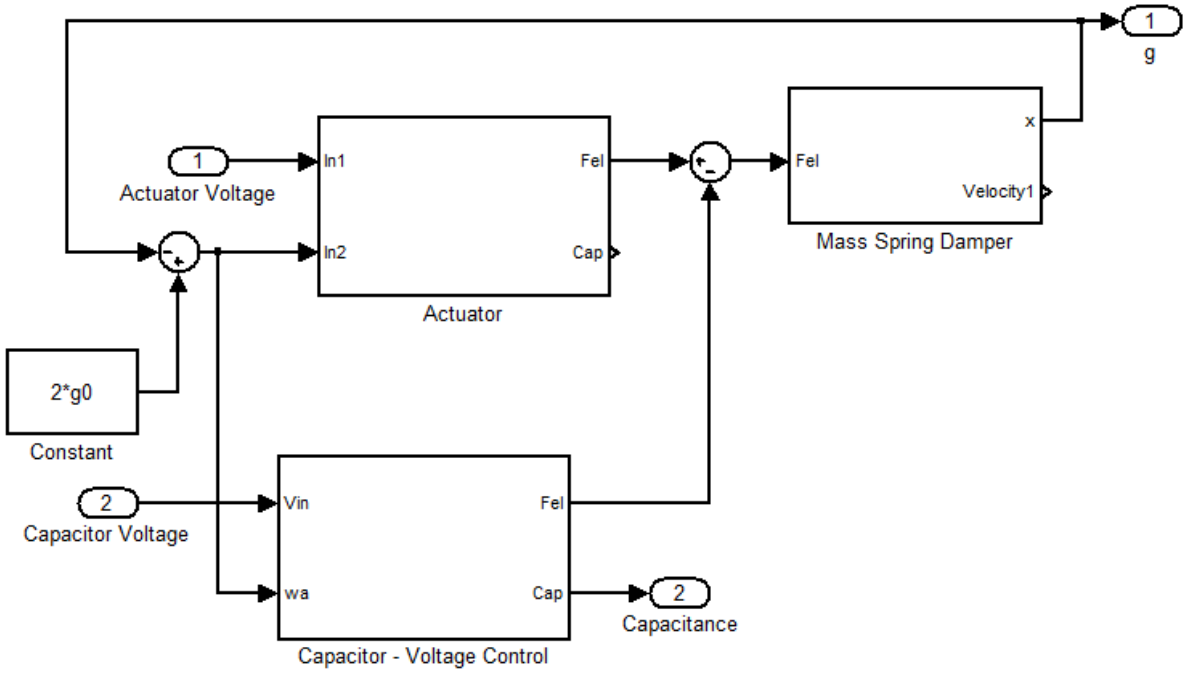

Figure 3-8 Simulink model of capacitor and actuator subsystems. This subsystem generates the electrostatic force from the difference of actuator and capacitor forces.

This force is then applied to the mass-spring-damper system of figure 3-7 and the electrode gap displacement, g, is output. The resulting variation in capacitance based on the variation in electrode displacement is given in figure 3-9.

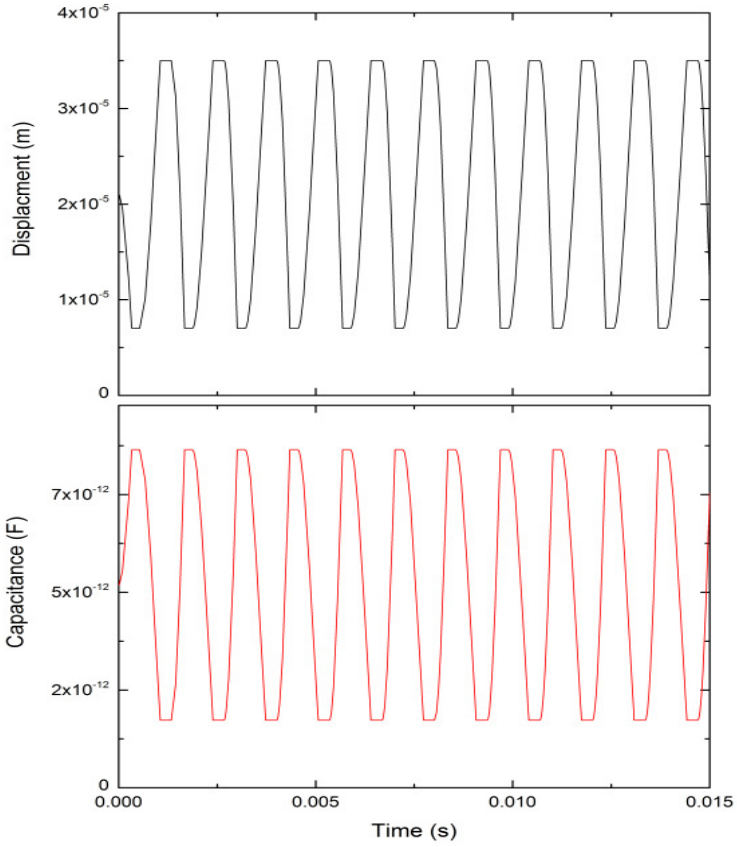

Figure 3-9 Plot illustrating the variation in capacitance due to a change in the electrode gap of the capacitor. The capacitor initially charges to a maximum capacitance before the actuator pulls the electrodes apart to a position of minimum capacitance.

3.5.2 MEMS+ and 3D FEM Analysis

The 3D model for FEM simulations is developed using MEMS+ software [86] and exported into Coventorware for analysis [87]. The analysis will consist of resonant frequency, capacitance and damping simulations. Compared to system level simulations, the Coventorware FEM simulation will produce results which will be a closer match to the final fabricated devices. This is due to the increased level of complexity in the solver calculations and the automatic simulation of parasitic elements e.g. capacitive fringing fields.

The parameters used for constructing the MEMS+ 3D model design come from the system level models and are shown in table 3-1. The device is to be designed on a low resistivity SOI wafer. Therefore, the design in MEMS+ consists of a 50µm thick silicon layer with a resistivity of 0.001-0.003 Ωcm to model the device layer of the SOI wafers that will be used during fabrication. The 3D model of the MEMS bi-stable device is shown in figure 3-10.

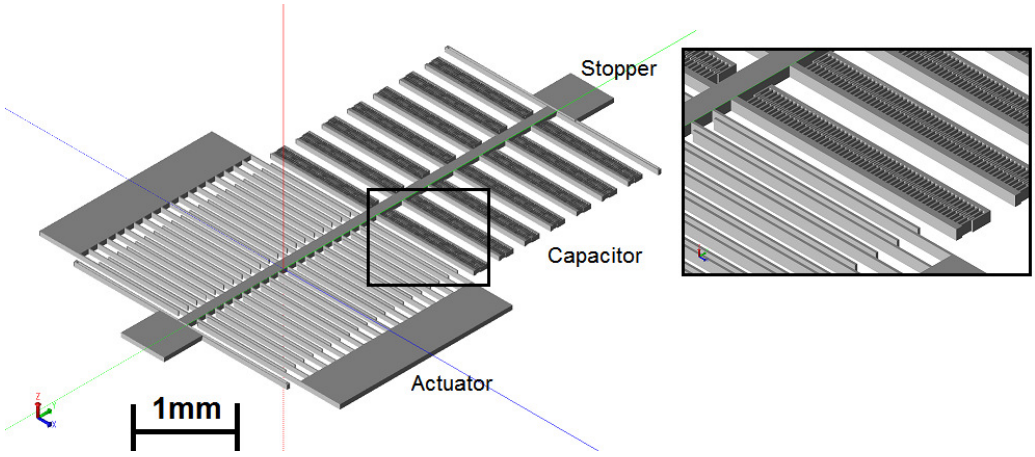

Figure 3-10 MEMS+ 3D model of bi-stable step-up converter featuring a parallel plate actuator and a comb drive capacitor.

A modified version of the bi-stable device was also designed. This device features the same general structure as the bi-stable device; however, the parallel plate configuration of the actuator has been replaced by a curved-beam zipping actuator as can be seen in figure 3-11. The curved beam will theoretically pull-in at the small gap end for a relatively low actuation voltage. The area beside the beam tip will then have a low electrostatic gap and therefore the electrostatic force should approach infinity and cause pull in. This will cause a series of pull in forces along the beam eventually causing the entire beam to pull-in in a zipping action. This form of actuator has previously been investigated in [88-90] where the authors report large beam deflections for a relatively low actuation force.

Due to the complexity of the curved geometry and the inability of the software to render such an element, no theoretical modelling could be conducted prior to fabrication. However, key design considerations were made based on the results reported in the papers listed above; The thickness of the moveable electrodes is reduced from 20µm, in the case of the bi-stable device, to 10µm to increase the flexibility of the electrodes, the length of the beams is increased to 2mm to prevent a sharp increase in step size along the beam and the tip of the beam resembles a parallel plate in order to generate a large initial actuating force.

The original bi-stable devices in this report could theoretically benefit from a reduction in area by implementing this actuator modification as a lower input voltage would be required to achieve the same magnitude of displacement. Therefore, fewer actuator electrodes would be required to provide the force required to separate the variable capacitor electrodes.

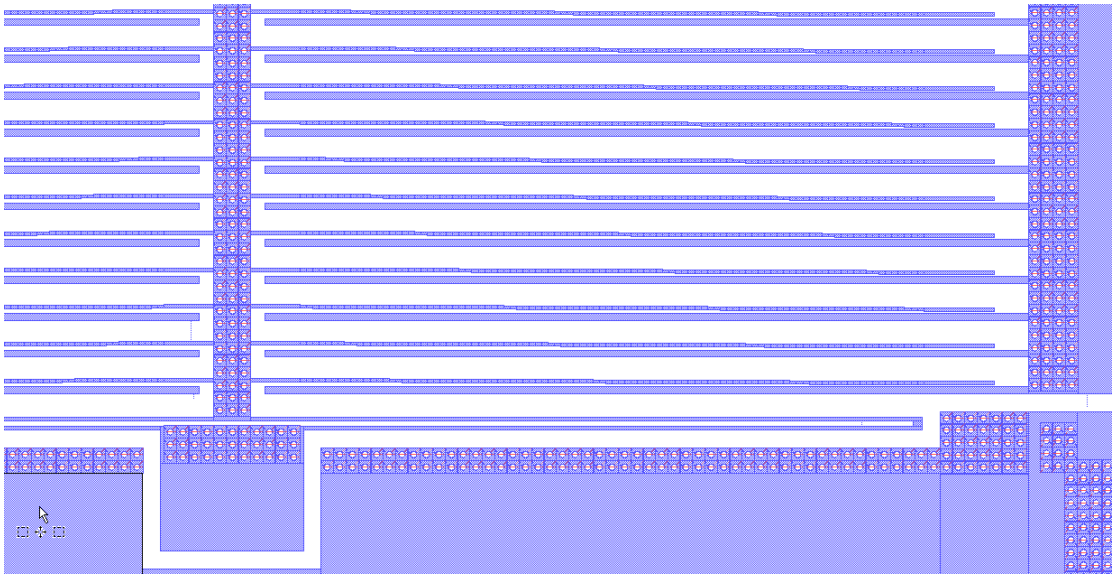

Figure 3-11 L-Edit layout of curved actuator fingers. A relatively small pull-in voltage should cause an exponential pull-in force along the beam.

3.5.2.1 Resonant Frequency

The spring constant varies greatly with the width of the spring beams. During the fabrication process, this width could be subject to some change which will alter the resonant frequency of the end device. Similarly, the mass of the device is subject to change during fabrication. In particular, the addition of perforation holes throughout the device will decrease the overall mass. These perforation holes are essential for the mask design as, during fabrication, they enable the etching of the sacrificial oxide layer beneath the structural device.

Table 3-2 below illustrates the difference that both spring width and perforation holes contribute to the resonant frequency of the device. Unfortunately, it was not possible to simulate a device with perforation holes in Coventorware due to the complexity of the meshing geometry; therefore, MEMS+ design file was imported into Simulink for these simulations. However, there is a clear difference between the accuracy of the results obtained in Simulink compared to Coventorware. This is due to the large error tolerances of the Simulink solver.

This table shows that if, during fabrication, the spring width were to be over-etched by 1µm, it would cause a significant reduction in resonant frequency. The result of a Conventorware modal analysis is shown in figure 3-12. The resulting resonant frequency is found to be ≈652Hz.

Table 3-2 - Resonant frequency of bi-stable device found using Simulink and Coventorware simulations.

Spring Width	Simulink	Coventorware
6 µm	471 Hz	519 Hz
6 µm with perforation holes	496.5Hz	NA
7 µm	606 Hz	652 Hz
7 µm with perforation holes	637 Hz	NA

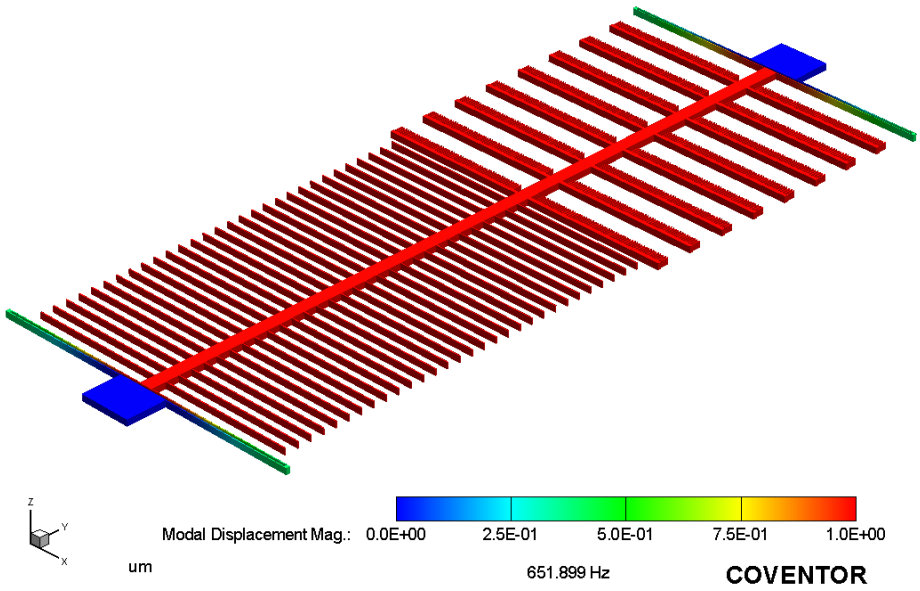

Figure 3-12 Coventorware simulation of resonant frequency for bi-stable converter device. This modal displacement diagrams illustrates how the bi-stable device will be affected at resonance.

3.5.2.2 Capacitance

The variation in the capacitance of the comb drive capacitor as it moves from a position of minimum capacitance (C_{MIN}, g_{MAX}) to a position of maximum capacitance (g_{MIN}), defines the factor of multiplication for the converter device as given in equation 2-4. A comb drive capacitor is used as the variable capacitor in both the bi-stable and resonant converter designs and therefore the formula for theoretically calculating the capacitance of this structure is given in equation 3-1. However, this will result in an ideal value of capacitance which does not take into account additional parasitic capacitances of the structure which affects the overall capacitance level. In particular parasitic fringing field

capacitance can severely degrade the overall multiplication factor of the system. The effect of this can be directly related to the structure of the capacitor.

Initially it was assumed that by keeping the value of minimum electrode overlap (g_{MIN}) as small as possible would be beneficial from a miniaturization point of view. However, as table 3-3 indicates, if g_{MIN} is small, capacitive fringing fields dominate the overall capacitance value. As g_{MIN} increases, the effect of these fringing fields is reduced. However, the electrostatic force of the capacitor also increases and so the actuator must also increase to compensate for this. Therefore, there is a tradeoff between choosing a value of g_{MIN}, to achieve a reasonable multiplication factor, and the size of the end device. For this work, g_{MIN} = 7μm which results in M=2.83.

Table 3-3 - Effect of minimum electrode overlap gap on voltage multiplication factor. The values listed are for a single segment branch of electrodes.

g_{MIN} (μm)	C_{MIN} (pF)	C_{MAX} (pF)	M
2	2.81	4.62	1.64
5	3.54	8.94	2.52
7	3.96	11.22	2.83
10	4.68	15.95	3.41
20	7.65	29.6	3.87

The ideal theoretical calculation estimated the capacitance as varying between ≈1.6pF to ≈8pF resulting in M=5. Clearly the parasitic capacitance adds ≈1.5pF to the minimum capacitance level and ≈4pF to the maximum capacitance level. For the sake of simplicity in further simulations in this thesis, a fixed parasitic capacitance of C_P = 3pF will be used. This would result in M=2.4. Figure 3-13 illustrates the sources of parasitic capacitance within the bi-stable MEMS device. This diagram also refers to a coupling capacitance, $C_{coupling}$, between the actuator and capacitor fixed electrodes. This will be discusses further in the measurement section of this thesis.

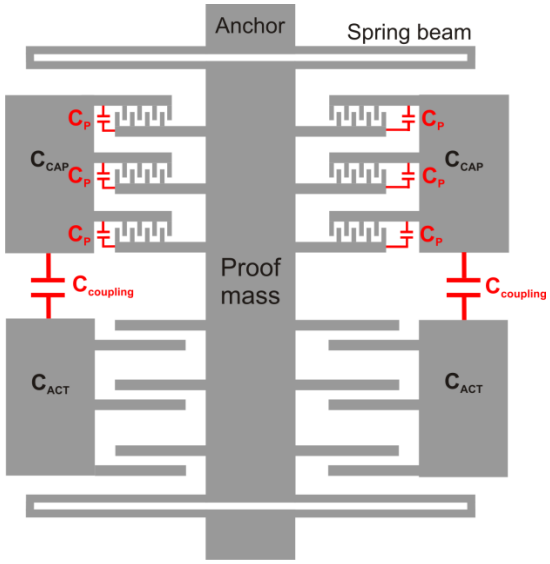

Figure 3-13 A conceptual drawing of a MEMS converter device including parasitic capacitances

3.5.2.3 Damping

The damping force of the system can be simulated using Coventorware's DampingMM solver. A Stokes flow analysis can be carried out to obtain a damping co-efficient at the points of rest (g_0), maximum capacitance (g_{MIN}) and minimum capacitance (g_{MAX}) for both the comb drive and parallel plate capacitors. To reduce simulation time, this analysis was conducted on a small sample of each capacitor structure as can be seen in figure 3-14 and figure 3-15.

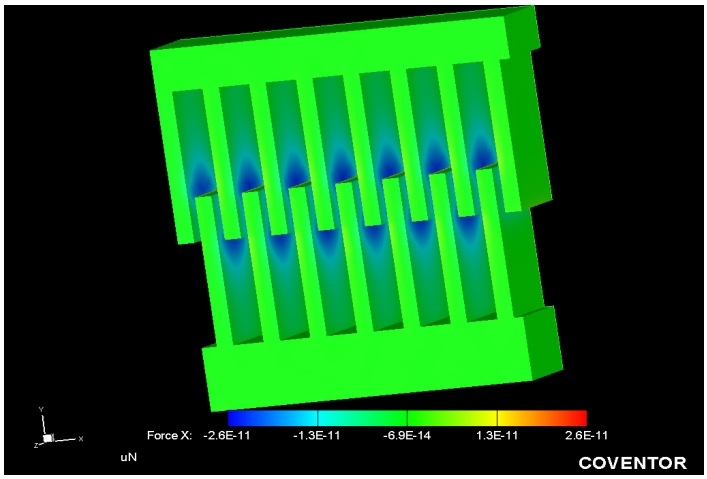

Figure 3-14 Coventorware results illustrating damping force (blue), at rest, for a sample of capacitor comb fingers in bi-stable device.

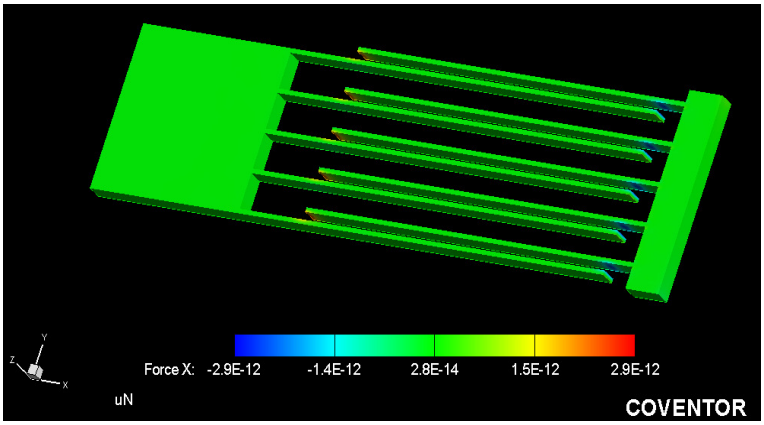

Figure 3-15 Coventorware's Visualizer result of Stokes flow damping analysis on set of parallel plate actuator fingers.

The resulting damping co-efficient for these capacitor arrangements are shown in figure 3-16 and figure 3-17. This can then be multiplied to account for the whole device.

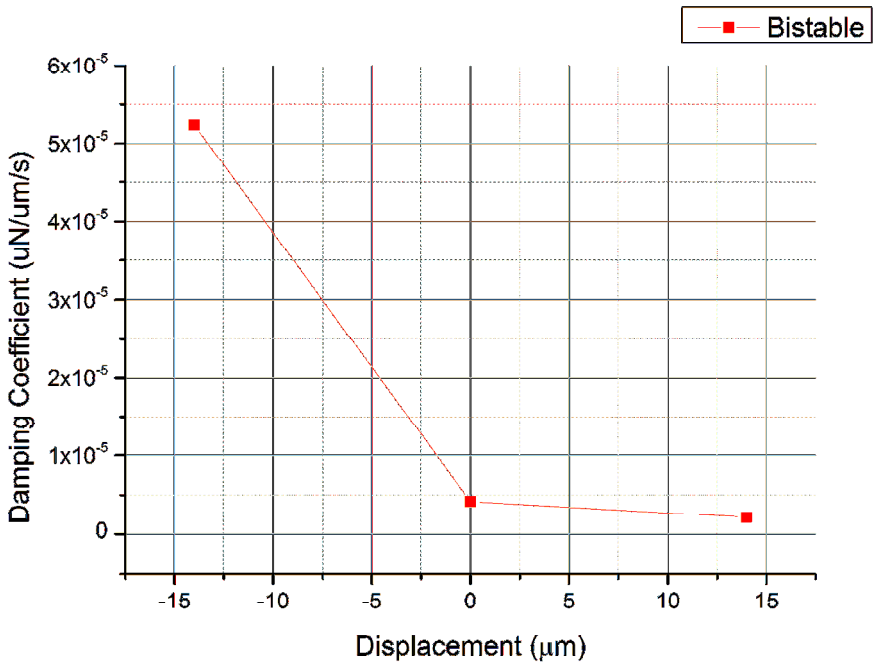

Figure 3-16 Damping co-efficient for the parallel plate actuator fingers of the bi-stable device at points g_{MAX}, g_{MIN} and g_0.

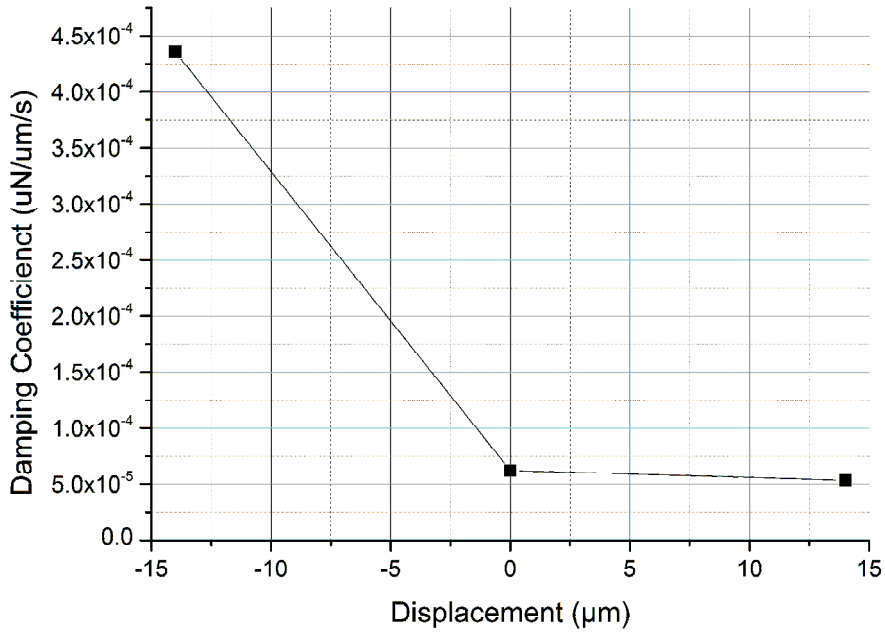

Figure 3-17 Damping co-efficient for a Stokes flow analysis on the complete bi-stable device at points g_{MAX}, g_{MIN} and g_0.

It is evident from the graphs that the parallel plate actuator contributes the majority of the damping force, particularly at the point of minimum capacitance. The theoretical estimation of damping at rest is $4.4e^{-5}$ which is in close agreement to the simulated value.

3.6 Control Circuit

In the previous section of this chapter, Simulink models were used to construct a mass-spring-damper model of the MEMS variable capacitor. These models can be further developed to include blocks which model the control circuit. Again, Simscape components are used to simplify the modelling and produce more accurate results.

3.6.1 System Level Modelling in Simulink

The Simulink model for the bi-stable device is shown in figure 3-18. Here, a pulsing voltage controls the actuator and the capacitor. The diodes have been assigned ideal parameters but still feature a 0.6V forward voltage drop.

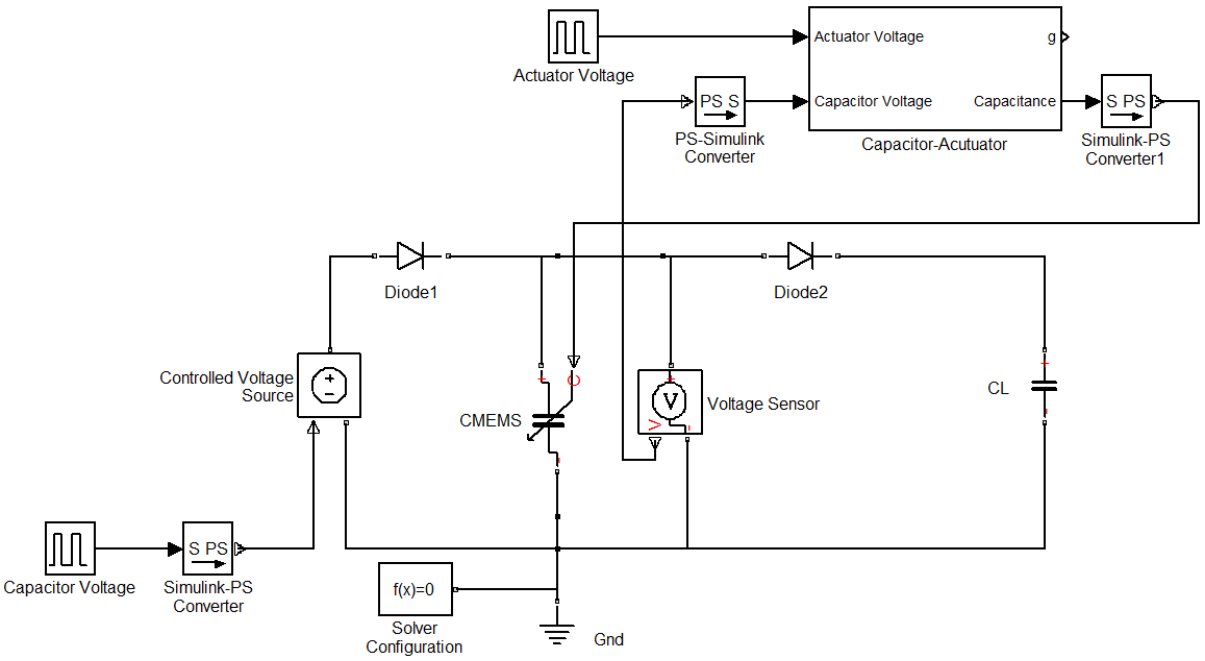

Figure 3-18 Simulink model of complete MEMS converter system. The use of Simscape electronic components greatly simplifies the modelling of the control circuit.

Originally, this system was designed for the capacitor to be charged from a 24V constant voltage, however, a coupling capacitance between the capacitor and actuator, which was initially assumed to be negligible, was measured to be 3.2pF during the evaluation of the fabricated devices. This is shown in figure 3-13. This coupling is due to the addition of boundary elements around the electrode block pad in the mask design process. This capacitance link means that while one capacitive element (actuator or capacitor) is active, the other must be grounded or it will be indirectly charged. Therefore these capacitor elements were powered from non-overlapping voltage signals.

The output voltage of the Simulink model is shown in figure 3-19. It is necessary to have a large load resistance (≈1GΩ). If a load resistance lower than this value is used, current will leak through the load resistor instead of the load capacitor. This is the reason for the reduction in output voltage. In figure 3-20, it can be seen that by lowering the load resistance to 100MΩ, the output voltage is significantly reduced.

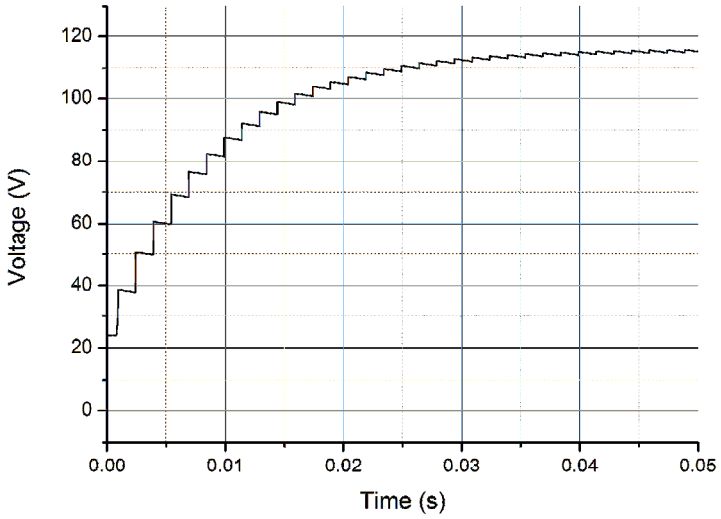

Figure 3-19 Resulting output voltage from Simulink model of bi-stable converter device. The maximum voltage peak is at 116V due to diode forward voltage drop. The load is purely capacitive i.e. infinite load resistance.

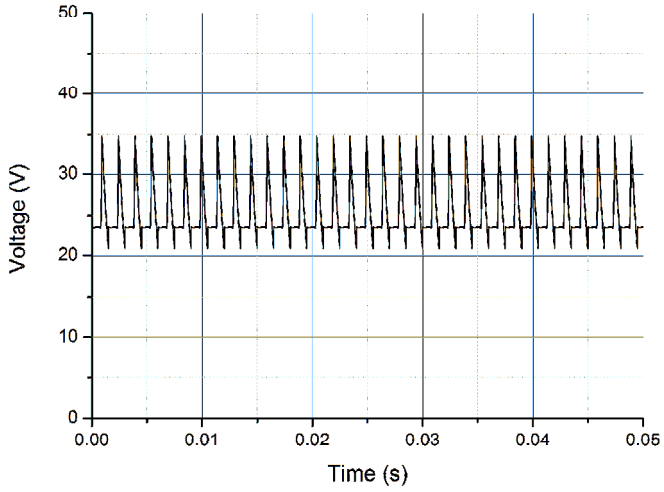

Figure 3-20 Effect that reducing the load resistance to 100MΩ has on the output voltage of the bi-stable converter device.

The output voltage shown in the figures above is for an ideal capacitor which exhibits no parasitic capacitance (C_P). As discussed in the previous section relating to FEM simulations, there is a significant contribution of parasitic capacitance due to fringing fields which will affect the overall capacitance of the device and prove to be a significant attenuating factor in the output voltage of the system. The load resistor also plays a key role in determining the

power efficiency of the system. The electrical efficiency can be calculated using the following formulae:

$$V_{OUT} = V_{IN}.\left(M + \frac{C_P}{C_{MIN}}\right)\left(\frac{R_L C_{MIN} f_{CLK}}{R_L(C_{MIN} + C_P)f_{CLK} + 1}\right) \quad 3\text{-}14$$

$$P_{CAP} = \frac{{V_0}^2}{R_L}\left(\frac{R_L(C_{MIN} + C_P)f_{CLK}}{R_L(C_{MIN} + C_P)f_{CLK} + 1}\right) \quad 3\text{-}15$$

$$P_{ACT} = \frac{C_a V_a^2 f_{CLK}}{2} \quad 3\text{-}16$$

$$\eta = \frac{P_{OUT}}{P_{Act} + P_{Cap}} \quad 3\text{-}17$$

Where C_a is the maximum value of capacitance of the actuator, V_a is the actuator voltage, f_{CLK} is the frequency of actuator switching, η is the electrical efficiency and P_{OUT} is the power taken across the load circuit. According to [30] an approximation of this is given by:

$$P_{OUT} = \frac{V_0^2 R_L}{(R_L + R_S)^2} \quad 3\text{-}18$$

Here, V_0 is the effective output voltage and R_S is the source resistance given by equations 2-5 and 2-6 respectively. Using these above equations, an approximation of output voltage and electrical efficiency can be generated with respect to load resistance. This is shown in figure 3-21. The parasitic capacitance adds ≈1.5pF to the minimum capacitance level and ≈4pF to the maximum capacitance level. For the sake of simplicity in further simulations in this thesis, a fixed parasitic capacitance of C_P = 3pF will be used. This would result in M=2.4.

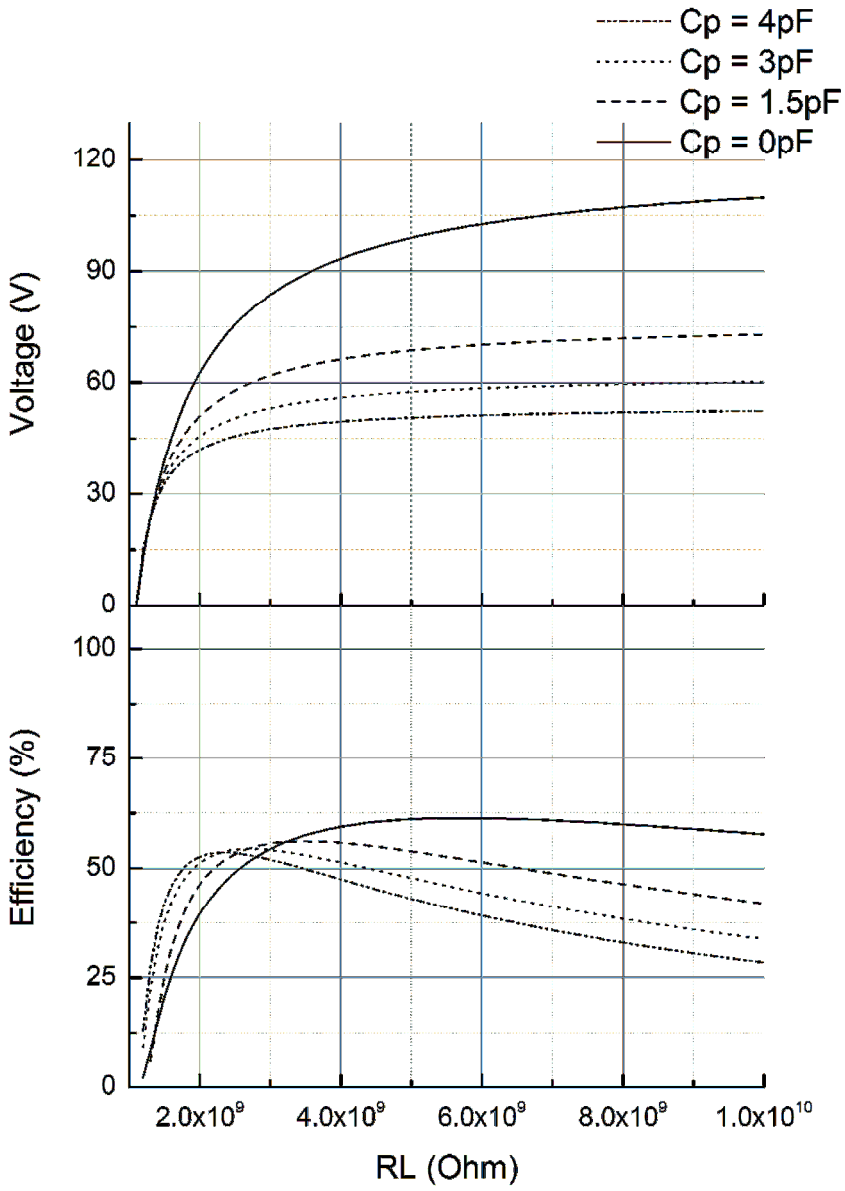

Figure 3-21 Matlab plot of electrical efficiency and output voltage vs. load resistance, for bi-stable converter device.

The actuator power term, P_{ACT} is independent of load resistance unlike the power delivered to the capacitor, P_{CAP}. It is critical to note here V_0^2 that the capacitor power depend on the ratio of effective output voltage to load resistance:

$$P_{CAP} \propto \frac{V_0^2}{R_L} \qquad 3\text{-}19$$

A plot of this relationship between effective voltage and load resistance is shown in figure 3-22.

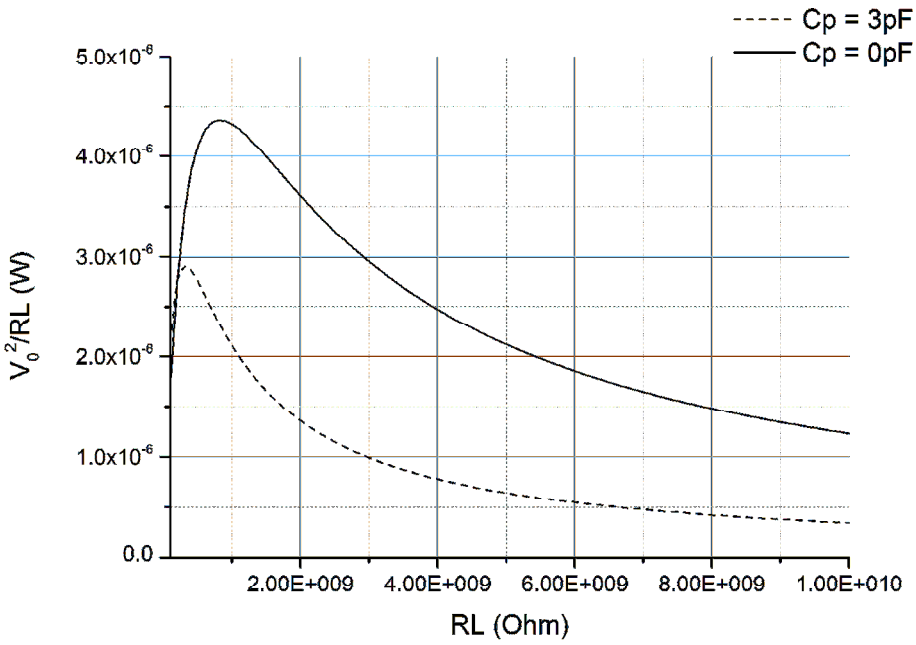

Figure 3-22 Matlab plot of relationship between effective voltage and load resistance for bi-stable converter device.

It would follow that due to the constant power level supplied from the actuator, the efficiency will not increase proportionately with increasing load resistance. It can be seen from figure 3-21 that a maximum theoretical efficiency of 61% is obtained with a 5GΩ load resistance, assuming no parasitic capacitance. At this point, a maximum effective output voltage of 101V can be extracted. As the load resistance increases beyond this point, the maximum achievable efficiency drops. However, a higher load resistance is required for larger voltage outputs. Therefore there is a trade-off between efficiency and output voltage. This graph also shows the decreasing effect parasitic capacitance has on the maximum achievable voltage whilst efficiency is not greatly affected by parasitic capacitance.

3.6.2 Circuit Level Analysis in Multisim Spice Simulator

Multisim is a Spice™ simulator which allows for further system modelling of the MEMS converter circuit with greater accuracy on the electrical components. The models constructed in Simulink form the basis for the Multisim modelling. It is possible to use Analogue Behavioural Model (ABM) components as function blocks in the construction of the mass-spring-damper system. In both the bi-stable and resonant converter circuits, a voltage controlled capacitor is used to model the MEMS capacitor. The modelling of mechanical

elements as electrical systems results in inaccurate efficiency measurements. Therefore, the Multisim simulations are only capable of producing output voltage measurements.

As discussed in [4], the junction capacitance from the diodes adds to the overall capacitance level of the system and so can be viewed as a parasitic capacitance. For the simulations in this thesis, 1N4148 diodes are used in place of D1 and D2 in figure 3-1. These diodes were chosen as they feature a relatively low level of junction capacitance (1pF) compared with other commercially available diodes. This junction capacitance, which is considered to be parasitic in this circuit, will cause an attenuation of the output voltage signal. This is illustrated in figure 3-23 where the output using 1N4148 diodes is compared against the output if virtual diodes are used.

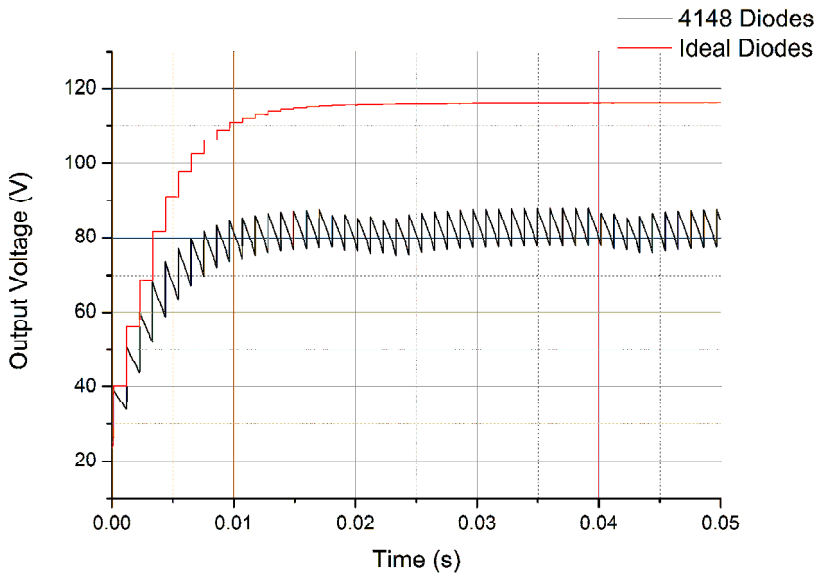

Figure 3-23 Output voltage of MEMS converter circuit, (red) ideal virtual diodes are used; (black) non-ideal 1N4148 diodes are used. Infinite load resistance and ideal capacitor (M=5) are assumed.

When a load resistor is connected to the circuit, further attenuation of the output voltage occurs, as was the case for the Simulink simulations. Figure 3-24 shows the effect a load resistance has on the output voltage. A 100MΩ load resistor has been connected to the circuit which models a typical oscilloscope measurement probe. It will be necessary to connect a measurement probe to the prototype circuit to view the output voltage waveform and so it is necessary to model this resistance before the measurement.

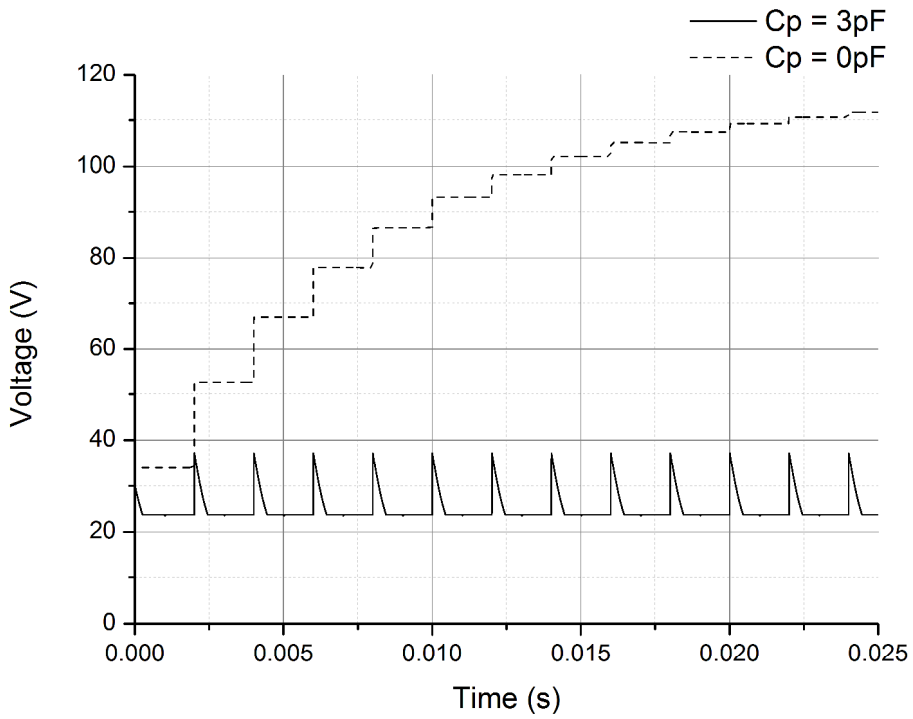

Figure 3-24 Output voltage of bi-stable device. (dashed) ideal output with infinite load resistance and no parasitic capacitance i.e. M=5, (solid) output with 100MΩ load and C_p=3pF.

Increasing the load resistance to the level necessary to prevent spiking (>1GΩ) is difficult to implement given the restrictions of measurement equipment. An alternative solution lies in increasing the capacitance of the variable capacitor. This is easily achieved by cascading multiple existing MEMS variable capacitor devices in parallel. However, in future design revisions of the MEMS variable capacitor, the capacitance can be increased by increasing either the number of capacitor electrodes (N) or the overlap gaps (i.e. g_{MIN} and g_{MAX}). In figure 3-25, it can be seen that the output voltage increases exponentially with the capacitance of the variable capacitor.

For the purpose of simplicity, four existing MEMS devices were connected in parallel for measurement in this paper. This results in a theoretical C_{MAX} and C_{MIN} of 43.4pF and 18.36pF respectively. The output voltage for this setup is shown in figure 3-26. No more than 4 devices could fit on a single PCB die used during wirebonding.

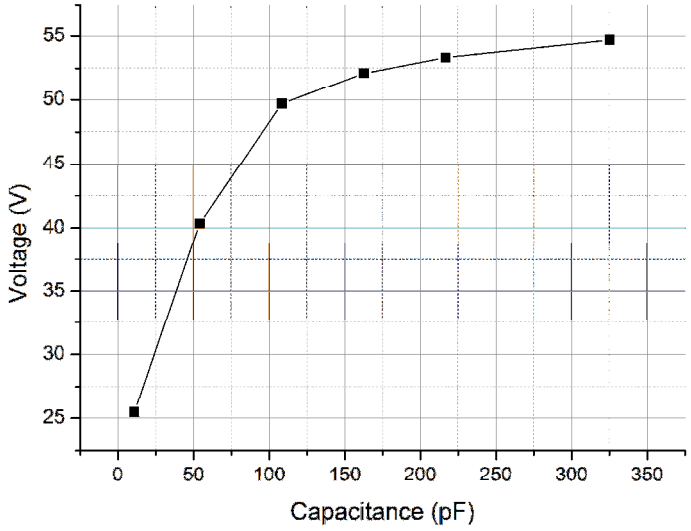

Figure 3-25 Output voltage versus maximum capacitance of C_{MEMS}. As the capacitance level increases, the output voltage increases exponentially. C_L = 100pF and R_L = 100MΩ.

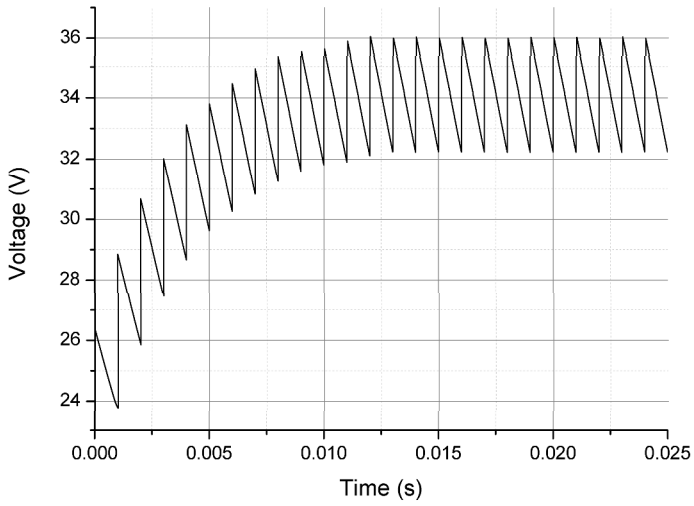

Figure 3-26 Output voltage with four C_{MEMS} devices connected in parallel. The maximum output voltage is 36V for this configuation.

Thus far, the capacitor and actuator pulsing voltage has been modelled using an ideal voltage pulse element. In reality, separate circuitry needs to be developed to create a pulsing square wave from a 24V DC input. Originally, a large test circuit was constructed which consisted of a 555-timer, a CMOS inverter and MOSFET switches to provide the non-overlapping control signals for the actuator and capacitor. While this circuit functioned well, the input power

required for the system was 1.7W. This power level is too high given the main requirement for energy harvesting systems, which typically output µW-mW levels of power, is for a low power solution to maximise electrical efficiency. As a result, an attempt to design a lower power solution was undertaken. A transistor a-stable oscillator test circuit was chosen and is shown in figure 3-27. This circuit provides a pulsing voltage for the capacitor and an inverse pulsing voltage which is supplied to the actuator. The power requirement of this circuit is ≈50mW. Again this could be improved on in future design iterations. However, for this work, it was suitable to prove the step-up operation of the MEMS devices.

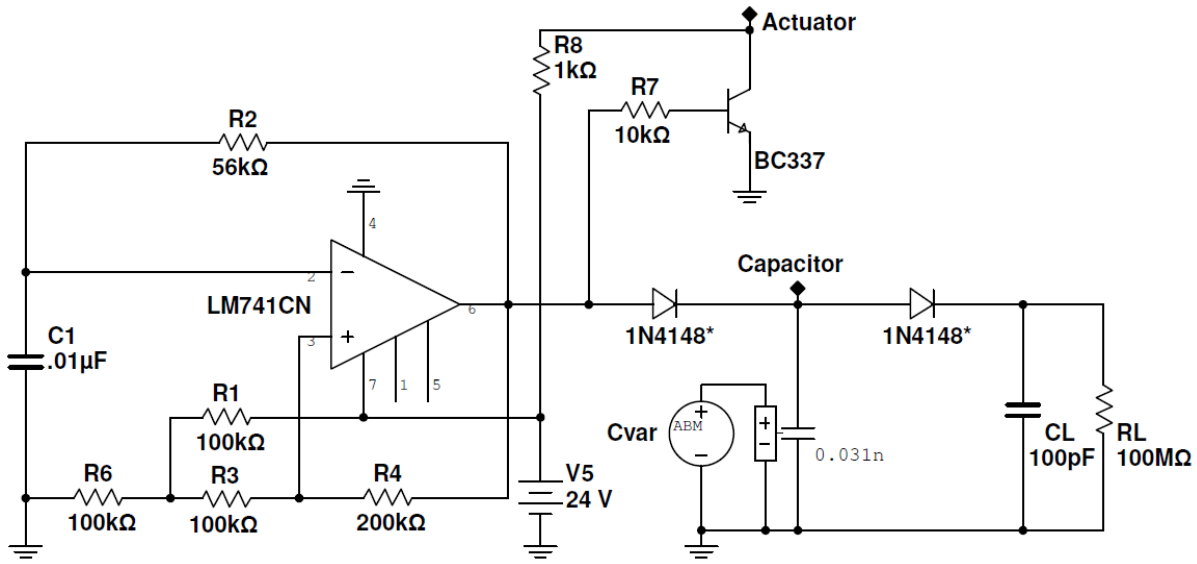

Figure 3-27 Full control circuit for bi-stable MEMS voltage converter. The pulsing voltage to the actuator and capacitor is created using an a-stable multivibrator circuit

The output voltage for this circuit is shown in figure 3-28. This output reaches a maximum level of 37.5V.

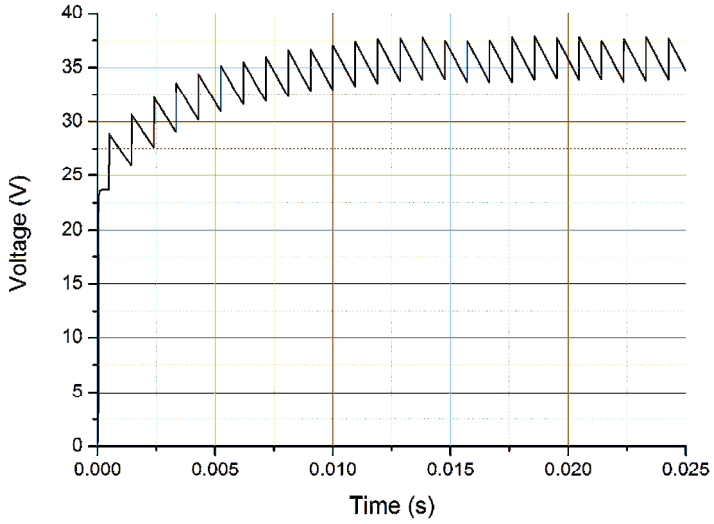

Figure 3-28 Output voltage for control circuit shown in figure 3-27.

3.7 Summary

This concludes the overview of the main simulations carried out on the bi-stable converter devices. The basic functionality was tested using system level simulations and the model used for these simulations was verified using FEM simulations. The FEM simulations provide results for resonant frequency and capacitance variation at maximum, minimum and rest electrode gap positions. The resonant frequencies of the devices match the calculated value closely while the capacitance simulations do not match their theoretical calculated values as there is a significant level of parasitic capacitance present.

The parasitic capacitance of the capacitor's fringing fields cause substantial attenuation in the maximum achievable multiplication factor. This parasitic capacitance can be reduced by increasing the overlap distance between electrodes for the comb capacitor. By increasing these dimensions, however, the actuator must also increase to compensate for the increased electrostatic forces. This will result in a physically larger end device. The devices were designed to feature a multiplication factor of M=5, but simulation shows that parasitic capacitances reduce this to M=2.83.

Further system level simulations are conducted using Simulink and Multisim to verify circuit operation. To simplify simulations, the parasitic capacitance is taken to be a fixed 3pF capacitance, this reduces the multiplication factor even further to M=2.4. These circuits are analysed in terms of output power and electrical efficiency. A prototype circuit is then presented which has been constructed using off the shelf components. From the above results, there is a clear trade-off between electrical efficiency and maximum achievable multiplication.

Choosing the correct value of load resistance based on the levels of variable capacitance is of critical importance. For the devices featured, a load resistance >1GΩ is required in order to achieve a stable output voltage as the variable capacitor exhibits relatively low levels of capacitance (≈pF) resulting in current leakage if too low a resistance value is used. This can be rectified in further designs by increasing the dimensions of the capacitor to allow for a greater capacitance level.

As the circuits will eventually be constructed and tested using standard measurement equipment, a 100MΩ load resistance was chosen as it models a typical oscilloscope probe. Therefore it was necessary to increase the effective level of variable capacitance by cascading multiple capacitors in parallel to reduce the effect of the leakage. Simulations show that if the capacitance level were to increase, the output voltage would increase exponentially until the maximum output is reached. For the bi-stable device, with four devices connected in parallel, a maximum estimated output voltage of ≈36V was reached.

The maximum achievable output voltage is set by the multiplication factor. However, this multiplication factor is affected by parasitic capacitances within the circuit. There are two main sources of parasitic capacitance; the junction capacitance of the diodes and the fringing field capacitance of the comb capacitor. Again in future iterations of this design, the effects of the parasitic capacitance of the comb capacitor can be reduced by altering the dimensions of the capacitor (e.g. increasing the overlap distance between electrodes). Similarly, by increasing the dimensions/capacitance level of the variable capacitor, the parasitic effects of the diodes would be lessened too.

The next chapter of this thesis details the theoretical work involved in designing the resonant MEMS converter.

Chapter 4 Models and Performance of Resonant MEMS Voltage Converters

4.1 Introduction

This chapter presents the theoretical work conducted in the designing of the resonant MEMS voltage converters. The operation of this device is similar to the bi-stable device presented in the previous chapter. The key difference between the two devices presented in this work is the method of actuation by which the capacitor electrodes are separated. For the bi-stable device, an electrostatic actuator is employed while the resonant device relies on the force from ambient vibrations. This resonant converter would be suited for integration with mechanical energy harvesters e.g. vibration. The VIBES generator presented in the literature review section of this thesis ideally operates at a frequency of 53Hz and acceleration level of 3.7ms-2. While this provides an interesting set of target parameters for the MEMS converter device, for the sake of simplicity, these design constraints can be somewhat relaxed. The resonant device presented in this chapter has been designed for a low voltage vibration harvester which would feature an output voltage of 0.5V at frequencies lower than 300Hz.

There are several issues associated with the design of the resonant MEMS converter. The main issue is the low capacitance level (<5pf). At this capacitance level, a large load resistance (≈TΩ) is required to produce an output voltage. Given that the output impedance of the VIBES generator, for maximum power transfer, is reported as being 4kΩ, it would follow that the load resistance of the voltage converter circuit should match this impedance for maximum efficiency. This is possible in future design iterations but will require a larger capacitance level than the devices presented in this thesis.

In addition to this, choosing suitable diodes for the control circuit is not trivial as the junction capacitance contributes a significant amount to the overall capacitance level. Therefore, a

modified version of the resonant MEMS converter is also presented in this chapter. This modified converter improves on many of these design issues. It features a higher capacitance level and a lower spring constant to reduce resonant frequency and the level of ambient acceleration needed for full actuation. The modified device was also designed to feature integrated MEMS switches to replace the diode switching elements in the control circuit. This should reduce the overall level of parasitic capacitance in the circuit.

This chapter presents the design of the MEMS variable capacitor unit using system level and 3D FEM simulations. A test circuit is then presented and analysed using Simulink and Spice™ simulations.

4.2 Dynamic Response

In the resonant design, the parallel plate actuator of the bi-stable design is replaced by a proof mass. The conceptual diagram is shown in figure 4-1. The ambient vibrations generate a force to deflect the proof mass ($F=ma$). As the proof mass actuator moves, so too do the moveable comb capacitor electrodes.

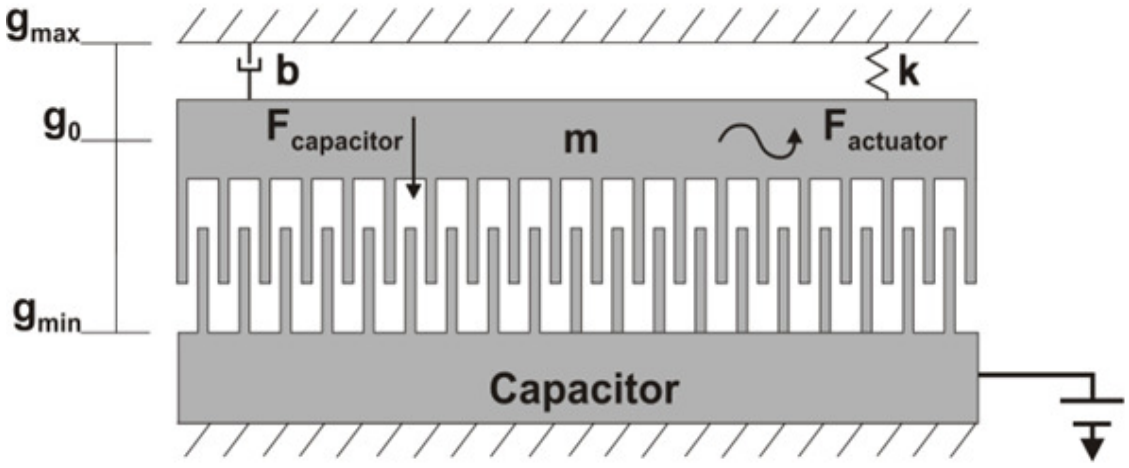

Figure 4-1 Resonant converter conceptual diagram. An external vibration, Fext, causes displacement of the proof mass. This movement causes the overlap electrode gap to vary between g_{MAX} and g_{MIN}. The capacitor is charged by a time varying voltage Φ, the output of a vibration energy harvester.

The 2nd order differential equation of motion, for this resonant system, becomes

$$mg'' + bg' + k(g_0 - g) = m\omega^2 Y sin\omega t \quad 4\text{-}1$$

Where Y is the vibration amplitude and ω is the angular frequency of the vibration [29]. For the electromagnetic generator and voltage converter, maximum power is transferred when the frequency of the vibration is equal to the resonant frequency of the device i.e. $\omega = \omega_0$. Therefore the resonant frequency of the voltage converter is designed to match the resonant frequency of the vibration harvester. The VIBES energy harvester, discussed in chapter 2 of this thesis, produces 0.5V from a 3.7ms^{-2} amplitude vibration at 120Hz. Therefore, the design target for the resonant device is to achieve full electrode deflection from this level of vibration.

In the first design iteration, the resonant device featured a relatively small number of capacitor electrodes (N=200) and, therefore, exhibits low levels of capacitance (<5pF). As the project progressed, it was clear that these capacitance levels were too low to provide any voltage multiplication. In addition to this, the acceleration level required for full actuation was 70ms^{-2} which can be reduced by lowering the gap size, spring constant and increasing the proof mass. In order to rectify the issues with the original resonant design, a modified version of this device was developed. This modified device featured a greater number of electrodes (N=800), lower resonant frequency and a lower range of travel between g_{MIN} and g_{MAX}. The resonant devices have been designed for low voltage inputs and therefore require a low voltage switch to control the charging and discharging of the capacitor. The modified resonant devices features integrated MEMS switches to overcome this issue. This will be discussed in the circuit design section in the next chapter of this thesis.

4.3 Design Considerations

The design considerations for the resonant device are similar to that of the bi-stable. The general modular spring structure remains the same in both designs with calculation methods for damping, resonant frequency, mass and spring constant remaining the same as in the previous chapter. The key difference between the devices is that the resonant design features a lower value of spring constant as the system operates from low frequency, low amplitude

ambient vibrations. For the resonant design, this was chosen to be 2N/m but this was further reduced to 1N/m in the modified resonant design.

Reducing the spring constant, while maintaining the same proof mass dimensions, lowers the level of vibration amplitude required to achieve full electrode displacement. However, despite the spring constant for the modified resonant device being relatively low (1N/m), the vibration amplitude required to drive the device is $15ms^{-2}$ which is higher than the resource available from the VIBES generator. This is due to the distance of travel between the electrodes (21µm from g_{MAX} to g_{MIN}). A lower distance of travel results in a lower multiplication value; this is a key design trade off. As a proof of concept, $15ms^{-2}$ was considered to be an acceptable level of acceleration.

4.4 Performance

The resonant design features key structural differences, in comparison to the bi-stable design; namely the lack of actuation electrodes and the addition of proof mass dimensions. As this design is to operate at low frequencies (<300Hz), it is necessary to have a low spring constant and/or large mass. In the case of this design, both of these parameters were varied to achieve the correct resonant frequency while trying to maintain surface area at a minimum. These design parameters are shown in table 4-1.

Not all the design parameters were met in order to satisfy integration with the MEMS converter devices and VIBES energy harvesting devices presented in the literature review section of this thesis. For example, the resonant MEMS feature a resonant frequency of 294Hz while the VIBES generator will resonant at 53Hz. It is possible to design a converter that will match the resonant frequency/acceleration level/impedance level of the VIBES generator; however, many of these parameters are mass dependent and so this would result in a larger overall device structure. In order to simplify the design, these parameters are considered secondary in this design process. The resonant converter presented in this thesis has been designed predominantly to prove that low voltage multiplication is possible without the need for electrical actuation. This design can be optimised further to address issues in resonant frequency, acceleration and impedance matching.

The original resonant design featured key design issues. In particular, the capacitance level at g_{MIN} and g_{MAX} was too low (<5pF) to provide any multiplication for the measurement equipment load (100MΩ). The next section of this chapter will demonstrate that a load resistance of ≈TΩ is required to obtain a suitable output from these devices. It was necessary to redesign these devices to solve the key issues associated with the original design. As a result, the modified resonant device was designed. This device features a greater number of capacitor electrodes reducing the load resistance requirement. The device also achieves full gap displacement at lower vibration amplitude and resonates at a lower frequency than the original device. This puts it a step closer towards being an ideal match for the VIBES generator. The parameters of this redesigned device are shown in table 4-2.

Table 4-1 - System parameters and dimensions for resonant converter device.

Parameter	Value	Unit	Description
			Fixed Variables
g_{MAX}	10	µm	Minimum overlap distance between capacitor electrodes
g_{MAX}	50	µm	Maximum overlap distance between capacitor electrodes
g_0	30	µm	Overlap distance between capacitor electrodes at rest
$g_{overlap}$	3	µm	Gap between capacitor electrodes.
L_{comb}	70	µm	Length of capacitor comb fingers
W_{comb}	7	µm	Width of capacitor comb fingers
L_{mass}	1200	µm	Length of actuator parallel plates
W_{mass}	3300	µm	Width of actuator parallel plates
N_{comb}	200	-	Number of capacitor electrodes
h	50	µm	Structural silicon thickness
			Calculated Variables
m	4.3e-7	Kg	Mass of moveable structure
k	1.7	N/m	Spring constant
f	294	Hz	Resonant frequency of device

Table 4-2 - System parameters and dimensions for modified resonant converter device.

Parameter	Value	Unit	Description
			Fixed Variables
g_{MIN}	7	µm	Minimum overlap distance between capacitor electrodes
g_{MAX}	35	µm	Maximum overlap distance between capacitor electrodes
g_0	21	µm	Overlap distance between capacitor electrodes at rest
$g_{overlap}$	3	µm	Gap between capacitor electrodes.
L_{comb}	70	µm	Length of capacitor comb fingers
W_{comb}	7	µm	Width of capacitor comb fingers
L_{mass}	1500	µm	Length of actuator parallel plates
W_{mass}	4300	µm	Width of actuator parallel plates
N_{comb}	800	-	Number of capacitor electrodes
			Calculated Variables
m	9.2e-7	Kg	Mass of moveable structure
k	0.98	N/m	Spring constant
f	165	Hz	Resonant frequency of device

4.4.1 Simulink System Level Analysis

The Simulink model presented in the previous chapter for the analysis of the bi-stable device can also be used to analyse the behaviour of the resonant device. However, there is a difference in that the resonant device does not have an electrical actuator element to generate an electrostatic force. The actuator in this case is an ambient vibration which is modelled using the fundamental expression $F=ma$. In this case F is the resulting actuating force, m is the mass of the moveable structure and a is the acceleration of the ambient vibration modelled using a sine wave block. The resulting electrode displacement and capacitance variation for the original resonant device with a $70ms^{-2}$ vibration is shown in figure 4-2. The minor non-uniformity in the start of this figure is due to a numerical anomaly in Simulink solver computation.

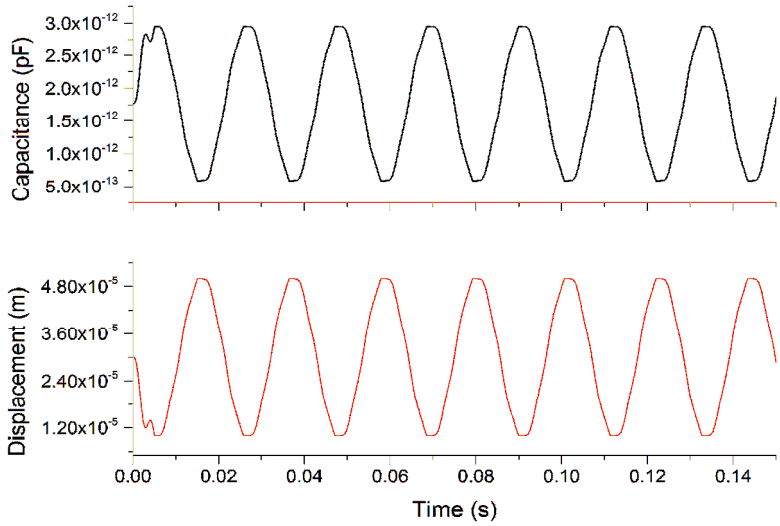

Figure 4-2 Plot of electrode displacement and resulting capacitance variation for resonant system. This displacement is the result of a 70ms^{-2} applied vibration.

By reducing the distance that the moveable electrode must travel in order to achieve full actuation, the required acceleration level will reduce too. For the modified resonant device, the electrode distance from rest to g_{MIN} or g_{MAX} is reduced from 20µm to 14µm. The spring constant is also lowered and the proof mass dimensions are increased. These changes result in a required acceleration level of 15ms^{-2} to achieve full actuation. This is shown in figure 4-3.

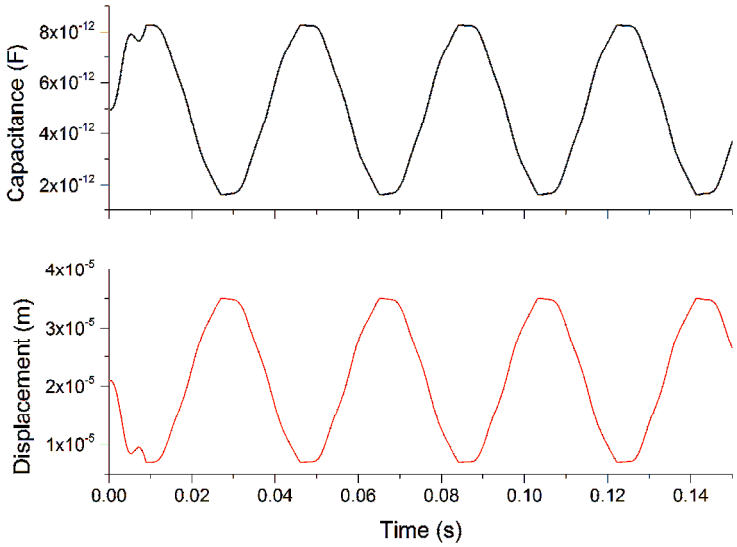

Figure 4-3 Plot of electrode displacement and resulting capacitance variation for modified resonant system. This displacement is the result of a 15ms^{-2} applied vibration.

4.4.2 MEMS+ and 3D FEM Analysis

A 3D model of the resonant device is constructed using MEMS+ in a similar fashion to the bi-stable device. The parallel plate actuator of the bi-stable device is replaced by a large block of silicon forming a proof mass. The mass of the proof mass and the spring constant must be designed with the specific resonant frequency in mind. For low frequencies this results in a large proof mass with a low spring constant. The MEMS+ layout for the original resonant device is shown in figure 4-4 while the modified resonant device is shown in figure 4-5. It can be seen that the modified resonant device contains more additional capacitor electrodes on either side of the proof mass. The modified device also has an additional electrode contained within the mechanical spring stopper. This electrode would act as a contact for integrated MEMS switches.

Again, MEMS+ was used to construct the 3D model of the devices. These were then imported into Coventorware for analysis of the resonant frequency, capacitance variation and damping coefficient.

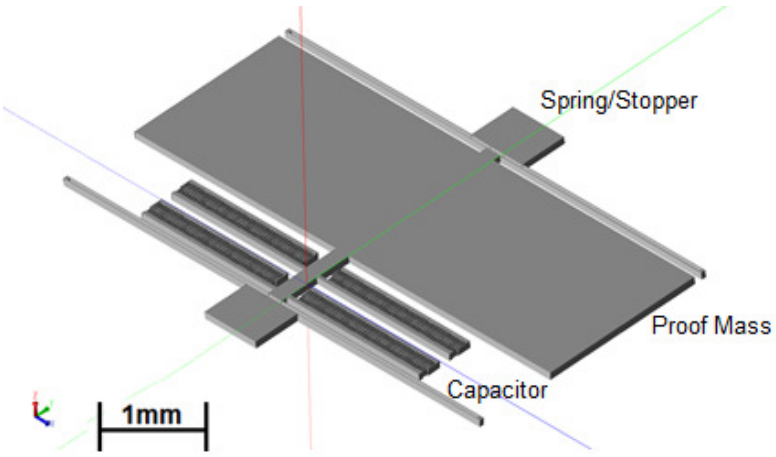

Figure 4-4 MEMS+ layout of resonant device. A proof mass replaces the parallel plate actuator of the bi-stable converter design. This proof mass will move relative to ambient vibrations and thus cause a displacement of the moveable capacitor electrodes.

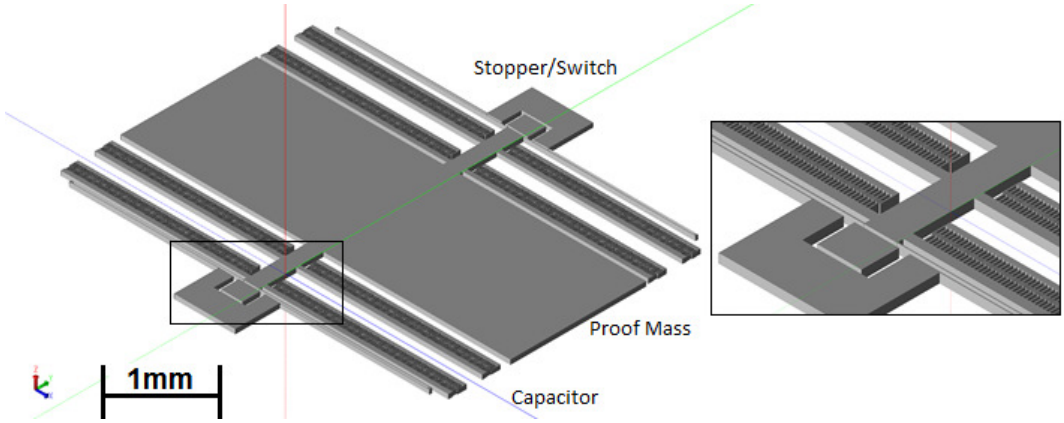

Figure 4-5 MEMS+ layout of modified resonant device. This device features integrated switches in the stopper element and more capacitor electrodes than the original resonant device.

4.4.2.1 Resonant Frequency

For a device which has been specifically designed to resonant at a particular frequency, it is vital that the calculated values and FEM simulations, for resonant frequency, are as close a match as possible. The results for a frequency analysis on the resonant and modified resonant devices are shown in figure 4-6 and figure 4-7 respectively. The resonant frequencies are found to be 294Hz, for the original resonant design, and 170Hz for the modified design. This is a good match to the calculated values of 294Hz and 165Hz.

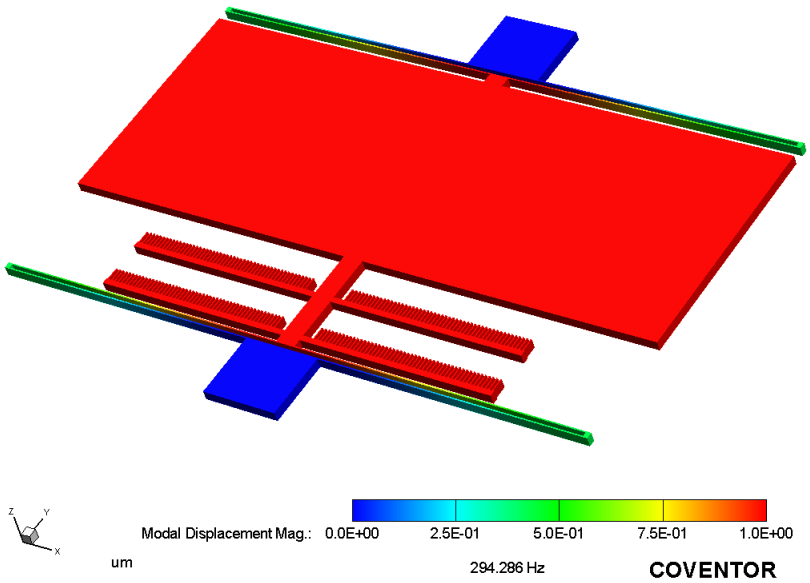

Figure 4-6 Coventorware simulation of resonant frequency for resonant converter device. The simulated resonant frequency value for a 7µm thick spring is 294Hz.

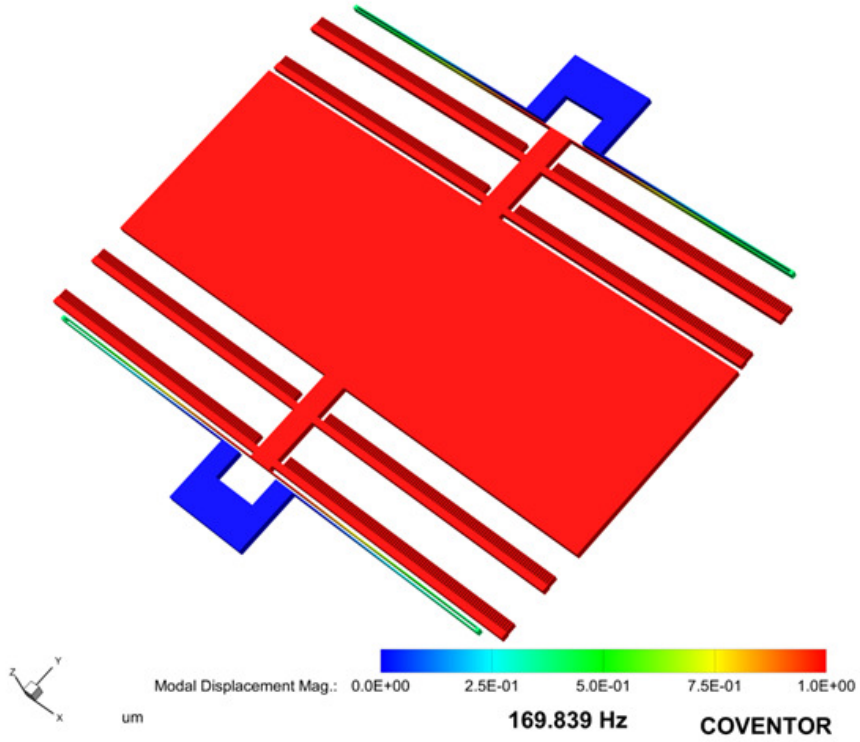

Figure 4-7 Coventorware simulation of resonant frequency for modified resonant converter device. The simulated resonant frequency value for a 7µm thick spring is 170Hz.

4.4.2.2 Capacitance

For the resonant device, unlike the bi-stable device, it is possible to increase g_{MAX} and g_{MIN} without having to consider electrostatic force as this force is considerably weaker than the actuation force generated by the proof mass. However, with higher displacement limits, the acceleration of the ambient vibration must be large enough to provide enough force to the proof mass so it can traverse the gap. This is the trade off when designing the resonant device's capacitor. In the original resonant device, the gaps were used for g_{MAX} and g_{MIN} were 50µm and 10µm respectively. This requires an acceleration of 70ms^{-2} for full actuation. The same dimensions of comb structure are used in the modified resonant device as in the bi-stable device. In this case, an acceleration of 15ms^{-2} will result in full electrode actuation.

The capacitance variation for both devices is shown in figure 4-8. This figure also illustrates the capacitance variation of the bi-stable device for comparison purposes.

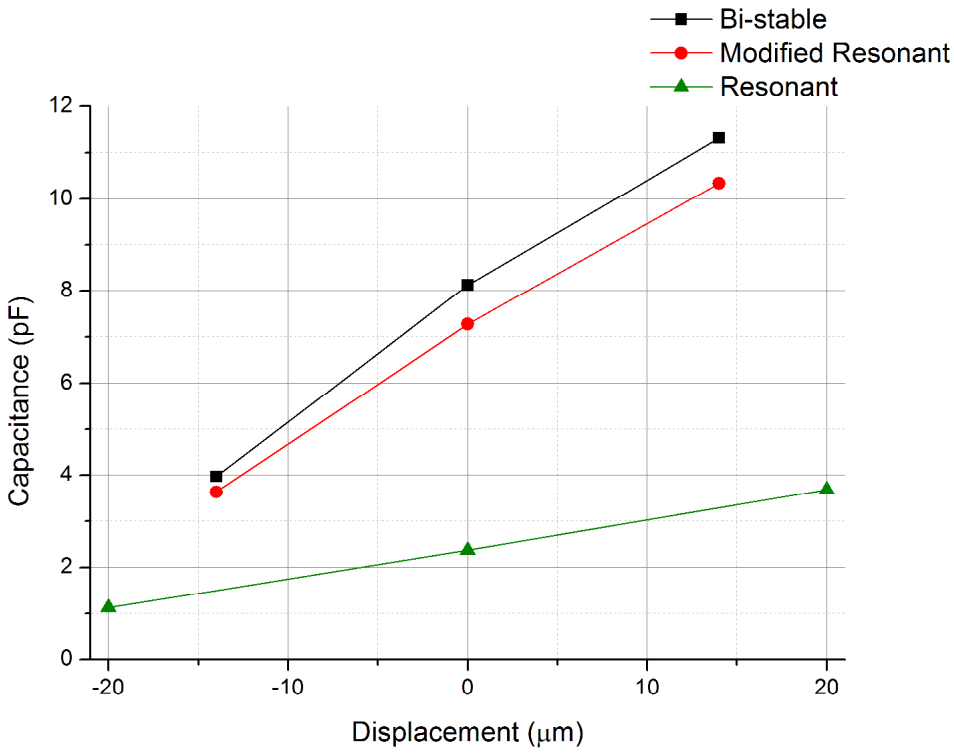

Figure 4-8 Capacitance (in pF) of bi-stable, resonant and modified resonant devices at points g_{MAX}, g_{MIN} and g_0. The capacitor electrodes are 7µm thick with a 3µm gap between them.

4.4.2.3 Damping

Again, a Stokes flow analysis was performed on a set of comb fingers as shown in figure 3-14. The resulting damping coefficient for a sample of comb fingers from the original resonant and modified resonant devices is shown in Figure 4-9. It is important to remember that the original resonant device had a larger overlap gap difference with g_{MIN} = 10µm and g_{MAX} = 50µm. For the modified resonant device, this was reduced to g_{MIN} = 7µm and g_{MAX} = 35µm.

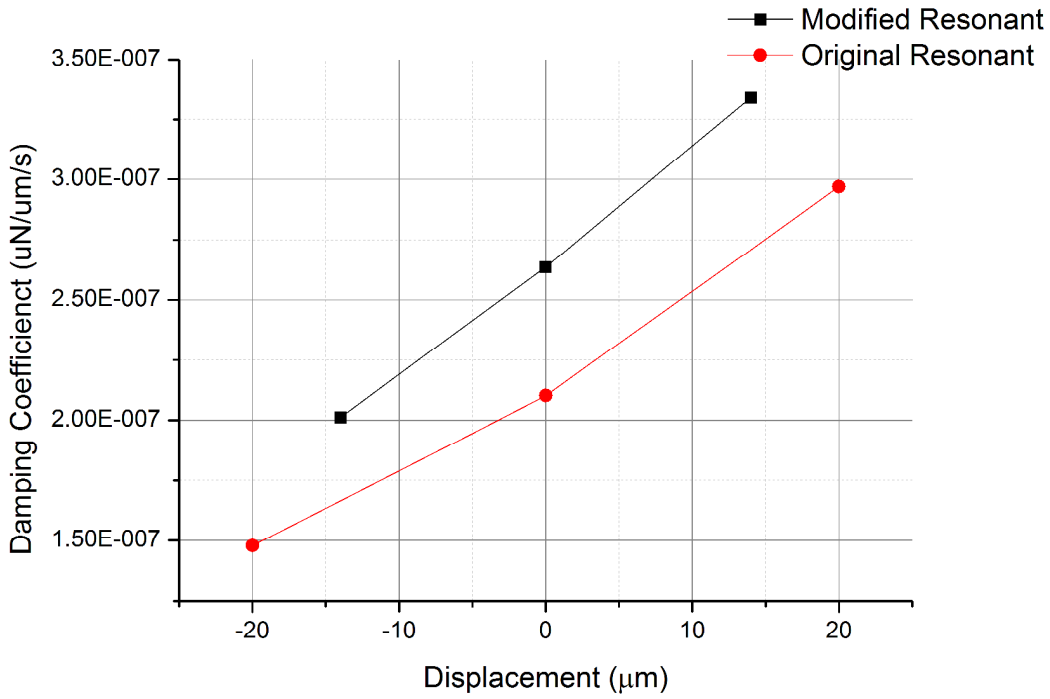

Figure 4-9 Damping co-efficient for the original resonant and modified resonant device, at points g_{MAX}, g_{MIN} and g_0.

4.5 Control Circuit

4.5.1 System Level Modelling in Simulink

The system level model for the resonant device is similar to that of the bi-stable device detailed in the previous chapter. The actuator force is also represented by a sine wave block. This sine wave models the input vibration with defined amplitude and a frequency matching the resonant frequency of the device. The force is then calculated by using the formula $F=ma$. A layout of this model is shown in figure 4-10.

The input voltage to the capacitor is modelled as a sinusoidal voltage as, typically, the output voltage of an electromagnetic energy harvester is a time varying signal. The peak of this input voltage is 0.5V and the frequency matches the resonant frequency of the device. As the input voltage is lower than in the case of the bi-stable system, the forward voltage drop of the diodes has been set to zero to model virtual diodes. Therefore, the diodes will not impact the output voltage.

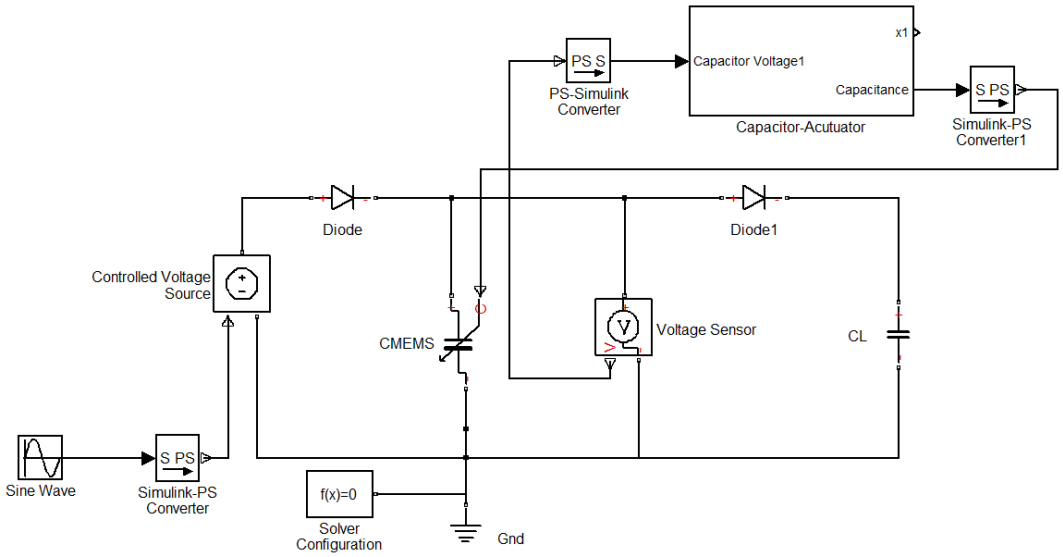

Figure 4-10 Simulink complete system overview for resonant device model. Unlike the bi-stable device, there is no electrostatic actuator element.

The output voltage for this system is shown in figure 4-11. The modified resonant devices have been designed with optional integrated switches. It was not possible to accurately model the operation of these switches for simulations, so it has been assumed that these switches are not in use. Measurement results will determine if there is an advantage to using these integrated switches over external diodes.

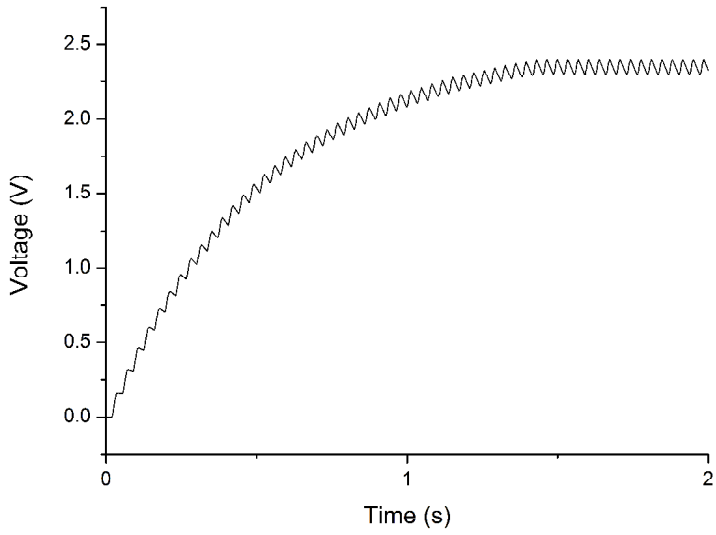

Figure 4-11 Output voltage from Simulink model of ideal resonant converter device. The maximum voltage peak is ≈2.5V from a 0.5V input voltage.

The resonant voltage converter features no electrical actuation and therefore the method used for estimating the electrical efficiency of the bi-stable converter becomes simplified to:

$$\eta = \frac{P_{OUT}}{P_{Cap}} \qquad 4\text{-}2$$

The electrical efficiency and effective output voltage results for the resonant and modified resonant devices are shown in figure 4-12 and figure 4-14 respectively.

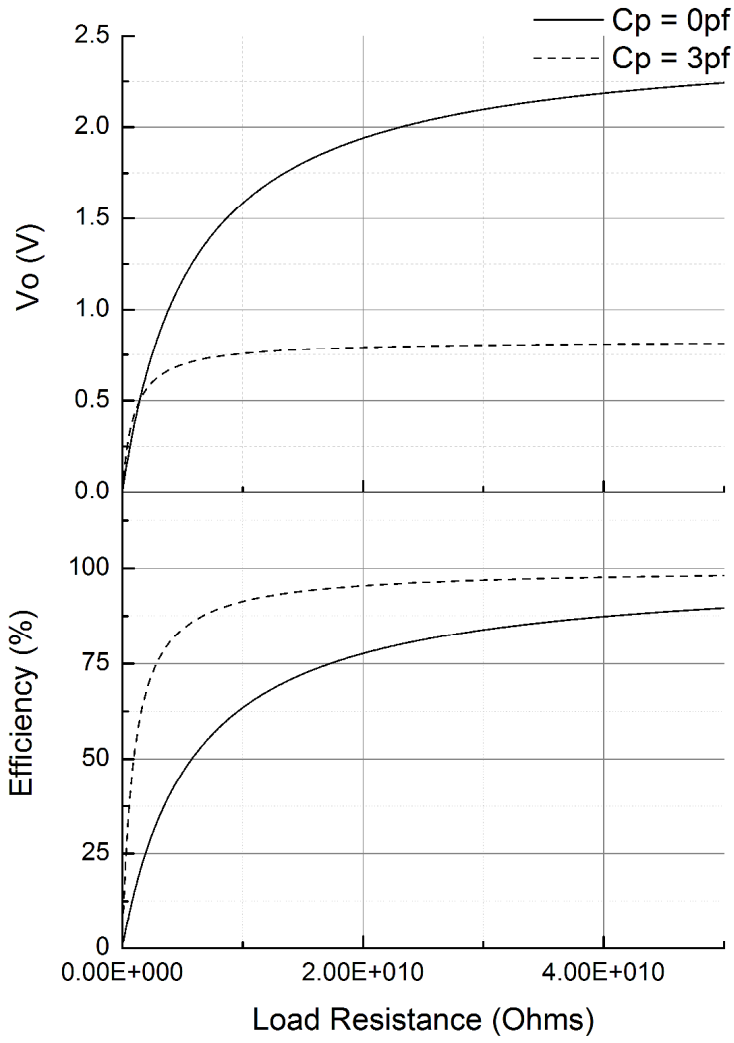

Figure 4-12 Matlab plot of electrical efficiency and output voltage vs. load resistance, for the resonant converter device.

As the constant actuator power term P_{ACT} is no longer considered, the efficiency should increase with increasing load resistance. Again, the capacitor power depends on the relationship between effective output voltage and load resistance. However, in the case of

these resonant devices, the output voltage is lower and the load resistance levels are higher than in the case of the bi-stable device, and so the resulting ratio is much lower. This can be seen in figure 4-13.

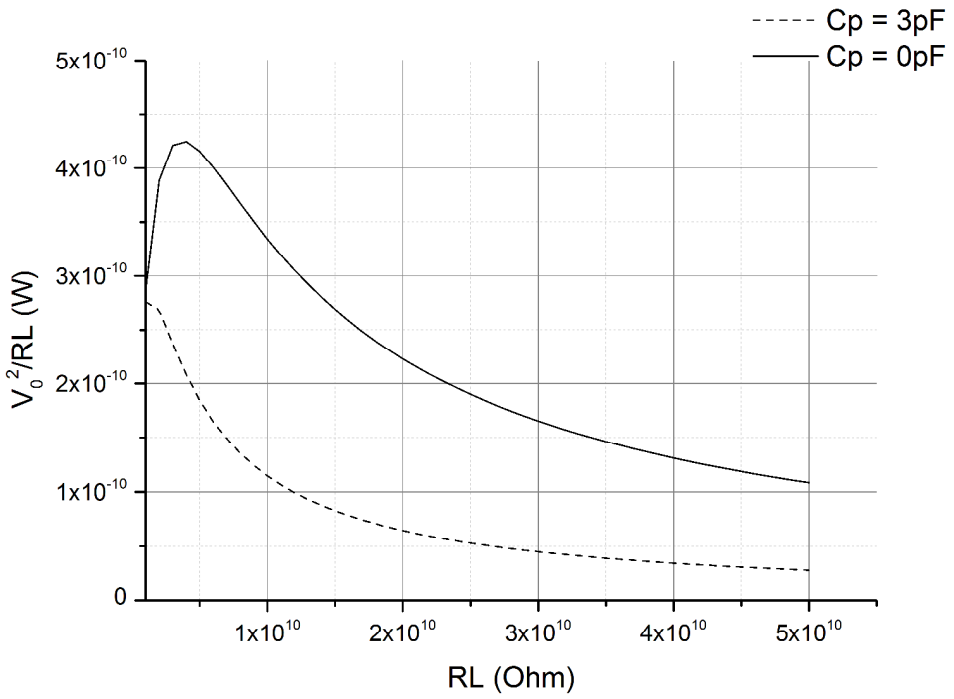

Figure 4-13 Matlab plot of relationship between effective voltage and load resistance for resonant converter device.

With increasing parasitic capacitance, the capacitor power will drop. This is due to a drop in the effective output voltage and an increase in the overall capacitance level (C_{MIN}+C_P). Therefore, the electrical efficiency increases with a greater overall variable capacitance level, including parasitic capacitance. However, with this parasitic capacitance, the output voltage drops to ≈33% of the level of the ideal output with no parasitic capacitance.

There is an increase in both the voltage output and electrical efficiency for lower load resistance levels in the modified resonant device. This is shown in figure 4-14 . This increase is due to the higher levels of capacitance independent of the parasitic capacitance.

The electrical efficiency, drops ≈5% at load resistances lower than 2TΩ, while effective output voltage is attenuated by over 50%.

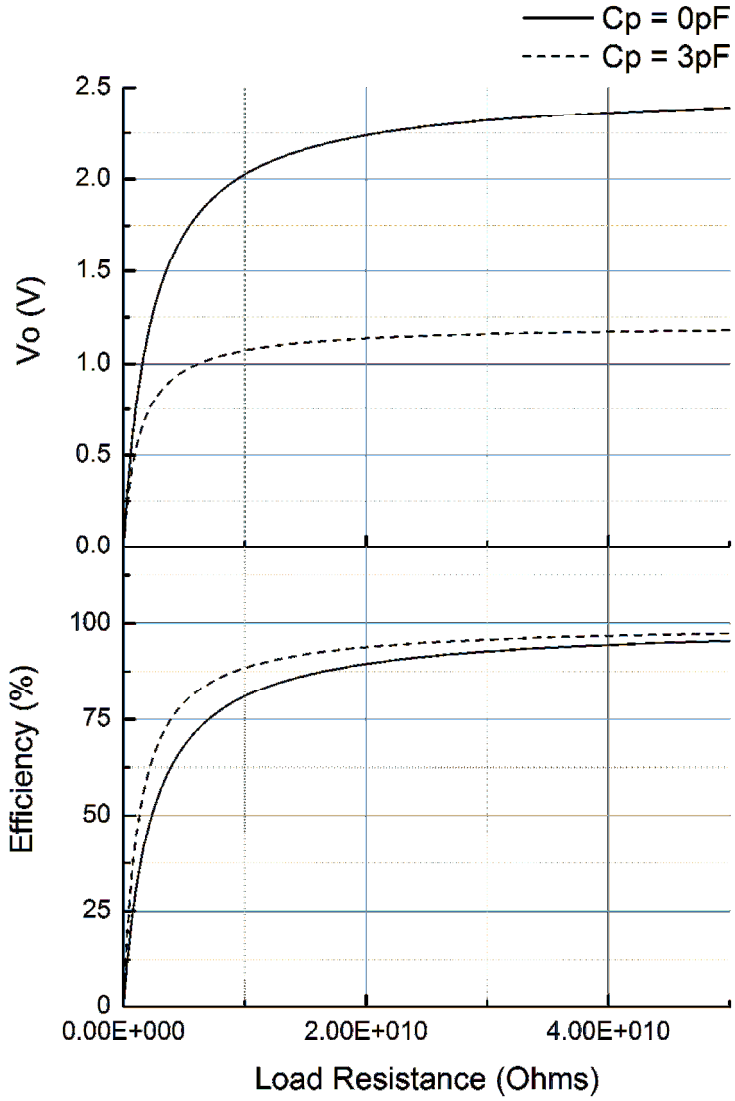

Figure 4-14 Simulink plot of electrical efficiency and output voltage vs. load resistance, for the modified resonant converter device.

4.5.2 Circuit Level Analysis in Multisim Spice Simulator

The Multisim model for the resonant design is shown in figure 4-15. The output of a vibration energy harvester will be a low voltage time varying signal. For this simulation an AC source was used which outputs 0.5Vpk-pk. The diodes and variable capacitor rectify the input AC voltage as well as isolating the charge on the variable capacitor. Schottky diodes are chosen for their low forward voltage drop (≈0.1V). However, the voltage drop will still impact the output of the circuit as the voltage to the capacitor will drop to ≈0.4V for a 0.5V input.

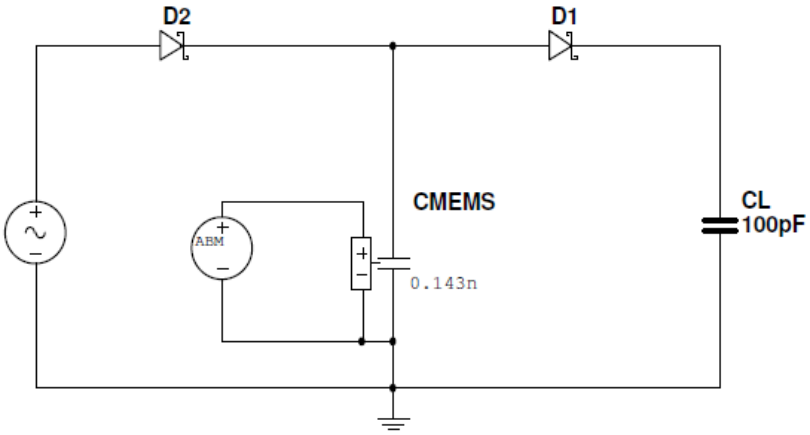

Figure 4-15 Multisim schematic of resonant control circuit. Here, the input voltage is sinusoidal to model a typical time varying voltage output from a vibration energy harvester.

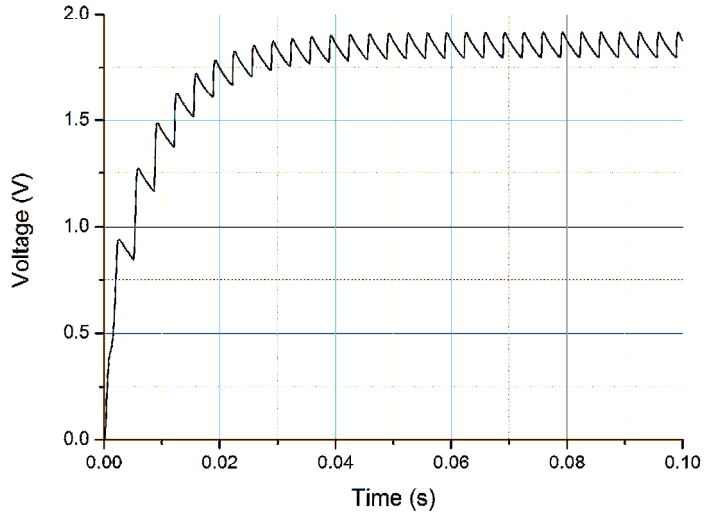

Figure 4-16 Output voltage of control circuit shown in figure 4-15 using BAT82 Schottky diodes. The peak output voltage is ≈1.9V based on an input sine wave of 500mVpk-pk. Load resistance is infinite here and no parasitic capacitance is assumed.

Again, a suitably high value of load resistance or a greater level of capacitance must be selected in order to prevent the output voltage from dropping. For a parasitic capacitance of 3pF and a load resistance of 100MΩ, figure 4-17 illustrates the increase in the output voltage as the maximum capacitance level of the variable capacitor increases.

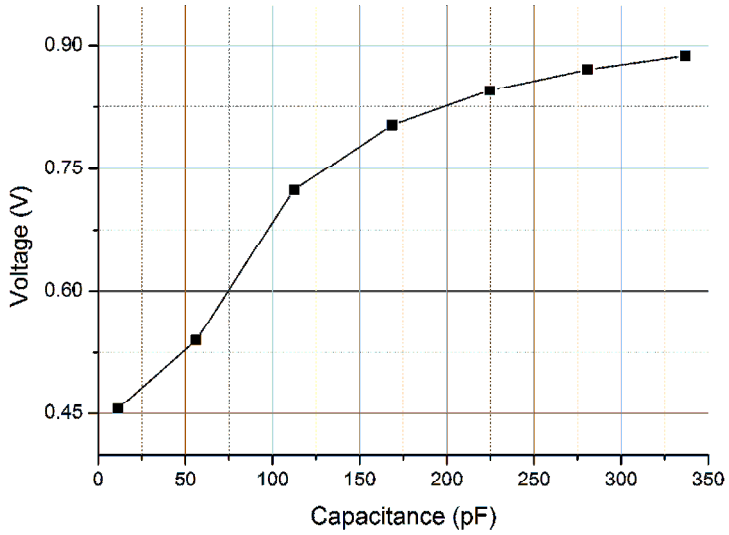

Figure 4-17 Output voltage, of resonant control circuit, versus maximum capacitance of C_{MEMS}.

The devices designed in this work exhibit a maximum capacitance of ≈4pf while the modified devices have a maximum capacitance of ≈11pf, therefore, it would be necessary to cascade many devices in parallel to achieve a reasonable voltage output. For example, in figure 4-17, 0.9V is achieved when maximum capacitance is 340pF. This is the equivalent of cascading 30 modified devices in parallel. The use of the integrated switches may improve the level of maximum output voltage as, unlike capacitors, these would have no forward voltage drop. The evaluation of these switches is detailed in the measurement section of this thesis.

4.6 Summary

This concludes the overview of the main simulations carried out on the resonant converter devices. The basic functionality was tested using system level simulations and the model used for these simulations was verified using FEM simulations. The FEM simulations provide results for resonant frequency and capacitance variation at maximum, minimum and rest electrode gap positions. The resonant frequencies of the devices match the calculated value closely which is important in the case of the resonant device which is designed specifically to

operate at a specific resonant frequency. However, the capacitance simulations do not match their calculated values as there is a significant level of parasitic capacitance present.

The parasitic capacitance of the capacitor's fringing fields cause substantial attenuation in the maximum achievable multiplication factor. This parasitic capacitance can be reduced by increasing the overlap distance between electrodes for the comb capacitor. By increasing these dimensions, however, the actuator must also increase to compensate for the increased electrostatic forces. This will result in a physically larger end device. The devices were designed to feature a multiplication factor of M=5, but simulation shows that parasitic capacitances reduce this to M=3.5 for the original resonant design and M=2.8 for the modified resonant design which has smaller electrode gaps.

Control circuit models have been developed in Simulink and Multisim to estimate the output voltage and electrical efficiency. There is a clear trade-off between electrical efficiency and maximum achievable multiplication. To simplify simulations, the parasitic capacitance is taken to be a fixed 3pF capacitance.

Choosing the correct value of load resistance based on the levels of variable capacitance is of critical importance. For the devices featured, a load resistance >1TΩ is required in order to achieve a stable output voltage as the variable capacitor exhibits relatively low levels of capacitance (<5pF) resulting in current leakage if too low a resistance value is used. This can be rectified in further designs by increasing the dimensions of the capacitor to allow for a greater capacitance level.

As the circuits will eventually be constructed and tested using standard measurement equipment, a 100MΩ load resistance was chosen as it models a typical oscilloscope probe. Therefore it was necessary to increase the effective level of variable capacitance by cascading multiple capacitors in parallel to reduce the effect of the leakage. Simulations show that if the capacitance level were to increase, the output voltage would increase exponentially until the maximum output is reached.

The maximum achievable output voltage is set by the multiplication factor. However, this multiplication factor is affected by parasitic capacitances within the circuit. There are two main sources of parasitic capacitance; the junction capacitance of the diodes and the fringing field capacitance of the comb capacitor. Again in future iterations of this design, the effects of the parasitic capacitance of the comb capacitor can be reduced by altering the dimensions

of the capacitor (e.g. increasing the overlap distance between electrodes). Similarly, by increasing the dimensions/capacitance level of the variable capacitor, the parasitic effects of the diodes would be lessened too.

Chapter 5 Fabrication

5.1 Introduction

The devices presented in this work are fabricated using an SOI process. The layout of a generic SOI wafer can be seen in figure 5-1 below. The top structural silicon layer measures 50µm in depth, this covers a 2µm silicon dioxide sacrificial layer which sits on top the silicon substrate layer. This thick structural layer offers good aspect ratios and is ideal for developing relatively large capacitor electrodes with a low surface area. The University of Southampton has a long established and well developed SOI fabrication platform and therefore, using this process was the obvious choice from an efficiency and support perspective. Previous investigations into MEMS voltage converters [27-29] also propose using an SOI process.

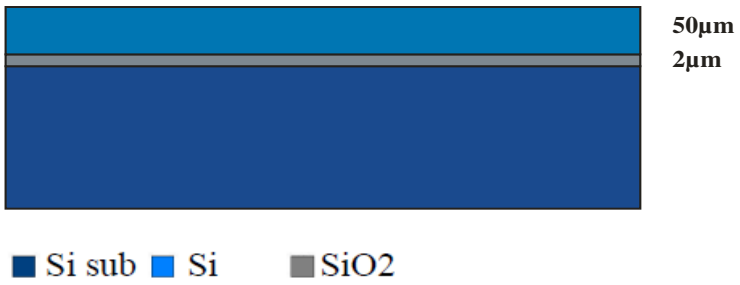

Figure 5-1 Standard SOI wafer featuring 50µm device layer and 2µm oxide layer (after Zeimpekis-Karakonstatinos, 2008, [91])

The structural silicon is often heavily doped to give a low resistivity and make the structural layer conductive. The silicon dioxide layer electrically isolates the structural silicon from the substrate layer. It also acts as an etch-stop and sacrificial layer. A typical SOI process routine is shown in figure 5-2.

A thin layer of photoresist is deposited onto the wafer using a mask pattern. A Deep Reactive Ion Etch (DRIE) is preformed to etch away the silicon layers and define the shape of the device in the structural layer. Finally, the oxide layer is removed by a HF vapour etch and the moveable structure is released.

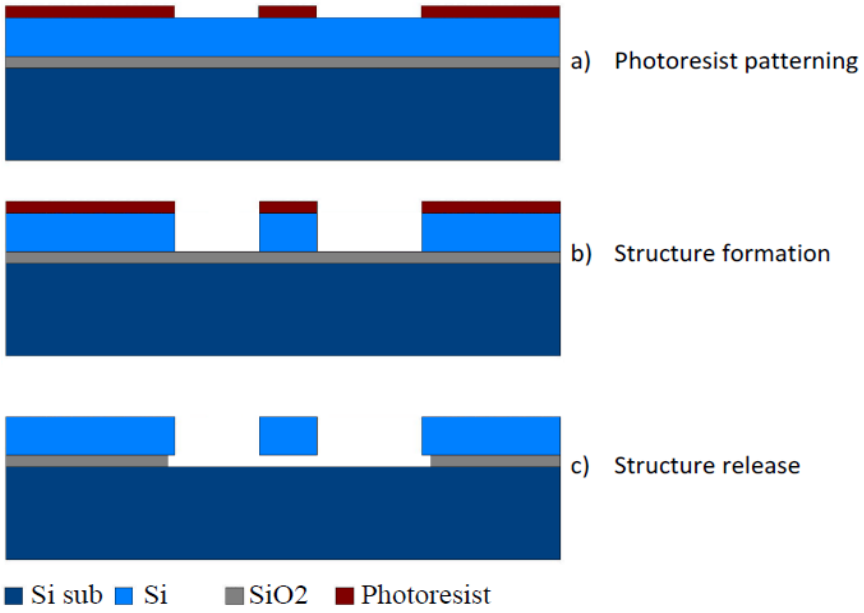

Figure 5-2 Standard SOI process: (a) device layer is patterned with resist using a mask, (b) silicon is etched away using DRIE, (c) oxide is removed using HF vapour etching (after Zeimpekis-Karakonstatinos, 2008, [91])

The final stage of the fabrication process is usually dicing. This cuts the individual devices out of the wafer. Since the mechanical components are quite sensitive to vibration, stiction etc. the devices are coated in a layer of resist to protect them during the dicing stage. However, dicing a wafer creates debris which settles on the resist. When this dicing stage is complete, and the resist is stripped in acetone, this debris can settle on the surface of the silicon causing short circuits or can block moving parts. For this reason, a dicing-free stage was proposed in [92]. This involves etching non-overlapping trenches around the device on the structural silicon layer and on the backside substrate silicon layer.

Another issue exists with using an SOI process to fabricate chips with large suspended proof masses. In previously described processes [93, 94], a proof mass greater than 3mm on each side is not possible to fabricate as the mass would bend and make contact with the substrate layer. To remedy this issue, a novel SOI process is developed in [95] which incorporates elements of the dicing free process of [92].

This process involves removing the silicon substrate layer from underneath the suspended mechanical device. This allows for larger size proof masses without the issue of stiction, it also eliminates any parasitic capacitances that may exist between the substrate and the device.

To remove this substrate, backside trenches are etched in the substrate layer and removed during the DRIE and HF vapour phase etching stages. A HF vapour phase etch is chosen over a wet release as it reduces the chance of components sticking to anchored features [96]. A top side view of these trenches can be seen in figure 5-3. Once again, the backside trenches do not overlap with the actual device area to prevent the chips from breaking off during etching.

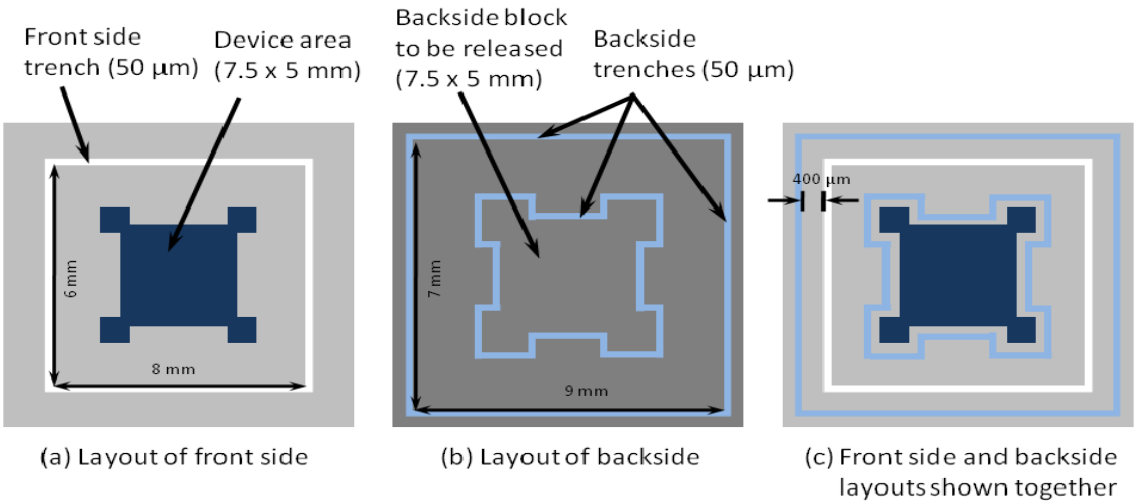

Figure 5-3 Top side views of non-overlapping trenches for dice-free etching and handle wafer removal (after Sari, Zeimpekis and Kraft, 2010, [95])

A diagram illustrating the stages of release is shown in figure 5-4. There are three release areas: i) the proof mass, ii) the handle wafer block underneath the proof mass, and iii) the outer trenches on the front and backside.

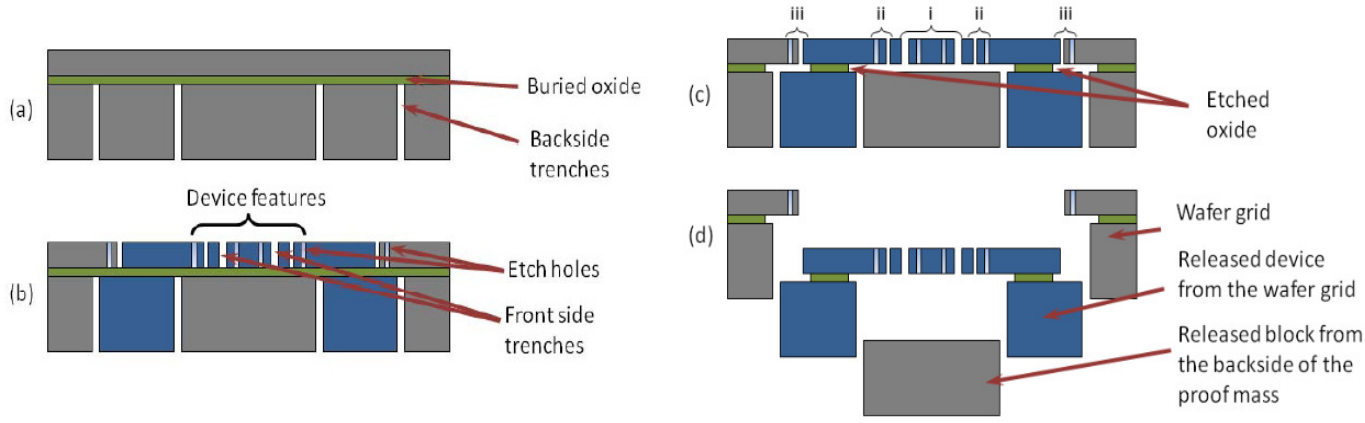

Figure 5-4 Removal process: (a) backside trenches etched using DRIE, (b) frontside trenches and features etched using DRIE, (c) release regions etched in HF VPE, (d) device separation (after Sari, Zeimpekis and Kraft, 2010, [95])

The devices presented have been designed to be fabricated using Silicon on Insulator (SOI). For this reason it was necessary to implement etch holes in the design to enable the oxide beneath the device layer to be etched. Back side and front side trenches are also incorporated into the design to allow for the complete release of the device from the wafer by etching and thus a dicing free process.

For this process, 6 inch double side polished SOI wafers are used. These wafers feature a 50±5µm silicon device layer. This is p-type boron doped silicon with a resistivity of 0.001-0.0015Ωcm. The buried oxide (BOX) layer is 5µm and sits on top of the 400µm thick silicon handle layer.

5.2 Process Flow

In the process described above, the back side trenches are patterned first in photoresist and etched followed by the patterning and etching of the front side features. Before the front side is inserted into the spinner to have a layer of photoresist deposited, the SOI wafer is attached to a silicon handle wafer to protect the wafer and deeply etched features of the back side. The SOI wafer and handle wafer are stuck together using a heat sensitive double sided tape. After the spinner stage, the wafer is soft baked and during this stage, the tape loses its adhesiveness and the handle wafer should easily disconnect from the SOI wafer. However, this is not always the case. A small force is often required to separate the wafers which can easily result in the breaking of the delicate SOI wafer. Clearly this is not an ideal situation and so for this work, a minor modification to the process in [95] is presented.

This process starts with the cleaning of the wafers in fuming nitric acid to remove organic contaminants. A 1µm layer of silicon dioxide ($Si0_2$) is deposited on the surface of the device layer using Plasma Enhanced Chemical vapour deposition (PECVD). This oxide layer will form a hard mask for the device features. A 6µm layer of AZ9260 photoresist is then deposited on to this oxide layer and is patterned using standard photolithography. The patterned oxide is then etched down to the silicon device layer using an Inductively Controlled Plasma (ICP) etch. The photoresist is then removed using an O_2 plasma etcher. This concludes the hard mask development for the front side features.

The next step is to pattern the back side of the SOI wafer. A 9µm layer of AZ9260 resist is deposited on the back of the wafer. This is then patterned and developed using photolithography. The structures are then defined by deep reactive ion etching (DRIE) up to the buried oxide layer. Again the back side photoresist is removed in O_2 plasma. The wafer is then reversed again and the front side is also etched to the buried oxide layer with DRIE. The wafer is very delicate at this stage as only the 5µm buried oxide is holding the device to the wafer.

The final step is the release of the devices using a solution containing 48% HF. A HF vapour phase etch is carried out to minimise the effect of stiction of device features, which is common when using a HF wet etch. However, as these SOI wafers have a thick 5µm BOX layer, the vapour etching time had to be split into segments in order to further prevent stiction. The oxide was etched in 4x20 minute intervals with 20 minute rest periods in between. This was to allow the HF to fully evaporate before re-starting the etch phase. Once the HF etch is complete, the devices are released in two stages; the mass of substrate layer beneath the suspended device is removed and then the actual devices are separated from the remaining wafer grid. This process is shown in figure 5-5 and the exact process flow can be found in appendix B of this thesis.

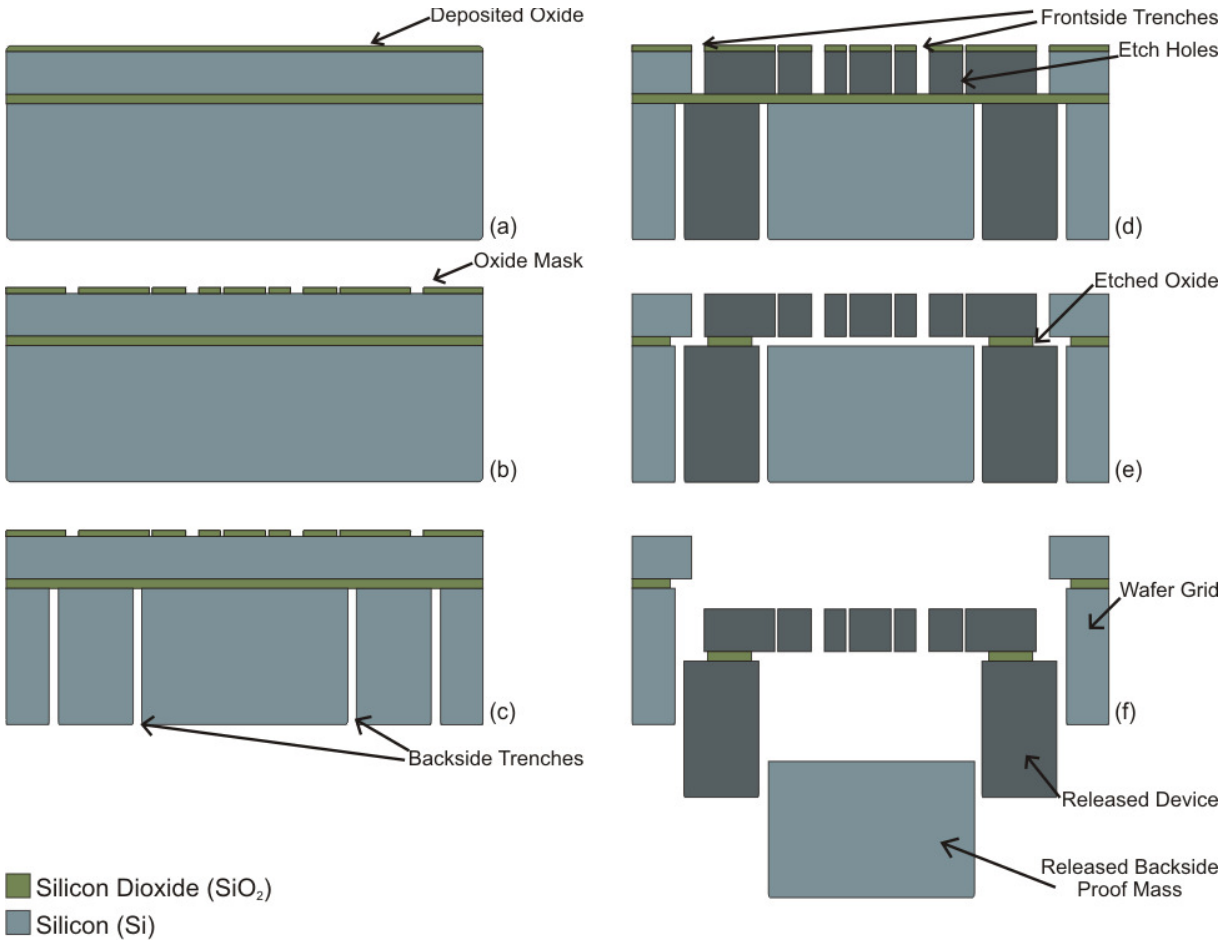

Figure 5-5 Removal process: (a) 1µm layer of silicon dioxide is deposited using PECVD, (b) top layer of silicon dioxide is patterned and etched to create front side hard mask, (c) back side trenches are patterned and defined using DRIE, (d) front side features are defined using DRIE, (e) buried oxide and hard mask layer etched in HF VPE, (d) device separation.

In order to prevent the devices from shorting if the electrodes make contact, a 400nm layer of oxide was deposited between the electrodes. Tetraethyl Orthosilicate (TEOS) oxide was chosen to be the deposited material as it benefits from more uniform step coverage than traditional silicon dioxide [97]. This would ensure a better distribution of the oxide on the sides of the electrodes. Depositing TEOS increases the capacitance level and multiplication factor of the device as shown in table 5-1. Clearly, a thicker oxide is more beneficial as it will result in less current leakage, however, in order to maintain some flexibility in the movement of the electrodes, a maximum oxide thickness of 400nm was set as the gap between the electrodes is initially 3µm.

Table 5-1 - Simulated effect of TEOS deposition on capacitance level and voltage multiplication factor.

TEOS (nm)	C_{MIN} (pF)	C_{MAX} (pF)	M
0	3.96	11.22	2.83
200	4.17	12.68	3.04
400	4.52	14.12	3.12

5.3 Results and Discussions

The fabrication work was split into two rounds; the original devices were first designed and fabricated followed by the design and fabrication of the modified devices in the second round. The original bi-stable and resonant devices were successfully fabricated and released. These released devices from this first batch of devices were evaluated under a single electron microscope (SEM). It was found that the side walls on the front side deviated by ≈1° from being perfectly vertical. This matches the side wall angle measured from test wafers where the fabrication process of [95] is followed i.e. no oxide mask is used for front side etching. The side wall angle of the back side is not so critical, as the features are larger, and deviates by ≈3°. Feature dimensions also were found to be closely matched to the ideal mask dimensions. For the comb fingers there was <0.5µm of over-etching from either side of the electrodes and, for the actuator and spring components, there was no obvious visible over etching, however, the SEM tool is subject to observation inaccuracies.

SEM images of the bi-stable and resonant devices are shown in figure 5-6 and figure 5-7 respectively. A close up image of the mechanical stopper element is shown in figure 5-8.

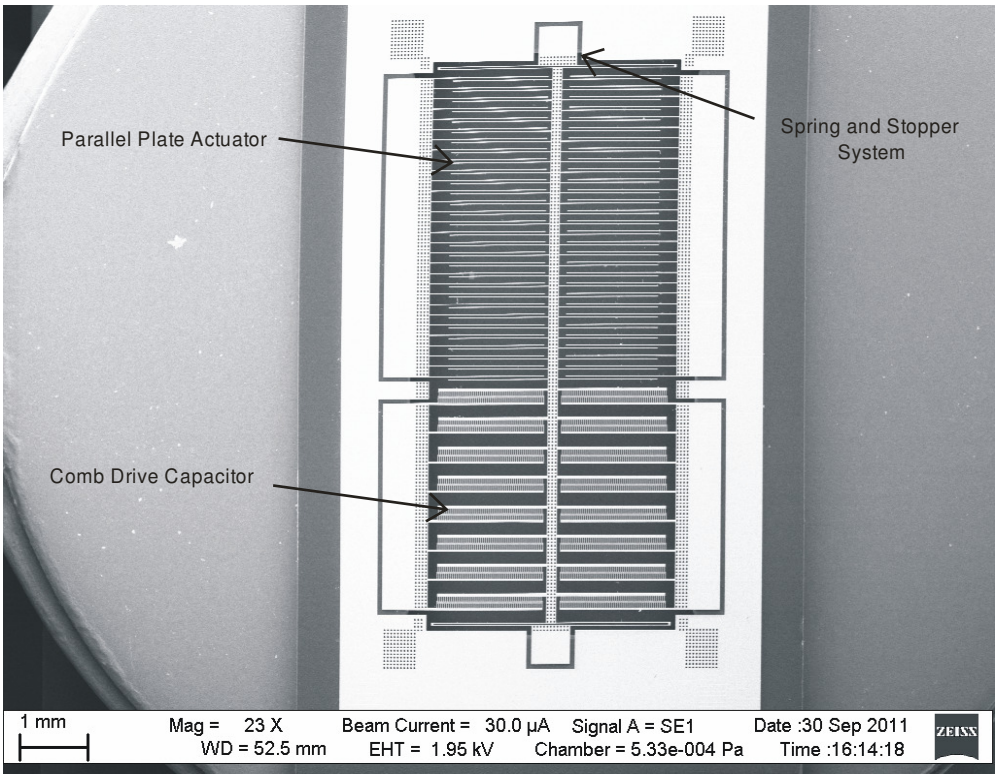

Figure 5-6 SEM image showing a complete front side view of a released bi-stable converter device.

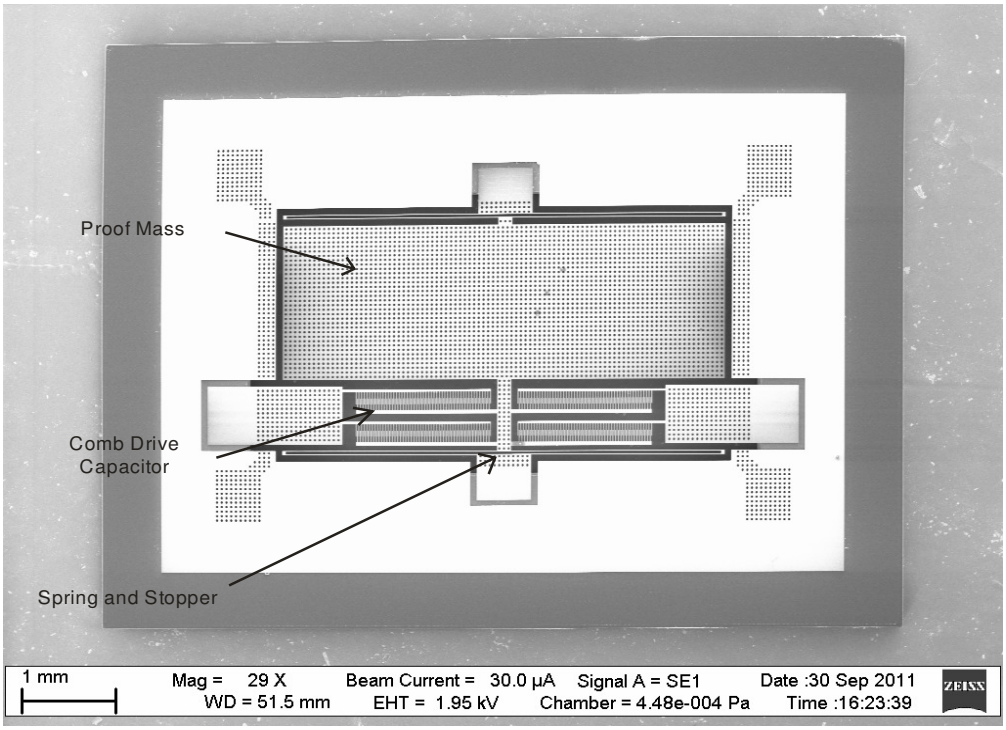

Figure 5-7 SEM image showing a complete front side view of a released resonant converter device.

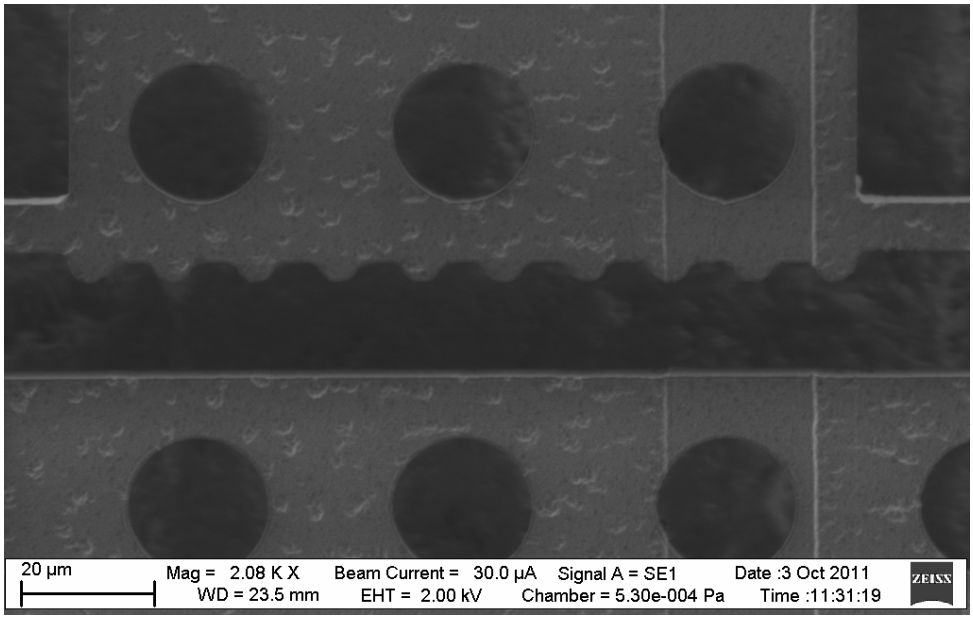

Figure 5-8 SEM close-up image of mechanical stopper element which inhibits the pull-in effect between the actuator electrodes. The small round bumps prevent stiction of the payload beam to the fixed anchored mass.

Camera images of the released resonant devices are shown in figure 5-9 and figure 5-10. The removed back side proof mass is also shown in this image.

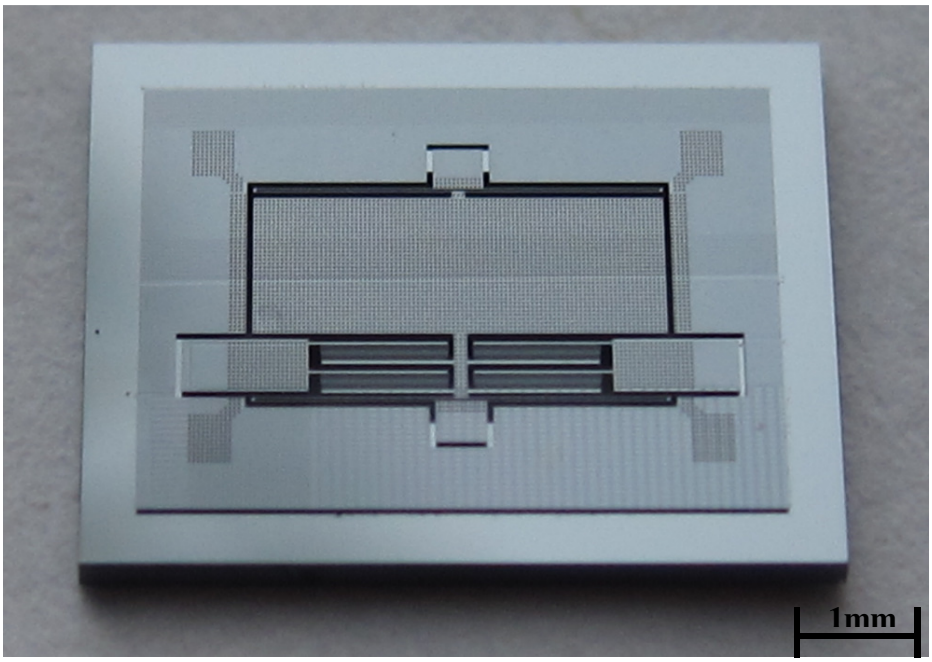

Figure 5-9 Front side camera image of released resonant device

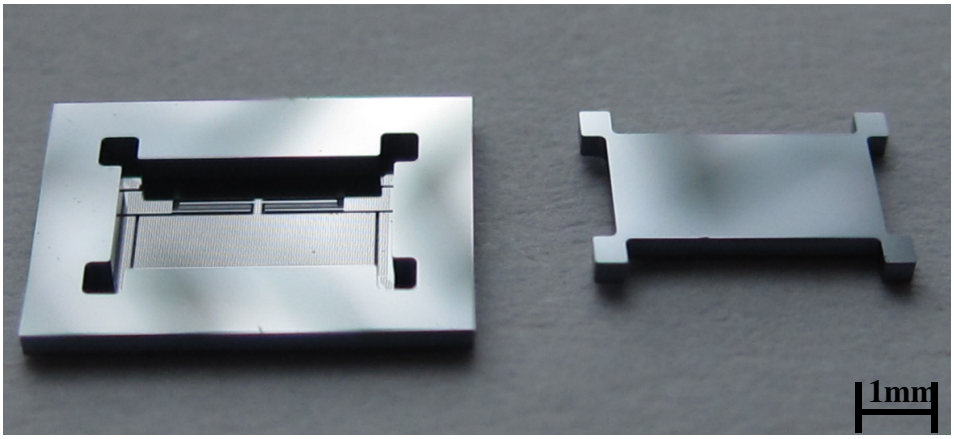

Figure 5-10 Back side camera image of released resonant device and released substrate block from underneath the suspended device.

Camera images of the released resonant devices are shown in figure 5-11 and figure 5-12.

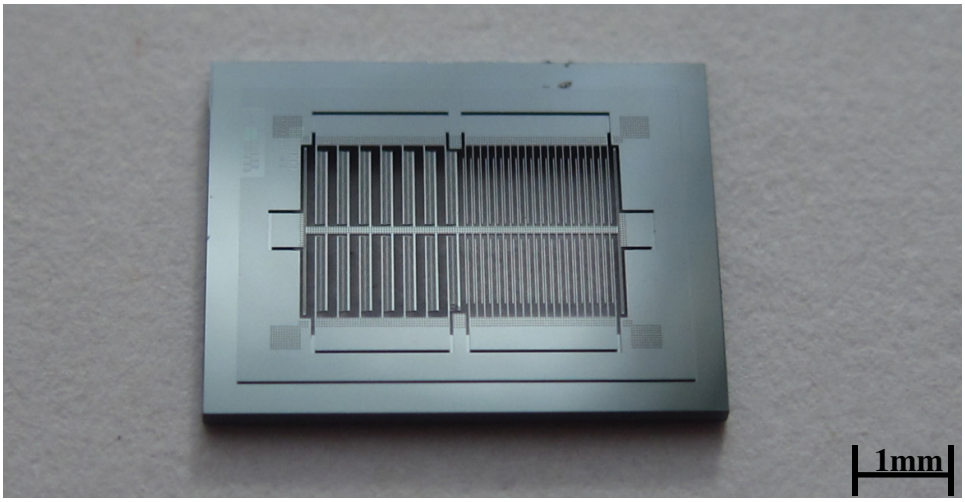

Figure 5-11 Front side camera image of released bi-stable device

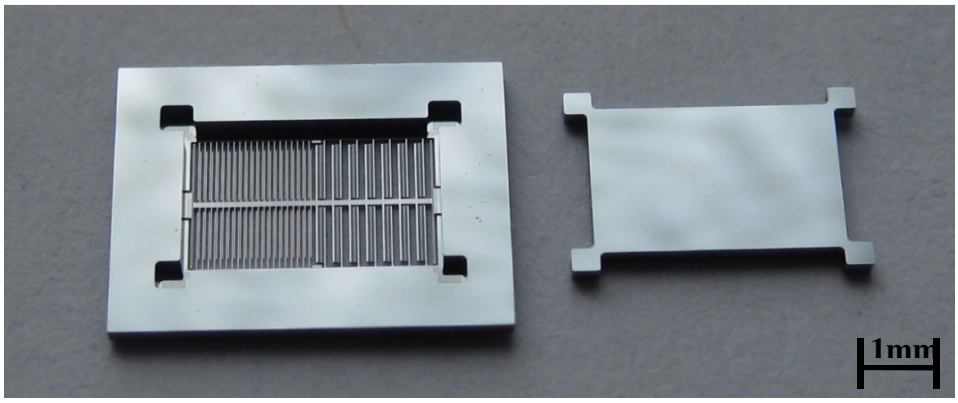

Figure 5-12 Back side camera image of released bi-stable device and released substrate block from underneath the suspended device.

When it came to fabricating the second round of modified devices, there was a fault with the DRIE tool at Southampton's Cleanroom facility. Alternative methods of etching included a KOH wet etch and an ICP RIE Bosch etch. The orientation of these wafers (100) was not suitable for the wet KOH etch as this would etch at a 45º into the wafer. Development of a Bosch process using the ICP was possible for small silicon thicknesses (<150µm). Beyond this thickness, the silicon etching stopped and the resist was etched instead.

Eventually, the wafers were etched using the DRIE tool at University College London (UCL). Unfortunately, these wafers returned under-etched. This was evident during the HF VPE release stage when, after extended periods of exposure to the HF vapour, the devices still did not release. As the wafer was under-etched, the vapour could not reach the buried oxide. There was no time left on this project for a complete re-fabrication given the time constraints associated with the installation of a new DRIE tool at Southampton. Some devices were "manually" released from the wafers by applying a force. In the case of the modified resonant device, as shown in figure 5-13, this resulted in structural imperfections in the features. It did, however, allow for the measurement of the bi-stable curved actuator devices shown in figure 5-14.

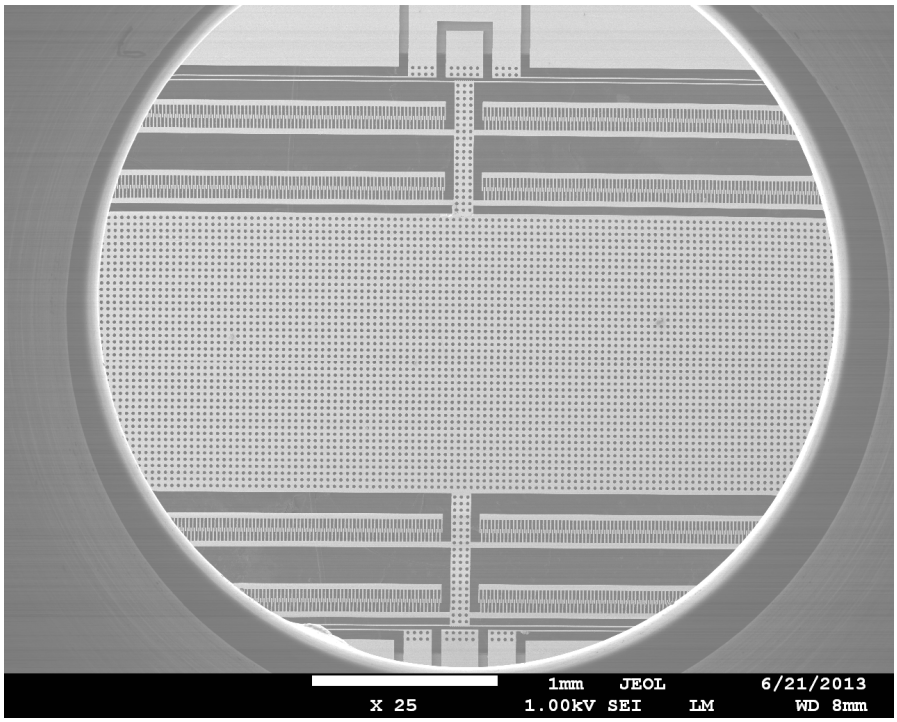

Figure 5-13 SEM image showing a front side view of the resonant converter device.

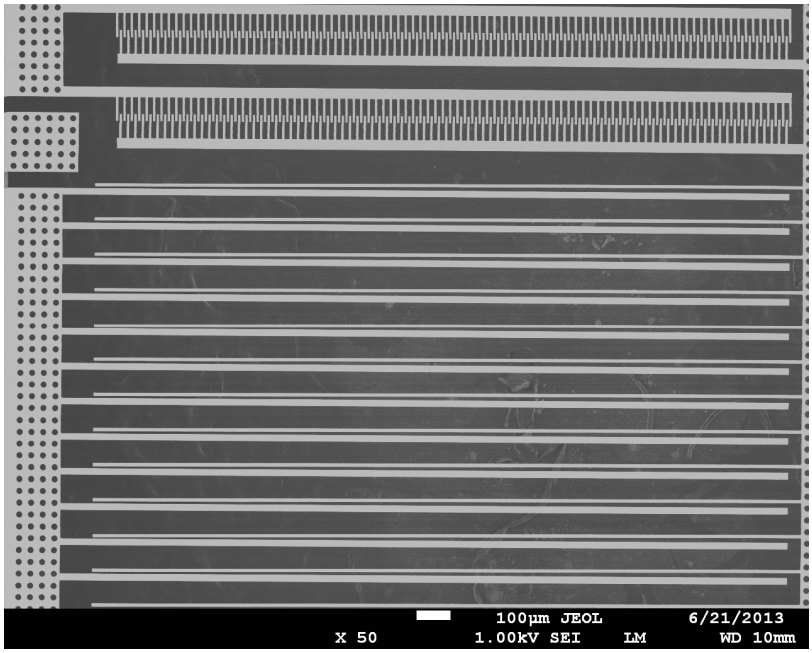

Figure 5-14 Close-up SEM image showing the modified bi-stable device with "curved" electrode actuator.

Once the individual devices have been released from the wafer a crystal bond is used to fix the device onto a 1x1cm^2 gold square of a 1.5x1.5cm^2 PCB package. The anchor, capacitor and actuator electrode segments are then wire-bonded to the electrode pads on the PCB. A plastic cover is placed over the device to prevent dust from landing on the die and header pins are soldered on to the PCB pads. This enables the devices to be integrated into an interface circuit. A plastic cap is placed on top of the device to prevent contamination from dust particles. This packaged device is shown in figure 5-15.

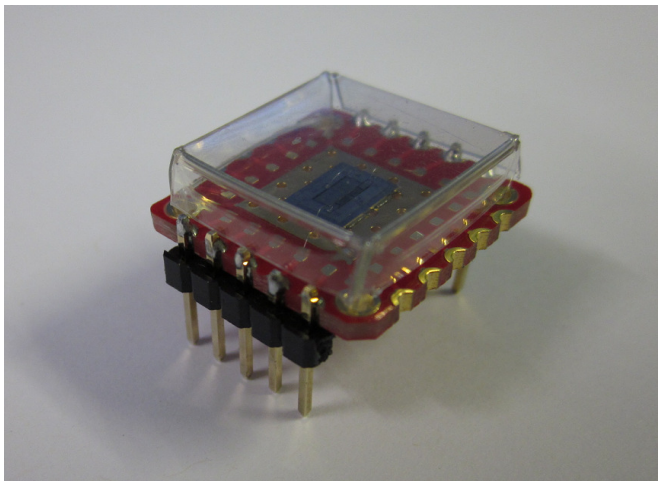

Figure 5-15 Camera image of packaged device. Chip is first wire bonded onto PCB; header pins are then soldered to contact pads on the sides.

5.4 Summary

The bi-stable and resonant MEMS voltage converters were successfully fabricated using an SOI process for high aspect ratios. The modified versions of these converters were also fabricated, but the yield was too low to deem it a success. This was due to the lack of access to a functional DRIE tool at Southampton in the later stages of this project. The fabrication process and results were discussed in this chapter. In brief, the front side and back side of the SOI wafer follow a similar process flow, with the addition of an oxide mask on the front side to protect the smaller features.

Trenches and etch holes were incorporated into the mask patterns to allow for a dicing-free release of the device. Both sides of the wafer were patterned using a standard photolithography process and etched up to the BOX layer using DRIE. The devices were released from the wafer after a HF etch of the BOX layer. TEOS oxide is deposited on the sidewall of the capacitor and actuator electrode to prevent shorting. This will also theoretically increase the capacitance of the devices. The released devices are then bonded to a PCB die using crystal bond and the electrical connections are made with a wire bonder.

In general, the results are positive and there is little need for further optimisation of this process for the fabrication of devices in this work. The side wall angles are close to being perfectly vertical and there was a 100% yield in the first round of devices. There is also far less risk of breaking a wafer during the DRIE stage with the introduction of the oxide mask step. The next section of this thesis details the evaluation of these fabricated devices.

Chapter 6 Experimental Evaluation of MEMS Voltage Converters

6.1 Device Characterisation

Once the devices have been fabricated, it is necessary to evaluate their performance and compare it with the theoretical models developed earlier in this thesis. A certain amount of variation is expected in the measured results due to fabrication tolerances. This chapter will start with the physical characterisation of the bi-stable converter devices i.e. measuring resonant frequency, topology etc. These devices will then be integrated with the control circuit designed in chapter 4, and output voltage and electrical efficiency results will be measured.

6.1.1 Topography

The characterisation of the converter devices is carried out using a Polytech MSA400 measurement system. This is an optical system capable of measuring in-plane and out-of-plane motion, and taking topology measurements without the need for an interface circuit. The system consists of a laser vibrometer, stroboscopic camera and a white light interferometry module.

The topology of the devices was measured, and thus the effective fabrication verified, using the white light interferometry method. This measures, pixel by pixel, the intensity of the light reflected from the device back to the camera and generates an accurate profile of the device based on this measurement. The output of this measurement for the bi-stable and resonant device is shown in figure 6-1 and figure 6-2 respectively.

For the bi-stable device, the result in figure 6-1 shows that the proof mass sits ≈68nm beneath the surface of the fixed anchors. This is indicated by Δz between points 1 and 2 in the diagram. This tilting is not critical as it has little effect on the capacitance and over all operation of the device.

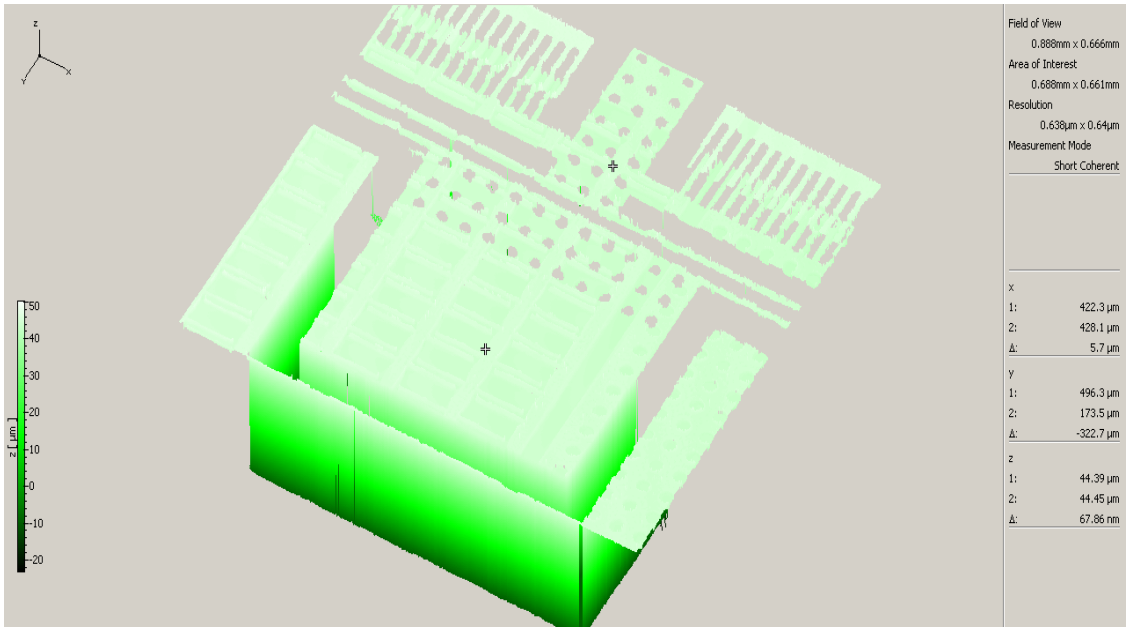

Figure 6-1 Topology of anchor and suspended central beam of bi-stable converter device using white light interferometry.

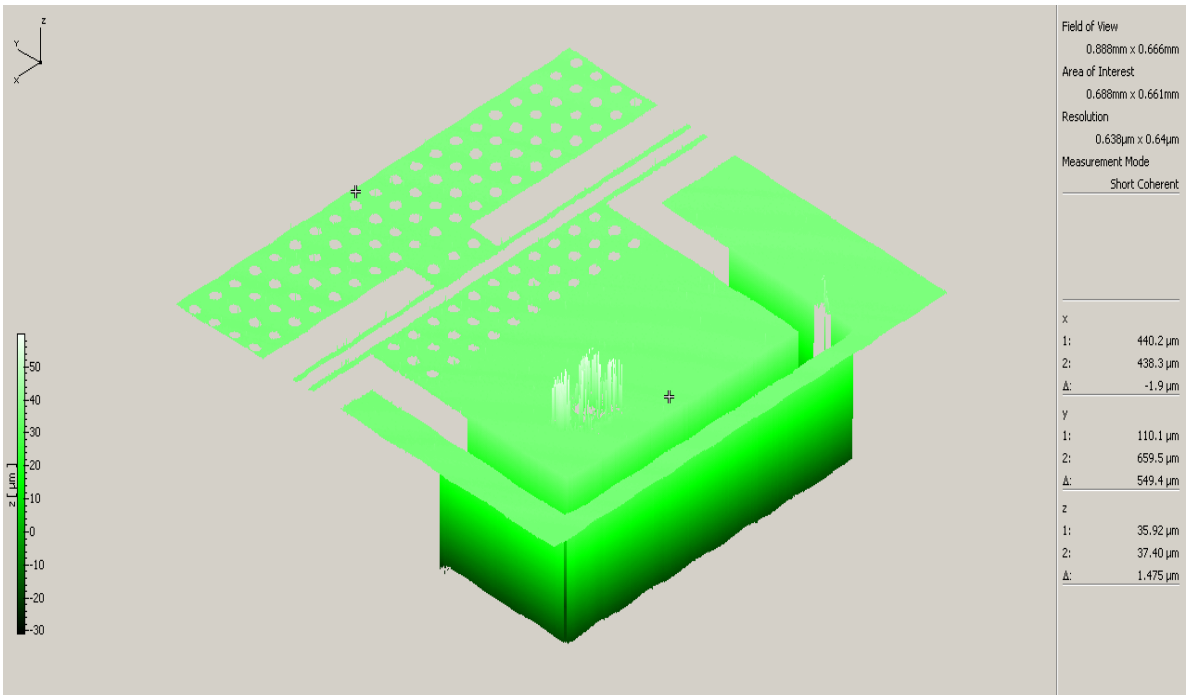

Figure 6-2 Topology of anchor and suspended proof mass of resonant converter device using white light interferometry.

For the bi-stable device, the result in figure 6-2 shows that the proof mass sits ≈1.5µm beneath the surface of the fixed anchors. This tilting will have some minor effect on the capacitance and over all operation of the device. The reason for this increase in tilting is due to the lower value of spring constant and the large proof mass.

6.1.2 Resonant Frequency

The in-plane motion was then characterised using the MSA 400's stroboscopic camera. This camera captures a predefined number of images of the device under test. These images are then correlated and the displacement of the device under various frequencies can be extracted.

It is necessary to apply an AC excitation voltage to the devices to simulate a mechanical vibration. It is not possible to directly apply a physical vibration to the device as this excitation cannot be obtained at the same reference frame as the camera. An issue exists, however, in applying an AC voltage to excite the device; the electrostatic forces of the comb drive capacitor and parallel plate actuator are dependent on the input voltage squared ($V_{IN}{}^2$).

$$F_{EL} \propto {V_{IN}}^2 \tag{6-1}$$

$$V_{IN} = (sin\omega t)^2 = \frac{1 - cos2\omega t}{2} \tag{6-2}$$

The measured frequency of oscillation has doubled, in relation to the frequency of the input signal, due to the presence of the cos2ωt component. To overcome this frequency doubling effect is necessary to apply a DC bias voltage to the capacitor and actuator electrodes. This will eliminate the AC voltage affecting the electrostatic force. If a positive DC bias is applied to the capacitor electrodes, then an equal but negative value must be applied to the actuator. The total electrostatic force of the system is the difference between the electrostatic force generated by the actuator and the capacitor.

$$F_{EL} \propto V_{ACTUATOR}^2 - V_{CAPACITOR}^2 \tag{6-3}$$

$$F_{EL} \propto (V_{AC} + V_{DC})^2 - (V_{AC} - V_{DC})^2 \tag{6-4}$$

$$F_{EL} \propto 4V_{DC} \tag{6-5}$$

In the case of the bi-stable device, this is uncomplicated to set up; a positive and negative DC bias is applied to the actuator and capacitor electrodes and the AC excitation signal is applied to the central moveable beam. The resonant of frequency of the bi-stable device is shown in the magnitude and phase plot in figure 6-3.

Another issue exists with regards to using the stroboscope camera and electrostatic excitation to measure resonant frequency; noise. There are many possible source of noise that can affect the accuracy of the measurement e.g. table vibration, camera magnification, contrast level, resolution etc. As such, it is necessary to excite the system using a large force/amplitude level to reduce the impact of the noise. Large electrostatic forces in mechanical systems with

parallel plate translational capacitors result in electrostatic spring softening [98]. Therefore, the measured levels of resonant frequency are lower than expected. The measured resonant frequency for the bi-stable device is ≈480Hz.

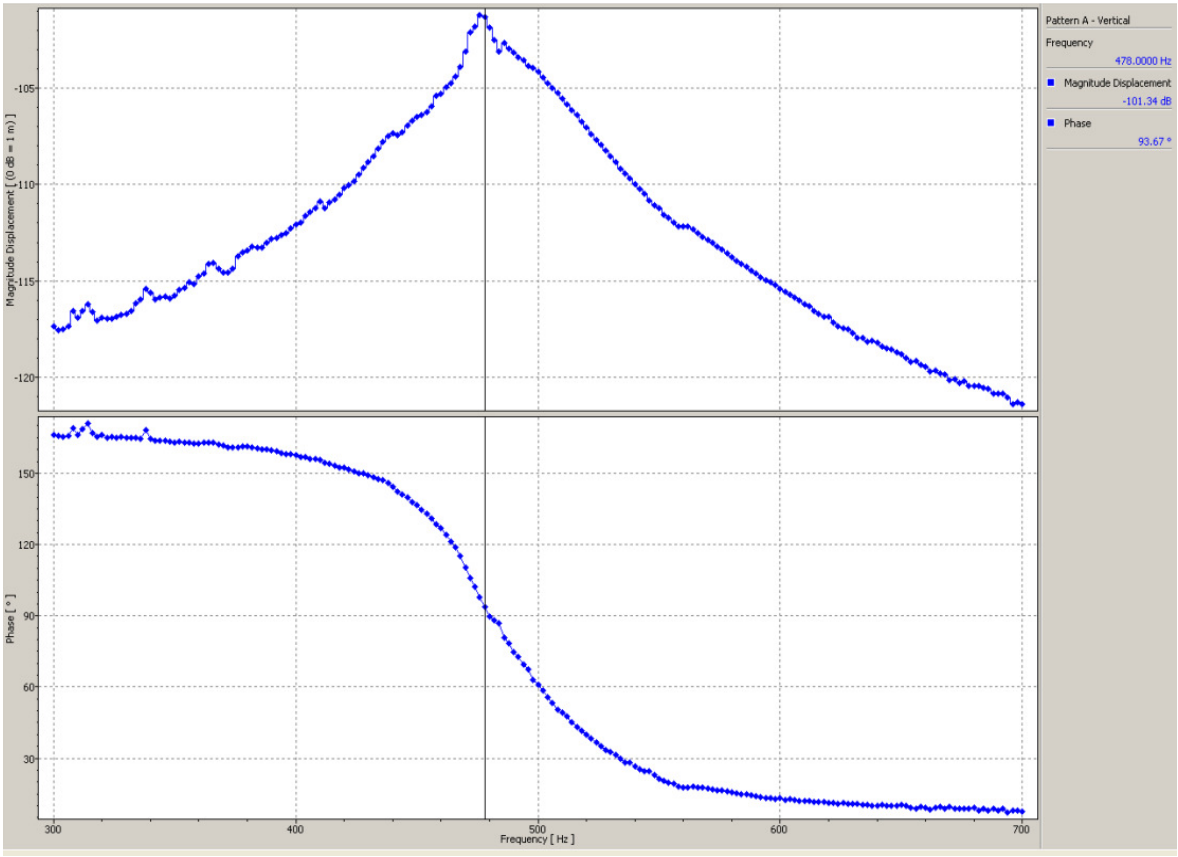

Figure 6-3 Magnitude and phase plot for bi-stable device. Resonant frequency is ≈480Hz.

When measuring the resonant frequency of the resonant device, as it does not feature any actuation electrodes, it is not possible to apply a DC bias to prevent the "doubling" of the input frequency. This was solved by manually extracting the output data points for each frequency in a sweep range. These data points were exported as an Excel file and processed in Matlab to produce a magnitude and phase plot, this is shown in figure 6-4. The Matlab file can be found in Appendix A of this thesis. The code generates the input sine wave signal, at each frequency point, based on the frequency and displacement data saved from the MSA400. From the input signal, the magnitude and phase plot can be constructed using the following formulae

$$\Delta\theta = (t_{MAX\_OUT} - t_{MAX\_IN}).f.360 \quad 6\text{-}6$$

$$Magnitude = 20\log_{10}(A_{MAX\_OUT}) \quad 6\text{-}7$$

Where t_{MAX_OUT} is the time at which the output signal is at its maximum amplitude, t_{MAX_IN} is the time at which the input signal is at its maximum amplitude, f is the frequency of both signals and A_{MAX_OUT} is the maximum amplitude of the output signal.

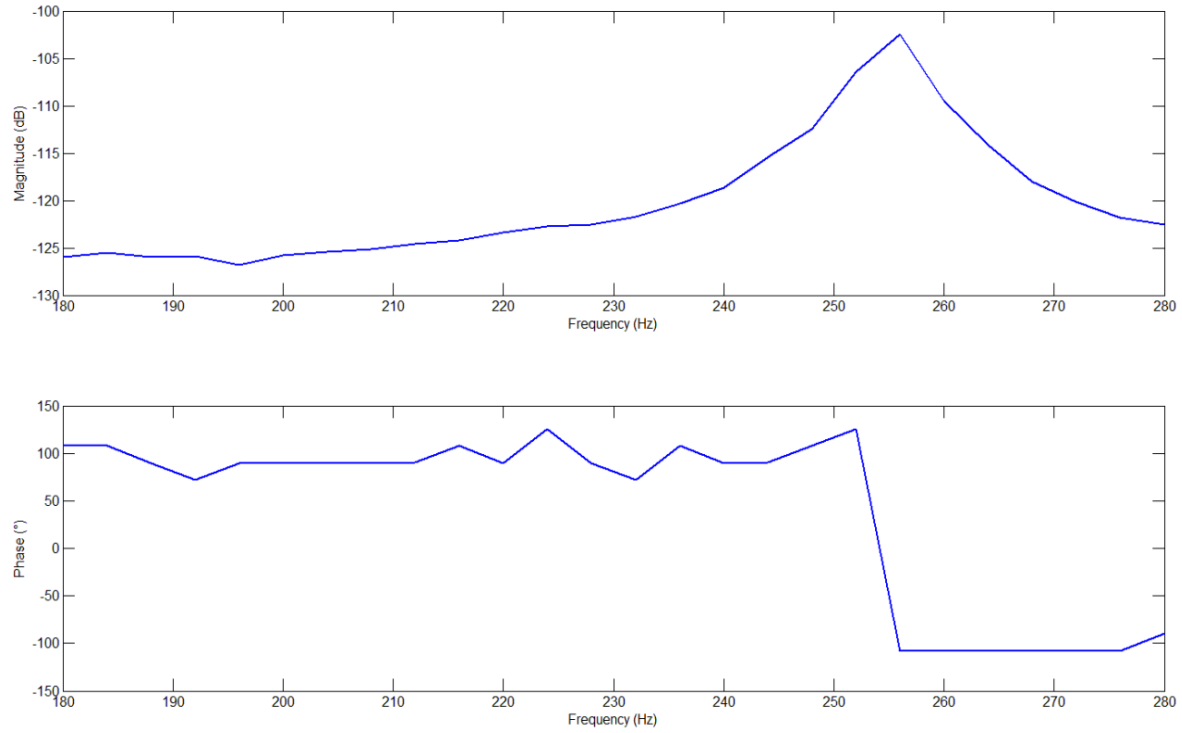

Figure 6-4 Magnitude and Phase plot for resonant device extracted data points using Matlab. Resonant frequency is ≈256Hz.

The measured frequency is found to be ≈256Hz. The FEM simulated value for this frequency was 294Hz. This is a variation of 13%.

6.1.3 CV Analysis

Capacitance measurements were made using Agilent's 4279A CV meter programmed for a DC sweep. This equipment operates using a charge feedback technique to measure the quasi-static capacitance over a range of voltages. It was not possible to repel the electrodes to measure the minimum capacitance level; this had to be done manually by pulling apart the electrodes with a probe. Therefore, the measurement results obtained from the 4279A meter, as shown in figure 6-5, only indicate the capacitance levels from the rest position to the maximum capacitance position.

For a device with no TEOS deposited on its electrodes, the maximum and minimum capacitance levels were found to be 10.2 pF and 4.8 pF respectively, resulting in a multiplication factor of M=2.125. With 400 nm of TEOS, the maximum and minimum

capacitance levels were found to be 15 pF and 5.1 pF resulting in a multiplication factor of M=2.94. The capacitance level is not symmetric about the rest point as the influence of fringing capacitances increase with decreasing electrode overlap.

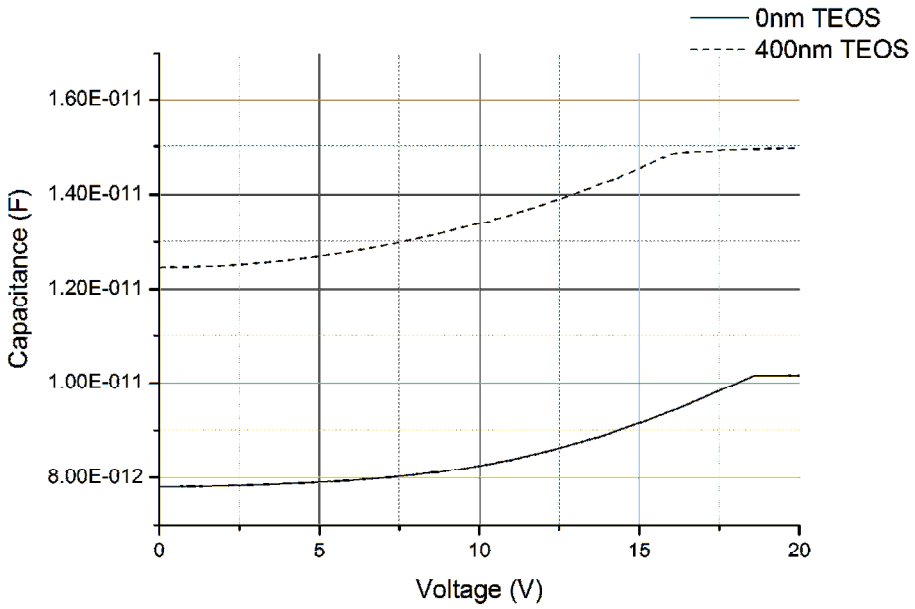

Figure 6-5 Measured C–V plot of bi-stable device from rest position to g_{MIN} (C_{MAX}), (solid) with no TEOS oxide, (dashed) with 400 nm of TEOS oxide deposited on the electrodes.

There is a difference of ≈2pF between the simulated and measured values for C_{MAX}. This can be the result of a number of factors including inaccuracy in the measurement. Other factors that may influence the measurement are related to the actual features of the device. It can be seen in figure 6-6, that despite the designed overlap gap between capacitor electrodes of 21µm, the fabricated device features a gap of 22.52µm. These small variations in the fabrication will result in differences between the ideal simulated device and the real measured device.

In addition to the parasitic capacitance of the capacitors fringing fields, another parasitic coupling capacitance was found between the fixed actuator and capacitor electrodes as indicated in figure 3-13. This capacitance, which was measured as 3.2 pF, creates a connection between the actuator and capacitor. If a voltage is applied to the actuator, rather than pull apart the capacitor electrodes, it will charge the capacitor if the capacitor is not grounded.This will impact the output voltage of the interface circuit and produce inaccurate results. To rectify this issue, when a voltage is supplied to either capacitor or actuator, the

other must be grounded in order to discharge the parasitic coupling capacitance. Therefore, the actuator and capacitor must be switched on at non-overlapping intervals.

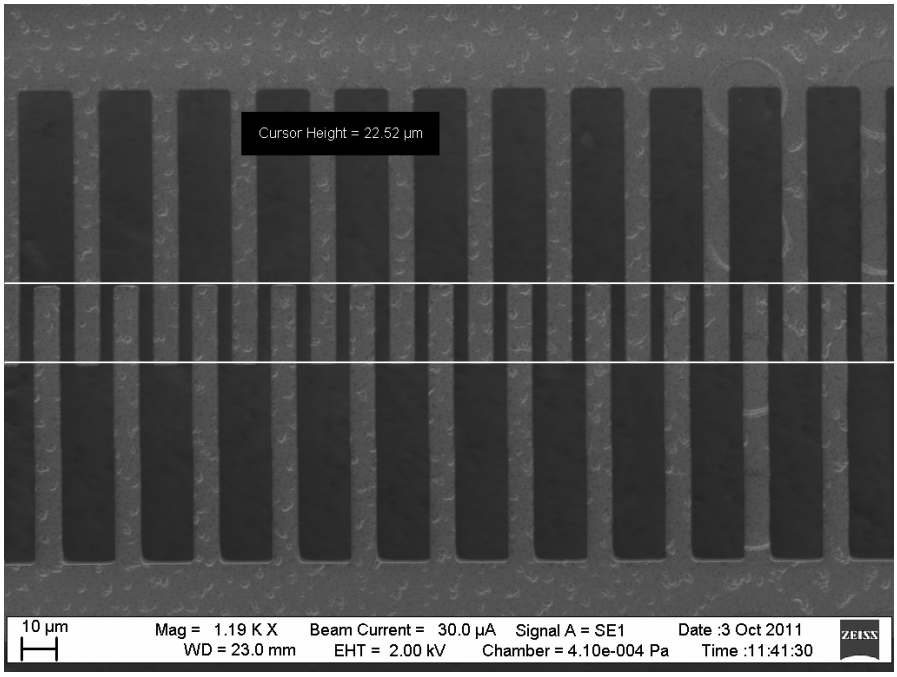

Figure 6-6 SEM close-up image of comb capacitor fingers of the bi-stable MEMS device. The measured overlap gap at rest is 22.52µm.

The same method of capacitance measurement was applied to the resonant devices. The results of this capacitance-voltage sweep are shown in figure 6-7. Again, the measurement results obtained only indicate the capacitance levels from the rest position to the maximum capacitance position. The minimum capacitance level was measured manually using a probe. The maximum and minimum capacitance levels were found to be 3pF and 1.3pF respectively, resulting in a multiplication factor of M= 2.3. The capacitance level is not symmetric about the rest point as the influence of fringing capacitances increase with decreasing electrode overlap.

It can be seen in figure 6-8, that the overlap gap at rest between capacitor electrodes is 32.35µm which is a ≈2µm deviation from the mask design. This is an example of a factor which is a potential source of error between measured and simulated results.

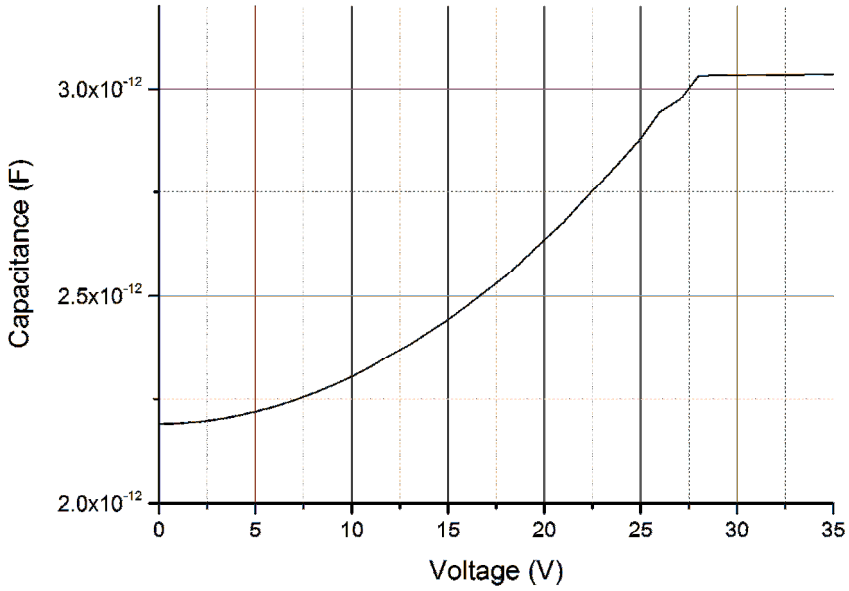

Figure 6-7 Measured C–V plot of resonant device from rest position to g_{min} (C_{max}) with no TEOS oxide.

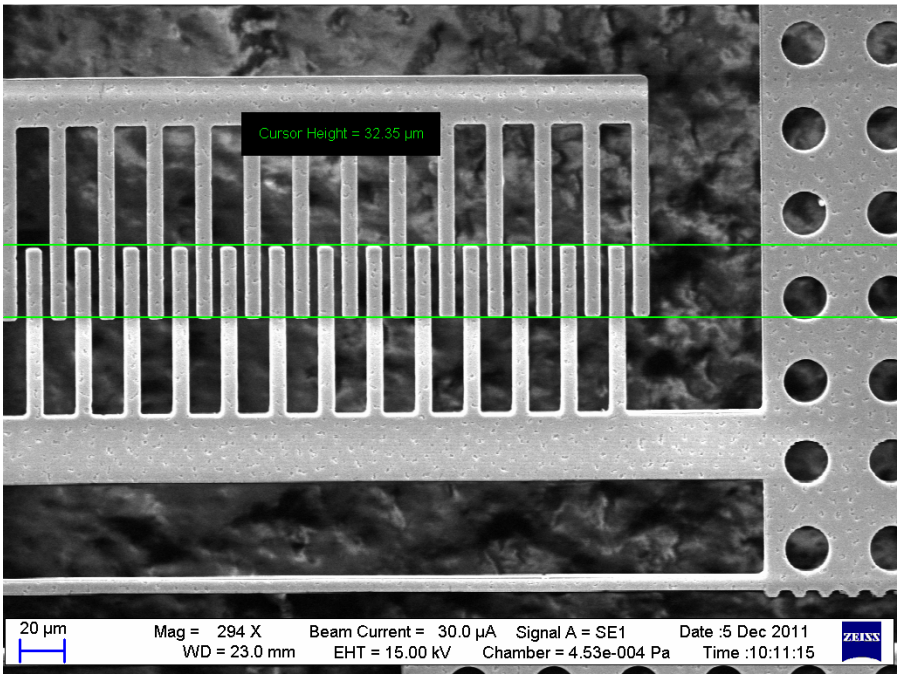

Figure 6-8 SEM image of capacitor electrodes in resonant MEMS converter device. At rest electrode overlap is shown to be 32.35µm.

6.1.4 Curved Electrode Pull-in

Using the camera on the MSA400, the electrode pull-in effect can be monitored. This is not so critical for the standard bi-stable devices which feature a mechanical stopper element in

the spring to prevent electrodes from pulling in (and therefore shorting). However, for the modified bi-stable device, the operation of the actuator is based on the curved electrodes pulling in and creating a ripple pull-in effect. These curved electrodes have a layer of TEOS oxide deposited to prevent shorting on contact.

To monitor the pull-in, an external voltage is applied to the electrodes from a function generator. This voltage is manually swept from 0-24V in steps of 1V and the electrode displacement is monitored. This was repeated on samples with 150nm and 400nm of TEOS oxide deposited between electrodes i.e. reducing the effective gap by 300nm and 800nm. The ripple pull-in effect does not occur in either sample. In both cases, pull in first occurs at the small gap end of the beams. As the voltage is increased, the large gap end of the beams then pulls-in. This is illustrated in the figures below. The system is shown at rest in figure 6-9. The voltage across the electrodes is then increased to the point where pull-in occurs at the tip of the electrodes. This takes place at 10V and is shown in figure 6-10. The voltage is increased to observe pull-in occurring at the opposite end of the electrodes. The voltage required for pull-in at this end is 17V and is shown in figure 6-11.

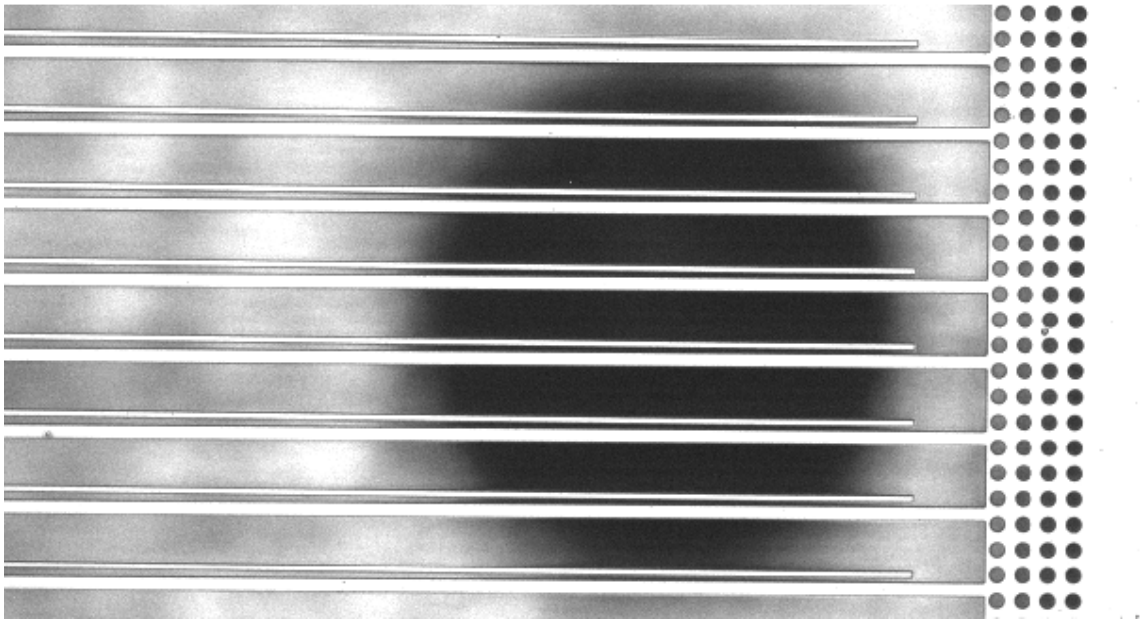

Figure 6-9 Modified bi-stable device's curved electrode actuator at rest with 150nm TEOS deposited on electrodes.

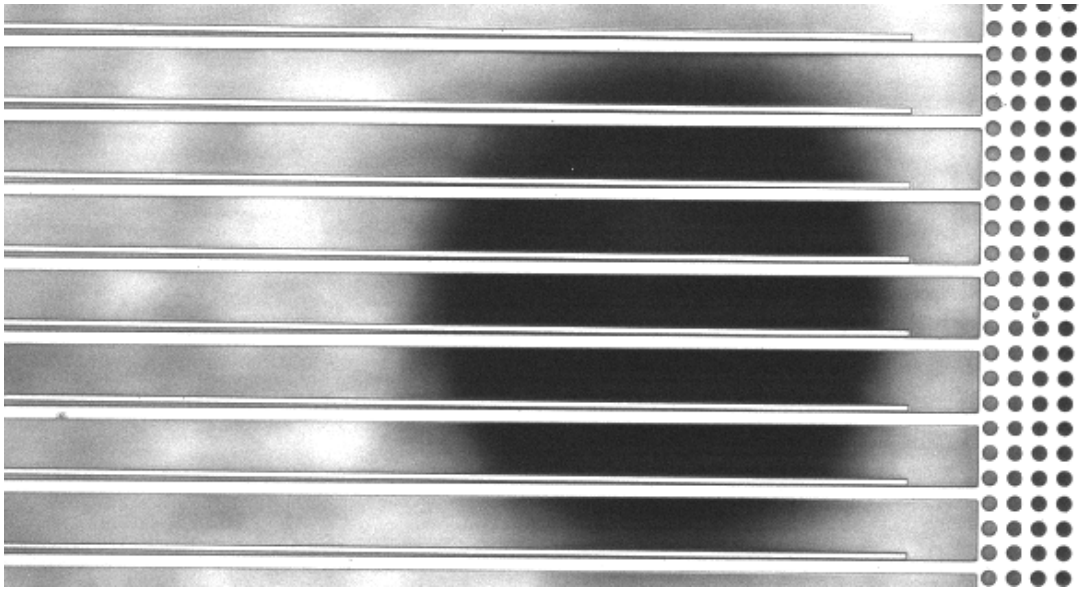

Figure 6-10 Modified bi-stable curved electrode actuator. Pull in at the tip occurs when 10V is applied. The remained of the electrode does not pull in.

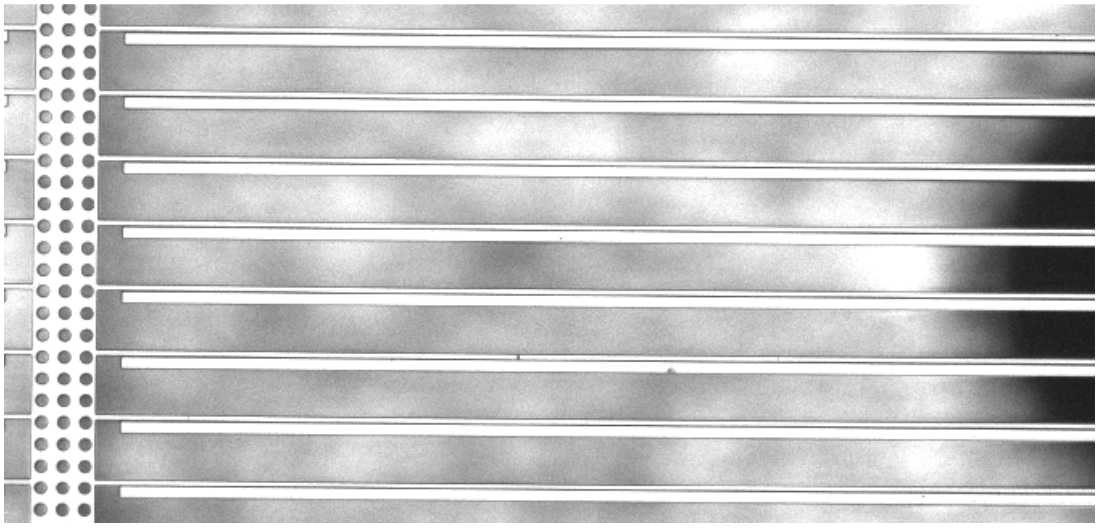

Figure 6-11 Modified bi-stable curved eelectrode actuator. Pull in at the clamped end occurs when 17V is applied.

These images show that pull in occurs in two stages rather than one continuous zipping pull-in action as desired. This is a result of the design of the beams. Steps can be taken in future design iterations to reduce the stiffness of the structure to encourage the zipping pull-in. For example, the spring constant of the double crap leg spring can be reduced or the length of the electrodes can be increased beyond 2mm to spread the separation step height per unit length and to generate more electrostatic force.

6.2 Bi-stable Interface Circuit Measurements

For testing the bi-stable device, the circuit in figure 3-27 was constructed. The effective load resistance from the oscilloscope probe is 100 MΩ. The load capacitor is 100 pF and 1N4148 diodes are used. The non-overlapping actuator and capacitor voltages are shown in figure 6-12.

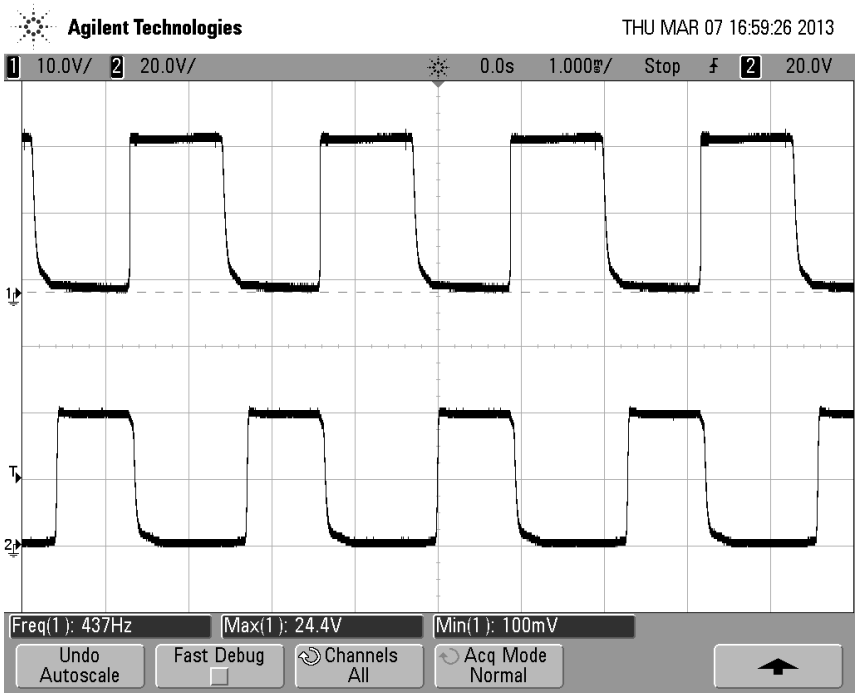

Figure 6-12 Non-overlapping capacitor and actuator voltages.

It was not possible to measure the output voltage of the modified resonant device, as these devices did not fabricate successfully. An attempt to measure the output voltage from the original resonant device was made, however, as expected from simulations; this did not successfully multiply the input voltage by any factor. The output voltage was simply a mirror of the input.

The set up for this experiment was as follows; the variable capacitor was mounted on a Labworks Inc. vibration shaker table. A Kistler piezoelectric reference accelerometer was also mounted to the shaker table. The shaker table was connected to an amplifier and controlled using Labworks software on a PC. The reference accelerometer provides a feedback signal for the software. This variable capacitor, which has been wirebonded to a chip carrier, had long thin wire-wrap wire connected to its capacitor and ground pins. The carrier was then recessed into the shaker table using wax. The other ends of the long wire

were connected to a test circuit. This was constructed on a PCB board and consisted of two Schottky diodes, a load capacitor and a terminal for the input sinusoidal voltage (generated from a function generator).

6.2.1 Output Voltage

The output voltage for this arrangement is shown in figure 6-13. This output response closely resembles the simulated output of 37.5V in figure 3-24. The peak voltage of this output is 26.34V.

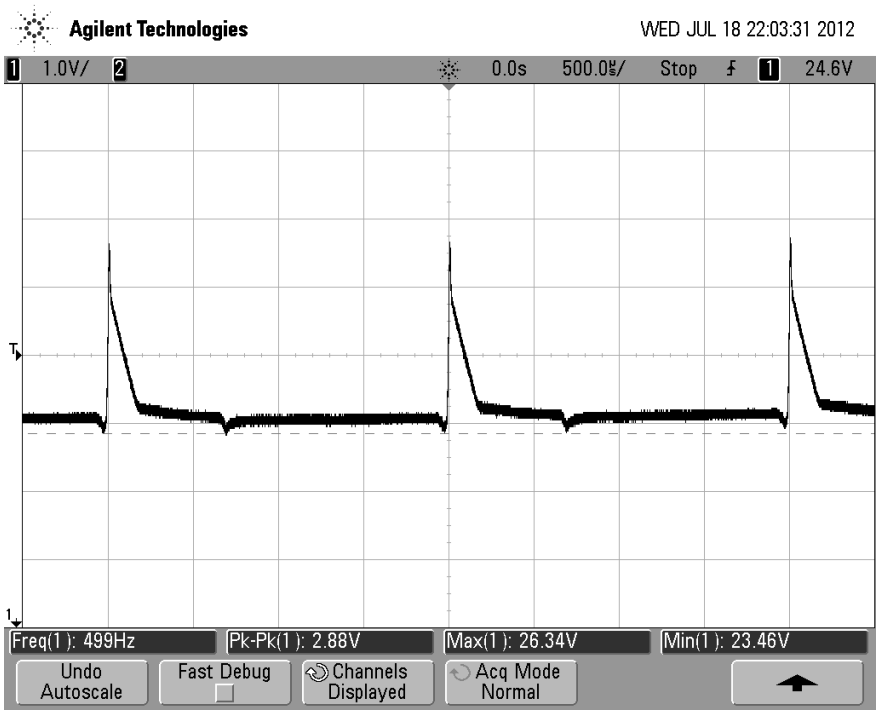

Figure 6-13 Measured output voltage of bi-stable device with 100MΩ oscilloscope probe connected to load capacitor.

By connecting multiple MEMS variable capacitor devices in parallel, the output voltage should increase as predicted by the simulated results shown previously in figure 3-25. By cascading four MEMS devices in parallel, the output voltage shown in figure 6-14 is obtained.

This result took ≈100ms to reach this steady state. This differs to the ≈10ms steady state time shown in simulations as the oscillator circuitry takes some time to settle into a 24V square wave. An example illustrating this is shown in figure 6-15. The voltage levels in this figure are not to be considered as it was simply an experiment to measure the timing delays. It can be seen that it takes ≈200ms for the lower voltage square wave signal to settle. This is the capacitor control voltage. The larger 12V signal is the rippling output voltage.

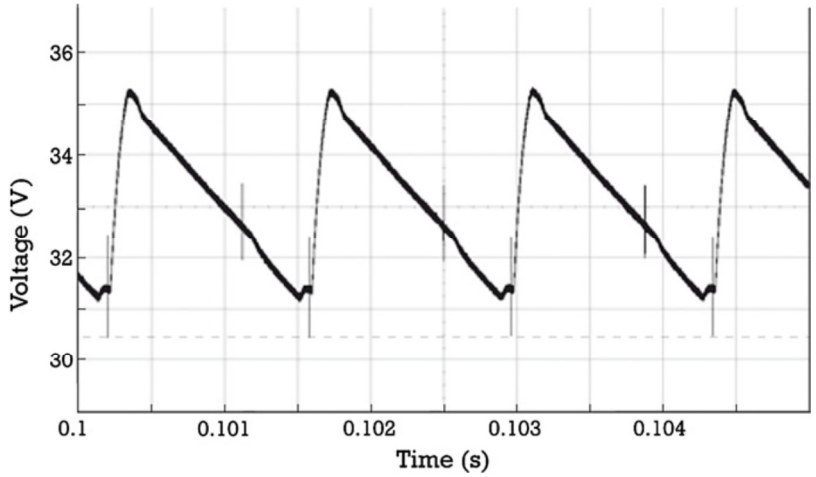

Figure 6-14 Steady state output voltage of bi-stable converter circuit. Maximum voltage level is 35.4V.

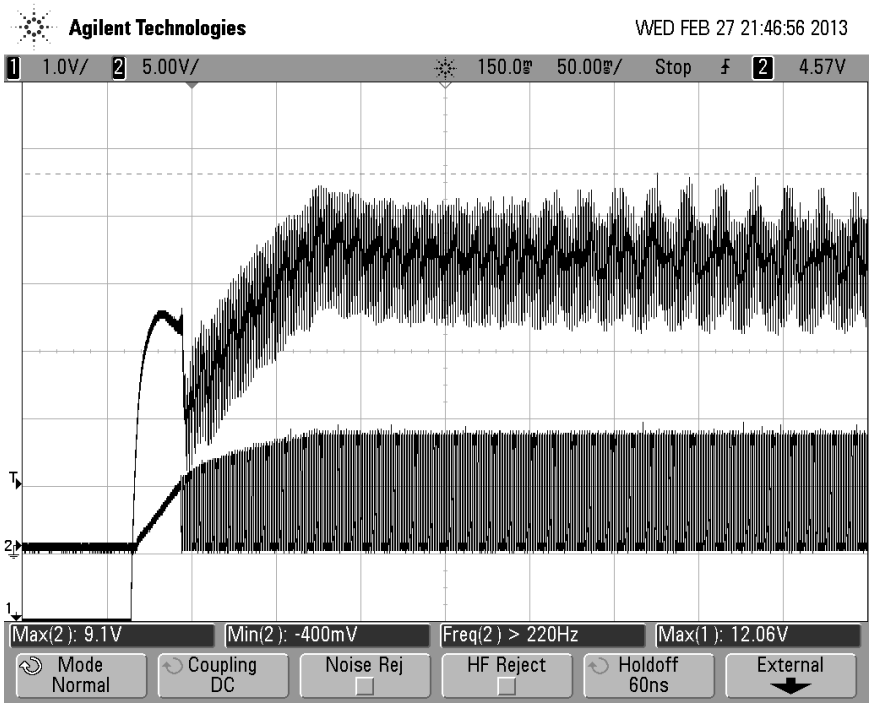

Figure 6-15 Steady state output voltage of bi-stable converter circuit. Square wave capacitor/actuator signal settles after ≈200ms.

The key result in in figure 6 14 matches the simulated result of 36 V, shown in figure 3-26, reasonably well. While this measurement was not repeated for a greater number of devices in parallel, based on this result, it can be assumed that the output would closely follow the simulated output of figure 3-25.

This measurement of output voltage is limited by the load resistance (100MΩ) of the measurement equipment. Should this load resistance increase beyond this level, the output

voltage would increase as simulated in figure 3-21. To prove this, a high impedance path was placed in series with the measurement probe using an op-amp unity gain buffer with a low input bias current. This experiment would test the multiplication capability of a single MEMS capacitor device using a high impedance load. The output voltage for this arrangement is shown in figure 6-16. The op-amp selected for this experiment was the AD8610 as it features an input bias current of 10pA. However, the maximum supply voltage is 40V so the output voltage will be limited at this level. Attempts were made to source an op-amp with a higher supply voltage; however, these were not successful given the input bias current restraint. The 40V supply required to power the op-amp device was provided from an external power supply unit.

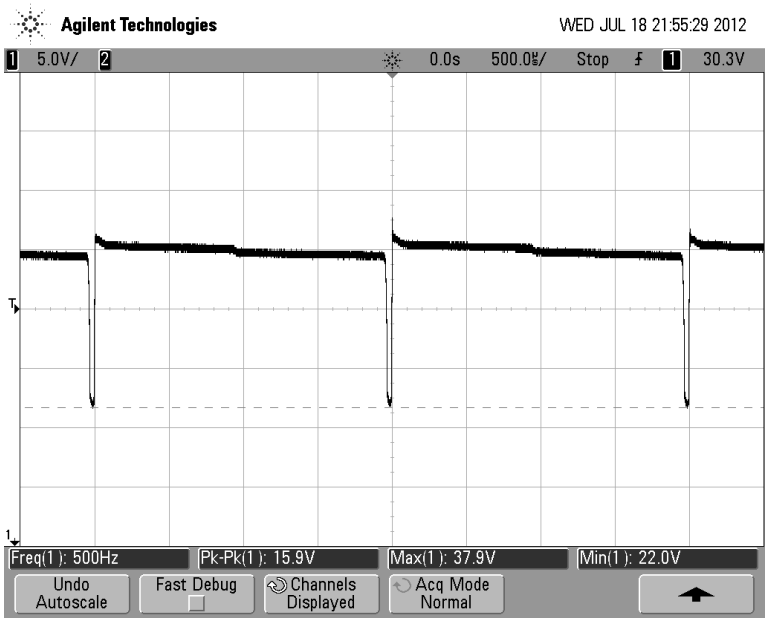

Figure 6-16 Steady state output voltage of bi-stable converter circuit featuring a unity gain op-amp chip to create a high impedance load. The maximum voltage level is 38V.

Unlike the output voltage shown in figure 6-14, the result shown in the figure above is the output voltage for a single MEMS capacitor device. This result proves that with a higher impedance load, a greater output voltage can be attained. Again, the output is limited by the voltage supply limits of the op-amp.

6.2.2 Electrical Efficiency

A Digital Multi Meter (DMM) was used to measure the instantaneous current at the input and output of the control circuit. The voltage at the input and output of the circuit was found to be 24V and 35.4V respectively. The measured current values are shown in table 6-1.

Table 6-1 – Efficiency measurement for bi-stable device

R_L	I_{IN}	I_{OUT}	η
100MΩ	2mA	300nA	0.022%

This result matches the theoretical efficiency found in figure 3-21. By increasing the load resistor to 1GΩ, the output current increased to 3μA, however, it was not possible to measure the output voltage at this high resistance level, therefore an accurate value of efficiency could not be extracted.

6.3 Summary

The evaluation results prove that the fabricated devices exhibit characteristics which are close in keeping with those determined through simulation. A comparison table for these two sets of results can be seen in table 6-2 and

table **6-3** below.

Table 6-2 – Capacitance and resonant frequency measurements and calulations for resonant device

$C_{calculated}$	$C_{measured}$	$f_{measured}$	$f_{calculated}$
Min = 1.3pF	Min =1.1pF		
Rest = 2.2pF	Rest = 2.4pF	≈256Hz	294Hz
Max = 3pF	Max = 3.7pF		

Table 6-3 – Capacitance and resonant frequency measurements and calulations for bi-stable devices

$C_{calculated}$	$C_{measured}$	$f_{measured}$	$f_{calculated}$
Min = 4.2pF	Min = 4.8pF	≈480Hz	652Hz
Rest = 8pF	Rest = 7pF		

Max = 11.9pF	Max = 9.25pF

The output voltage from the bi-stable converter circuit closely matches that of the simulated values presented in chapter 4. With four MEMS devices in parallel, an output voltage of 35.4V is obtained which is comparable to the simulated value of 36V. The efficiency of this circuit is very low (<1%). It is not practical to consider the effect of increasing the load resistance, as it is not possible to measure the output when the load resistance is higher than the resistance of the measurement equipment. The current will drain through the measurement equipment.

Higher voltage and efficiency levels would be possible if the variable capacitance levels were to increase; this was also shown in chapter 4. In order to increase the capacitance level of the devices, the structure and/or the number of capacitor electrodes needs to be modified. In the case of altering the structure of the electrodes, by increasing the minimum overlap gap between electrodes the capacitance level will increase with a reduction in parasitic fringing field capacitance. This modification will result in larger comb drives, however, it is a more practical solution than to simply increase the number of comb fingers to boost capacitance as this does not address the issue of parasitic capacitance. This increase in capacitor area would require an increase in actuator area to generate a larger actuating force.

In an attempt to generate a larger actuating force from a relatively small actuator area, an electrostatic zipping actuator was considered over the original parallel plate design. This modified bi-stable device, featured a curved electrode actuator and the test results are presented in this chapter. Unfortunately, this did not exhibit the desired pull in effect expected. The electrodes pull in at the tip (small gap) for a low voltage (≈10V). As the voltage is increased to ≈17V, the electrode pulls in at the clamped end (large gap). The actuator action can be attributed to the geometry of the electrodes. It was not possible to simulate the zipping action of the actuator prior to design and therefore this design was developed on a “trial and error” basis.

It was not possible to measure the output voltage of the resonant devices. The capacitance level was too low to measure the output using standard measurement equipment i.e. oscilloscope probe. The current would leak through the measurement probe rather than

charge the load capacitor. An attempt was made to measure the output using a Labworks vibration simulator and, as expected, there was no multiplication of the input voltage.

A modified resonant device was designed; however, as mentioned in chapter 5 of this thesis, this device was not successfully fabricated due to absence of a DRIE facility at Southampton at this stage in the project. Therefore it was not possible to carry out any testing on this

Chapter 7 Conclusions and Future Work

7.1 Conclusions

MEMS voltage converters for static and resonant energy harvesting applications have been presented and analysed. These devices are designed to mechanically amplify the output voltage of energy harvesting systems to meet the voltage requirements of their intended application systems e.g. sensor devices. A solar cell harvester was taken to be the energy harvesting system supplying the static MEMS converter, while a vibration energy harvester provided the supply voltage to the resonant MEMS converter.

The static converter assumed a constant DC input voltage of 24V which is a typical output of a solar panel setup. This voltage was then converted into two non-overlapping square wave signals using an oscillator circuit. These square wave signals powered the MEMS actuator and capacitor. The frequency of the square waves was designed to match the resonant frequency of the MEMS device for maximum power transfer.

The VIBES vibration energy harvesting system presented in [33] was considered to be the target supply for the resonant converter device. This harvester produces 428mV and 58mW in an ambient acceleration of $3.7ms^{-2}$ at 120Hz. This provides the ambient specification for the design of the resonant device.

In addition to the two core converter devices thesis, the bi-stable and resonant devices, a modified variation of each device is also presented. The modified bi-stable device features “curved” electrode actuator fingers. Ideally these devices would pull-in at the small tip gap between electrode plates, at a low voltage. This would then create a ripple pull-in effect along the beam. This is known as a zipping actuator. The modified resonant device was designed to address some of the design issues associated with the original resonant device, in particular, the low capacitance level. The modified devices feature a greater number of capacitor electrodes and integrated MEMS switches.

The devices were designed using a dicing-free SOI process developed at the University of Southampton's Nano Fabrication Centre. They were then evaluated in terms of structural characteristics (e.g. resonant frequency, topography) and performance when integrated with the control circuit. For four bi-stable devices in parallel, a maximum output voltage of 35.4 V was obtained for an input voltage of 24V.

No performance results exist for the resonant device, beyond the resonant frequency and capacitance variation. The capacitance level of this device was too low (2-4pF) that the load capacitor cannot retain any charge and it all dissipates through the load resistor. However, capacitance variation and resonant frequency results proved to be a close match to the simulated values. It was also not possible to evaluate the modified resonant device as fabrication was not completed on this round of devices due to faulty cleanroom equipment.

For the modified bi-stable device, a test was conducted to evaluate the behaviour of the zipping actuator. It was unknown whether this would yield a successful result as these devices were not simulated prior to fabrication. Unfortunately, these devices did not produce the desired actuator motion. Rather than a single pull-in action for a relatively low voltage, pull-in occurs in two stages; at the small tip gap for a low voltage (5-10V) and at the large end gap for a higher voltage (15-20V).

The main issues with the performance of the MEMS devices are parasitic capacitances and leakage currents. The parasitic capacitance of the capacitor's fringing fields cause substantial attenuation in the maximum achievable multiplication factor. This parasitic capacitance can be reduced by increasing the overlap distance between electrodes for the comb capacitor. By increasing these dimensions, however, the actuator must also increase to compensate for the increased electrostatic forces. This will result in a much larger end device. The devices were designed to feature a multiplication factor of M = 5, but measurement shows that, in the case of the bi-stable device, parasitic capacitances reduce this to M = 2.125.

For all the devices presented, another issue exists with regards to current leaking through the load resistor. For this reason, this circuit would operate well using an intermittent load whereby the circuit would slowly charge an external capacitor/battery and this would be used to intermittently power the target application device. Alternatively, the design of the MEMS capacitor can be rectified in further designs by increasing the dimensions of the comb structure to allow for a greater capacitance level. This was proved by cascading multiple capacitors in parallel to reduce the effect of the leakage. Simulations show that if the

capacitance level were to increase, the output voltage would increase exponentially until the maximum output (≈60 V) is reached for this design. This is the maximum achievable output that is set by the multiplication factor.

7.2 Future Work

The immediate future work for this project would be to re-design the MEMS devices to exhibit a higher level of variable capacitance. This can be achieved by altering the dimensions of the capacitor electrodes. For example, by increasing the electrode overlap and decreasing the gap between electrodes, the effects of parasitic capacitance can be significantly reduced. A higher capacitance level would result in a better multiplication factor, a higher output voltage and a higher electrical efficiency level. Other design techniques such as MEMS interconnects could prove to be an interesting solution to achieving high capacitance levels for lower volume devices.

Improving the curved electrode design for the actuator in the bi-stable device would be another interesting avenue for future research. If this design were to be optimised, the actuator would offer larger ranges of displacement for lower input voltages. This would help to improve the electrical efficiency of the system by requiring less power to actuate the capacitor electrodes. The current challenges for this design are with the simulation software. For the curved devices presented in this thesis, it was not possible to simulate the motion of the curved actuator under an applied voltage as the FEM software could not process the mesh. This lead to a “trial and error” approach towards the design and fabrication of the devices.

Continuing the development work of the modified resonant converter could also yield some interesting results in the future, in particular, these devices would be the most obvious choice of converters to integrate directly with a vibration energy harvesting system. Again, this device could benefit from a higher capacitance level in order to achieve a reasonable output voltage without cascading multiple devices in parallel. These devices have the potential to achieve the highest levels of electrical efficiency compared with any current voltage multiplier circuit. This is due to the use of integrated MEMS switches and lack of an electrostatic actuator unit.

This work could then progress to integration of the MEMS variable capacitor and control circuit with an energy harvesting unit. This may present some challenges with impedance matching, frequency matching etc. but would serve as the foundation work to a fully integrated solution for resonant based energy harvesting units, where the MEMS variable capacitor could be designed on the same silicon as the harvesting device.

References

[1] K. Martinez and J. K. Hart, “Glaciers monitoring: deploying custom hardware in harsh environments.” *Wireless Sensor Networks - Deployments and Design Framework*, Springer. Chapter 9, 2010.

[2] J. A., Paradiso and T. Starner. "Energy scavenging for mobile and wireless electronics." *Pervasive Computing, IEEE* , pp. 18-27, 2005.

[3] R. J. M. Vullers, R. Van Schaijk, I. Doms, C. Van Hoof and R. Mertens. "Micropower energy harvesting." *Solid-State Electronics,* vol. 53, pp. 684-693, 2009.

[4] M. Marzencki, Y. Ammar and S. Basrour. "Integrated power harvesting system including a MEMS generator and a power management circuit." *Sensors and Actuators A: Physical* pp. 363-370, 2008.

[5] R. Torah, P. Glynne-Jones, M. Tudor, T. O'Donnell, S. Roy and S. Beeby, “Self-powered autonomous wireless sensor node using vibration energy harvesting.” *Measurement science and technology*, vol. 19, 2008

[6] T. Becker, M. Kluge, J. Schalk, T. Otterpohl and U. Hilleringmann, “Power management for thermal energy harvesting in aircrafts” *IEEE Sensors 200,* pp. 681-684, 2008.

[7] M. AbdElFattah, A. Mohieldin, A. Emira, and E. Sanchez-Sinencio. "A low-voltage charge pump for micro scale thermal energy harvesting." *2011 IEEE International Symposium on Industrial Electronics (ISIE),* pp. 76-80. 2011.

[8] G. Palumbo and D. Pappalardo. "Charge pump circuits: An overview on design strategies and topologies." *IEEE Circuits and Systems Magazine,* vol. 10, pp. 31-45, 2012

[9] J. Bernstein, "An overview of MEMS inertial sensing technology", *Sensors*, vol. 20, pp.14 -21, 2003

[10] C. Haas, "Modelling and analysis of a MEMS approach to a voltage step-up conversion." *J. Micromech. Microeng.,* vol. 14, pp. 114-22, 2003.

[11] S.Ghandour, G. Depesse and S. Basrour, "Theoretical analysis of a new MEMS approach to build a high efficiency fully integrated DC-DC converter." *MME 2009 Conference Paper,* 2009.

[12] C. O' Mahoney and M. Hill, "Modelling and performance evaluation of a MEMS DC/DC convertor". *J. Micromech. Microeng.,* vol. 16, pp. 149-55, 2006.

[13] L. Li, M. Begbie and D. Uttamchandani, "Single-input, dual-output MEMS DC/DC converter" *Electronics Letters,* vol. 43, no.15, 2007.

[14] P. Glynne-Jones and N. M. White. "Self-powered systems: a review of energy sources." *Sensor review* vol. 21, pp. 91-98, 2001.

[15] S.B Riffat and X. Ma, "Thermoelectrics: a review of present and potential applications", *Applied Thermal Engineering*, vol. 23, pp. 913-935, 2003.

[16] M. D. Rowe, G. Min, S. G. Williams, A. Aoune, K. Matsuura, V. L. Kuznetsov, and L. W. Fu. "Thermoelectric recovery of waste heat-case studies." *1997 Proceedings of the 32nd Intersociety Energy Conversion Engineering Conference,* pp. 1075-1079, 1997.

[17] L. E. Bell, "Cooling, heating, generating power, and recovering waste heat with thermoelectric systems." *Science*, pp. 1457-1461, 2008.

[18] Z. Hadas, V. Singule, S. Vechet and C. Ondrusek, "Development of energy harvesting sources for remote applications as mechatronic systems," *2010 14th International Power Electronics and Motion Control Conference* , pp. 13-19, 2010

[19] T. Caillat, J. P. Fleurial, G. Synder, A. Zoltan, D. Zoltan, and A. Borshchevsky. "A new high efficiency segmented thermoelectric unicouple." *34th Intersociety Energy Conversion Engineering Conference*. 1999.

[20] M. A. Green, K. Emery, Y. Hishikawa, W. Warta and E. D. Dunlop. "Solar cell efficiency tables (version 39)." *Progress in photovoltaics: research and applications* vol. 20, pp. 12-20, 2012.

[21] S. Chalasani and J.M. Conrad, "A survey of energy harvesting sources for embedded systems," *IEEE Southeastcon 2008*, pp.442-447, 2008

[22] R. S. Ohl "Light-sensitive electric device." U.S. Patent 2,402,662, issued June 25, 1946.

[23] B. M. Kayes, H. Nie, R. Twist, S. G. Spruytte, F. Reinhardt, I. C. Kizilyalli and G. S. Higashi. "27.6% conversion efficiency, a new record for single-junction solar cells under 1 sun illumination." *2011 37th IEEE Photovoltaic Specialists Conference (PVSC)*, pp. 4-8, 2011.

[24] L. Wuhua and H. Xiangning, "Review of nonisolated high-step-up DC/DC converters in photovoltaic grid-connected applications," *IEEE Transactions on Industrial Electronics,* vol.58, pp.1239-1250, 2011

[25] J. E. Nordholt , D. T. Young and H. O. Funsten, “Plasma experiment for planetary exploration (PEPE) on DS1” *IEEE Aerospace Conference Proceedings,* vol.7, pp.597–607, 2000

[26] P. Glynne-Jones, S. P. Beeby and N. M. White. "Towards a piezoelectric vibration-powered microgenerator." *IEE Proceedings-Science, Measurement and Technology* vol. 148, pp. 68-72, 2001.

[27] H. A. Sodano, D. J. Inman and G. Park. "A review of power harvesting from vibration using piezoelectric materials." *Shock and Vibration Digest,* vol. 36, pp. 197-206, 2004

[28] S. R. Anton, and H. A. Sodano. "A review of power harvesting using piezoelectric materials (2003–2006)." *Smart Materials and Structures* vol. 16, 2007

[29] S. Saadon and O. Sidek. "A review of vibration-based MEMS piezoelectric energy harvesters." *Energy Conversion and Management* vol. 52, pp. 500-504, 2011

[30] S. Roundy and P. K. Wright. "A piezoelectric vibration based generator for wireless electronics." *Smart Materials and Structures,* vol. 13, pp. 1131, 2004.

[31] C.B. Williams and R.B. Yates, "Analysis of a micro-electric generator for microsystems" *Sensors and Actuators A,* vol. 52, pp. 8-11, 1996.

[32] C. R. Saha, T. O'Donnell, H. Loder, S. Beeby and J. Tudor, "Optimization of an electromagnetic energy harvesting device" *IEEE Transactions on Magnetics,* vol. 42, pp. 3509-11, 2006.

[33] S. Beeby, R. Torah, M. Tudor, P. Glynne-Jones, T. O'Donnell, C. Saha and S. Roy, "A micro electromagnetic generator for vibration energy harvesting." *J. Micromech. Microeng,* vol. 17, pp. 1257-65, 2007.

[34] S. Kulkarni, E. Koukharenko, R. Torah, J. Tudor, S. Beeby, T. O'Donnell and S. Roy, "Design, fabrication and test of integrated micro-scale vibration-based electromagnetic generator." *Sensors and Actuators A,* vol. 145, pp. 336-42, 2008.

[35] D. Zhu, S. Roberts, M. J. Tudor and S. P. Beeby. "Design and experimental characterization of a tunable vibration-based electromagnetic micro-generator." *Sensors and Actuators A: Physical* vol. 158, pp. 284-293, 2010.

[36] S. Meninger, J. O. Mur-Miranda, R. Amirtharajah, A. Chandrakasan and J. Lang, "Vibration-to-electric energy conversion." *IEEE Trans. Very Large Scale Integr. (VLSI) Syst.,* vol. 9, pp. 64-76, 2001.

[37] S. Roundy, P. K. Wright and K. S. J. Pister, "Micro-electrostatic vibration-to-electricity converters" " *IMECE2002 Conf. Proc.,* 2002.

[38] B. C. Yen and J. H. Lang, "A variable capacitance vibration-to-electric energy harvester." *IEEE Trans. Circuits Syst.,* vol. 53, pp. 288-95, 2006.

[39] Y. Chiu, C. T. Kuo and Y. S. Chu, "MEMS design and fabrication of an electrostatic vibration-to-electricity energy converter." *Microsyst. Technol.,* vol. 13, pp. 1663-9, 2007.

[40]A. Mahmood Paracha, P. Basset, D. Galayko, A. Dudka, F. Marty and T. Bourouina, "MEMS DC/DC converter for 1D and 2D vibration-to-electricity power conversion." *IEEE Transducers 2009 Proc.,* 2009.

[41] S. Priya and D. J. Inman. *Energy harvesting technologies*. Springer, pp. 24, 2008.

[42] E. Lefeuvre, D. Audigier, C. Richard and D. Guyomar, "Buck-Boost converter for sensorless power optimization of piezoelectric energy harvester," *IEEE Transactions on Power Electronics*, vol.22, pp.2018-2025, 2007

[43] K. Kobayashi, H. Matsuo and Y. Sekine, "Novel solar-cell power supply system using a multiple-input DC–DC converter," *IEEE Transactions on Industrial Electronics,* vol.53, pp.281-286, 2006

[44] E. J. Carlson, K. Strunz, and B. P. Otis. "A 20 mV input boost converter with efficient digital control for thermoelectric energy harvesting." *IEEE Journal of Solid-State Circuits,* vol.45, pp.741-750, 2010

[45] X. Cao, W. J. Chiang, Y. C. King and Y. K. Lee. "Electromagnetic energy harvesting circuit with feedforward and feedback DC–DC PWM boost converter for vibration power generator system." *IEEE Transactions on Power Electronics,* vol.22, pp.679-685, 2007.

[46] J. F. Dickson, "On chip high-voltage generation in MNOS integrated circuits using an improved voltage multiplier technique." *IEEE J. Solid-State Circuits,* vol. SC-11, pp. 374-378, 1976.

[47] L. Pylarinos, "Charge pumps: an overview", *University of Toronto tutorial paper*, http://citeseerx.ist.psu.edu/viewdoc/summary?doi=10.1.1.128.4085

[48] A. Anil and R. K. Sharma. "A high efficiency charge pump for low voltage devices." *International Journal of VLSI Design & Communication Systems* vol.3, pp.3, 2012

[49] J. S. Witters, G. Groeseneken and H. E. Maes, "Analysis and modelling of on-ship high-voltage generator circuits for use in EEPROM circuits" *IEEE J. Solid-State Circuits,* vol. 24, pp. 1372-80, 1989.

[50] J. T. Wu and K. L. Chang, "MOS charge pumps for low-voltage operation" *IEEE J. Solid-State Circuits,* vol. 33, pp. 592-7, 1998.

[51] K. Phang, "CMOS optical preamplifier design using graphical circuit analysis" *University of Toronto PhD thesis,* 2001.

[52] P. Favrat, P. Deval and M. J. Declercq, "A high-efficiency CMOS voltage doubler." *IEEE J. Solid-State Circuits,* vol. 33, no. 3, pp. 410-16, 1998.

[53] T. C. Huang, F. M. Hsu and P. C. P. Chao, "An energy harvesting system with a novel rectifier charge pump" *IEEE Sensors Conf. Proc.*, 2011.

[54] M. Marzencki, Y. Ammar and S. Basrour, "Integrated power harvesting system including a MEMS generator and power management circuit" *Sensors and Actuators A,* vol. 145-146, pp. 363-70, 2008.

[55] Ultralow voltage step-up converter and power manager LTC3108, *Linear Technology*, Milpitas, CA, 2010.

[56] J. M. Noworolski and S. R. Sanders, "An electrostatic micro-resonant power conversion device" *IEEE Power Electronics Specialists Conf.,* vol. 2, pp 997-1002, 1992.

[57] J.M. Noworolski, "Micromechanical power conversion." *University of California at Berkeley, PhD Thesis,* 1998.

[58] B. Otis and R. Lu, "A single mask SOI mechanical voltage pump." *University of California at Berkeley, EE245 Class Project,* 2001.

[59] C. Haas and M. Kraft, "Design study of MEMS voltage converters" *Tripartite Diplomarbeit Thesis,* University of Southampton, 2003.

[60] A. Chaehoi, D. Weiland, M. Begbie, S. Scherner and C. Welham, "MEMS DC/DC converter: a detailed CMOS mechanical co-simulation" *Smart Systems Integration Conf.,* paper. 36, 2011.

[61] S.Ghandour, G. Depesse and S. Basour, "Design and control of a zero voltage switching MEMS DC-DC power converter." *NSTI-Nanotech,* vol. 2, pp 352-5, 2010.

[62] Quad/Dual N-channel zero threshold EPAD matched pair MOSFET array ALD110800/ALD110800A/ALD110900/ALD110900A, *Advanced Linear Devices Inc.*, Sunnyvale, CA, 2005.

[63] P. D. Grant, R. R. Mansour and M. W. Denhoff, "A comparison between RF MEMS and semiconductor switches" *Can. J. Elect. Comput. Eng.,* vol. 27, pp 33-9, 2002.

[64] G.M. Rebeiz, "RF MEM: Theory, design and technology." *Wiley-Interscience,* 2003.

[65] G.M. Rebeiz, "RF MEMS switches: Status of the technology" *12th Int. Conf. on Solid State Sensors, Actuators and Microsystems,* pp. 1726-29, 2003.

[66] J. B. Muldavin and G.M. Rebeiz, "Nonlinear electro-mechanical modelling of MEMS switches" *IEEE MTT-S Int. Microwave Symp. Dig.,* pp. 2119-122, 2001.

[67] R.E. Mihailovich, M. Kim, J.B. Hacker, E.A. Sovero, J. Studer, J.A. Higgins, and J.F. DeNatale, "MEM relay for reconfigurable RF circuits," *IEEE Microwave Wireless Comp. Lett.*, vol. 11, pp. 53-55, 2001.

[68] W. D. Groot, D. Felnhofer, and E. Gusev, "Reliability aspects of capacitve MEMS devices" *Proc. Eurosensors XXV.,* 2011.

[69] G. L. Tan and G. M. Rebeiz, "A DC-contact MEMS shunt switch," *IEEE Microwave Wireless Comp. Lett.*, vol. 12, pp. 212–14, 2002

[70] J. B. Muldavin and G. M. Rebeiz, "All-metal high-isolation series and series/shunt MEMS switches," *IEEE Microwave and Wireless Components Lett*, vol. 11, pp. 373-75, 2001

[71] RF MEMS switch 2SMES-01, *Omron Electronic Components LLC*, Schaumburg, IL, 2009.

[72] SPST, RF MEMS switches, *Radant MEMS*, Stow, MA, Available: http://www.radantmems.com/radantmems/products.html

[73] H. Cai, Z. Yang, G. Ding and H. Wang, "Development of a novel MEMS inertial switch with a compliant stationary electrode," *IEEE Sensors J.,* vol. 9, no. 7, pp.801–808, 2009.

[74] Z. Yang, G. Ding, H. Cai, and X. Zhao, "A MEMS Inertia Switch With Bridge-Type Elastic Fixed Electrode for Long Duration Contact," *IEEE Trans. Electron Devices,* vol. 55, pp. 2492–2497, 2008.

[75] Y. Chiu and V. F. G. Tseng, "A capacitive vibration-to-electric energy converter with integrated mechanical switches," *J. Micromech. Microeng.,* vol. 18, 104004, 2008.

[76] S. Beeby, G. Ensell, M. Kraft and N. White, "MEMS mechanical sensors" *Archtech House MEMS library,* pp.104-105, 2004.

[77] R. Legtenberg, A. W. Groeneveld and M. Elwenspoek, "Comb-drive actuators for large displacements." *J. Micromech. Microeng.,* vol. 6, pp. 320-9, 1996.

[78] B. Zhang and D. Fang, "Modelling and modification of the parallel plate variable MEMS capacitors considering deformation issue." *Mechanism and Machine Theory,* vol. 44, pp. 647-55, 2009.

[79] Y. Cho, B. M. Kwak, A. P. Pisano ad R. T. Hoew, "Slide film damping in laterally driven microstructures", *Sensors and Actuators A,* pp. 31-39, 1994.

[80] W. S. Griffin, H. H. Richardson and S. Yamanami, "A study of fluid squeeze-film damping", *J. Basic Engineering*, pp. 451–6, 1966

[81] J. J. Blech, "On isothermal squeeze films", *J. Lubrication Tech.*, vol. 105, pp. 615-20, 1983

[82] H. Sumali, "Squeeze-film damping in the free molecular regime: model validation and measurement on a MEMS" *J. Micromech. Microeng*., vol. 17, pp. 2231–40, 2007

[83] L. Mol, L. A. Rocha, E. Cretu and R. F. Wolffenbuttel, "Squeezed film damping measurements on a parallel-plate MEMS in the free molecular regime" *IEEE Transducers 2009 Proc*, pp. 1425–8, 2009

[84] Y. Dong, "Control systems for capacitive micromachined inertial sensors with high-order sigma-delta modulators" *University of Southampton PhD Thesis*, pp. 135–50, 2009

[85] Simscape Manuals, The Mathworks Inc, http://www.mathworks.co.uk/ , 2013

[86] MEMS+ 2.1 Manual, Coventor Inc, http://www.coventor.com/, 2011

[87] Conventorware Manual, Coventor Inc., http://www.coventor.com/, 2003

[88] R. Legtenberg, J. Gilbert and S. D. Senturia, "Electrostatic curved electrode actuators", *IEEE J. Microelectromech. Syst.,* vol. 6, no.3, pp. 257–265, 1997.

[89] J. Li, M. P. Brenner, T. Christen, M. S. Kotilainen, J. H. Lang and A. H. Slocum, "Deep-reactive ion-etched compliant starting zone electrostatic zipping actuators" *J. Micromech. Microeng*., vol. 14, pp. 1283–1297, 2005

[90] N. Dhaubanjar, S. M. N. Rao, Y. Cai, D. Popa, M. Chiao and J. C. Chiao, "A cantilever-type electrostatic zipping actuator", *SPIE Int. Smart Materials, Nano- & Micro-Smart Systems Symp., Smart Structures, Devices, and Systems Conf. Proc.*, 2006.

[91] I. Zeimpekis-Karakonstatinos, "Mechanical amplification in inertial sensors." *University of Southampton, nine month progress report,* 2008.

[92] T. Overstolz, P. A. Clerc, W. Noell, M. Zickar, and N. F. de Rooij, "A clean wafer-scale chip-release process without dicing based on vapor phase etching," *Proc. 17th IEEE Int. Conf. Micro Electro Mech. Syst.*, pp. 717–720, 2004.

[93] Y. Matsumoto, M. Nishimura, M. Matsuura and M. Ishida, "Three-axis SOI capacitive accelerometer with PLL C-V converter", *Sensors and Actuators A,* pp. 77-85, 1999.

[94] Y. Hsu, J. Chen, H. Chien, S. Chen, S. Lin and L. Liao, "New capacitive low-g triaxial accelerometer with low cross-axis sensitivity", *J. Micromech. Microeng.,* vol. 14, pp. 1083-90, 2004.

[95] I. Sari, I. Zeimpekis and M. Kraft, "A full wafer dicing free dry release process for MEMS devices", *Proc. Eurosensors XXIV.,* 2010.

[96] O. Raccurt, F. Tardif, F. A. d'Avitaya, and T. Vareine, "Influence of liquid surface tension on stiction of SOI MEMS," *J. Micromech. Microeng*., vol. 14, pp. 1083–1090, 2004

[97] E. P. Van De Ven, I. W. Connick and A. S. Harrus, “Advantages of dual frequency PECVD for deposition of ILD and passivation films”, *Proc. 7th IEEE Int. Conf. VMI,* pp.194-201, 1990

[98] S. K. De and N. R. Aluru, "Full-Lagrangian schemes for dynamic analysis of electrostatic MEMS," *J. Microelectromechanical Systems*, vol. 13, pp. 737-758, 2004.

Appendix A: Matlab Code

A.1 Bi-stable Design

```
% CORE DESIGN
clear
%---Constants---%
t = 50e-6                          %Thickness of structural silicon layer
Ds=2331                            %Density of silicon in Kg/m^3
E= 1.69e11                         %Young's Modulus in Pa
e0= 8.854*10^-12                   %permitivity of free space
mu = 1.86e-5                       %effective dynamic viscosity of air
Vin = 24                           %input voltage


%----Gaps-----%
M=5                                %multiplcation factor
gmin =7e-6                         %mininum gap
gmax = M*gmin                      %maximum gap
g0 = (gmax-gmin)/2+gmin            %gap at rest
ga = 3e-6                          %gap between rotor and stator fingers


%----Spring Dimensions------%
b2w = 7e-6
b1w = 25e-6
b2lb = 1200e-6
b2lt = 1000e-6
b2lx1 = b2lt-b1w
b2lx2 = b2lb-b1w
b1l = g0+b2w
end_length = 70e-6

%----Actuator Dimensions------%
finger_length=1000e-6       %length of actuator finger
finger_width=12e-6          %width of capacitor and actuator fingers
finger_spacing = g0+3*g0+2*finger_width
N_act = 60                  %number of actuator fingers

%----Capacitor Dimensions------%
comb_finger_width = 7e-6
cap_bar_width = 30e-6
cap_finger_length = 70e-6  %length of capacitor comb fingers
N = 880                    %number of capacitor comb fingers
num_cap_bars = 16
comb_segment_number = N/num_cap_bars
comb_bar_length = (comb_segment_number*(2*comb_finger_width+2*ga))

payload_width = 52.5e-6     %2*payload_width = width of main beam
stator_anchor = 130e-6      %width of capacitor stator anchor
```

```
tip_gap = 40e-6             %gap between main beam and capacitor fingers
act_cap_gap = 60e-6         %gap between actuator and capacitor

%----Capacitor Equations------%
min_cap = ((2*N*t*e0*(gmin))/ga)
max_cap = (2*N*t*e0*(gmax))/ga
rest_cap = (2*N*t*e0*(g0))/ga
Cp = 0;                     %parasitic capacitance;

%---Spring Constant---%
Kx1                                                                    =
4*E*t*((b2w/b2lx1)^3)*((b2lx1*b1w^3)+(b1l*b2w^3))/((b2lx1*b1w^3)+(4*b1l*b2w
^3));
Kx2                                                                    =
4*E*t*((b2w/b2lx2)^3)*((b2lx2*b1w^3)+(b1l*b2w^3))/((b2lx2*b1w^3)+(4*b1l*b2w
^3));
Kx = ((1/Kx1)+(1/Kx2))^-1

%------Area Calculation------%
finger_area=(finger_length)*finger_width
area_capacitor                                                         =
(num_cap_bars*((comb_bar_length+tip_gap)*cap_bar_width))+(N*comb_finger_wid
th*cap_finger_length)
area_actuator = finger_area*N_act
area_comb = area_capacitor+area_actuator
area_beam = 2*payload_width*(4346e-6)
spring_area = ((b2lb)*(b2w) + (b1l)*(b1w) +(b2lt)*(b2w) )*4
total_surface_area = area_comb+area_beam+spring_area

%------Mass Calculation------%
m = total_surface_area*t*Ds

%---Damping---%
cc = 2*sqrt(Kx*m)
c=t/finger_length;
P=(c^2/((c^2)+1))+(2*(c^2)/(9*((c^2)+9)))
D_actuator=N_act*0.8*0.895*(1.85e-5)*(t)*((finger_length/g0)^3)*P;
D_capacitor = (2.636507e-7/7)*N
D_total = D_actuator+D_capacitor

%------Various------%
omega = sqrt(Kx/m)
f = omega/(2*pi)            %resonant frequency of device
x1g = (m*9.8)/Kx            %displacement under gravity

%------Power+efficiency Calculations------%
Rin = 1/((min_cap+Cp)*(f))  %input resistanct
RL = 0:1e8:10e9             %load resistance
test = max(size(RL))

for i=1:test,
Vo(i) = ((M+(Cp/min_cap))*(RL(i)*min_cap*f/(RL(i)*(min_cap+Cp)*f+1))*Vin)
power_cap                                                              =
((Vo(i)^2)/RL(i))*((RL(i)*(min_cap+Cp)*f)/((RL(i)*(min_cap+Cp)*f)+1))
power_act = 0.5*((Vin^2)*(maximum_actuator_capacitance)*f);
pout(i) =((Vo(i)^2)*RL(i))/((RL(i)+Rin)^2)
efficiency(i) = (pout(i)/(power_cap+power_act))*100
end
```

```
subplot(2,1,1)
plot(RL, Vo, RL(high1), Vo(high1), 'rs')
xlabel('Load Resistance')
ylabel('Voltage (V)')
grid on
subplot(2,1,2)
plot(RL, efficiency, RL(high2), efficiency(high2), 'g^')
xlabel('Load Resistance')
ylabel('Efficiency (%)')
grid on
```

A.2 Resonant Design

```
% RESONANT DESIGN
clear
%---Constants---%
T = 50e-6                           %Thickness of structural silicon layer
Ds=2331                             %Density of silicon in Kg/m^3
E= 1.69e11                          %Young's Modulus in Pa
eps0= 8.854*10^-12                  %permittivity of free space
mu = 1.86e-5                        %effective dynamic viscosity of air
Vin = 0.5                           %input voltage

%---Gaps---%
gmin = 10e-6                        %minimum gap
gmax = 5*gmin                       %maximum gap
g0 = (gmax-gmin)/2+gmin             %rest gap
ga = 3e-6                           %gap between rotor and stator fingers

%---Spring dimensions---%
bw2 = 7e-6
bw1 = 25e-6
blb2 = 1600e-6
blt2 = 1450e-6
blx1 = blt2-bw1
blx2 = blb2-bw1
b1l = g0+bw2
end_length = 60e-6

%other dimensions
payload_width = 105e-6              %half width of central beam
tip_gap = 50e-6                     %gap between central beam and comb
hole_radius = 9e-6                  %perforation hole radius
mass_cap_gap = 200e-6               %gap between proof mass and capacitor

%----Capacitor Dimensions------%
finger_width=7e-6                   %electrode width
cap_finger_length = 70e-6           %electrode length
comb_bar_width = 30e-6              %width of comb beam
comb_bar_length = 1000e-6           %length of comb beam
num_cap_bars = 4                    %number of comb capacitor bars
comb_segment_number = comb_bar_length/(finger_width*2+ga*2)
num_capacitor =comb_segment_number*num_cap_bars

%----Capacitor Equations------%
min_capacitance = (2*num_capacitor*T*eps0*(gmin))/ga
max_capacitance = (2*num_capacitor*T*eps0*(gmax))/ga
rest_capacitance = (2*num_capacitor*T*eps0*(g0))/ga
M = max_capacitance/min_capacitance;
Cp = 3e-12;                         %parasitic capacitance

%---Spring Constant---%
Kx1                                                                    =
4*E*T*((bw2/blx1)^3)*((blx1*bw1^3)+(b1l*bw2^3))/((blx1*bw1^3)+(4*b1l*bw2^3)
);
```

```
Kx2                                                                    =
4*E*T*((bw2/blx2)^3)*((blx2*bw1^3)+(b11*bw2^3))/((blx2*bw1^3)+(4*b11*bw2^3)
);
Kx = ((1/Kx1)+(1/Kx2))^-1

%------Area Calculation------%
area_capacitor                                                         =
num_cap_bars*(((comb_bar_length+tip_gap)*comb_bar_width)+(comb_segment_numb
er*finger_width*cap_finger_length))
end1 = end_length*payload_width%-(3*pi*(hole_radius^2))
end2 = 560e-6*payload_width%-(3*16*pi*(hole_radius^2))
area_beam = end1+end1
spring_area = ((blb2)*(bw2)*2 + (b11)*(bw1)*2 +(blt2)*(bw2)*2 )*2
mass_width = 3300e-6
mass_length = 1200e-6
area_holes = 5124*pi*(hole_radius^2)
mass_area = (mass_width*mass_length)%-area_holes
surface_area = area_capacitor+area_beam+spring_area+mass_area

%------Mass and Frequency Calculation------%
m = surface_area*T*Ds                %mass of device
f = (1/(2*pi))*(sqrt(Kx/m))          %resonant frequency

%------Damping--------%
D = (3.34e-8)*num_capacitor

%------Acceleration under Gravity------%
x1g = (m*9.8)/Kx                     %displacement under gravity
a_ideal = ((20e-6)*Kx)/m             %acceleration needed for full motion

%------Power+efficiency Calculations------%
Rin = 1/((min_capacitance+Cp)*(f))   %input resistance
RL = 0:1e8:5e10                      %load resistance
test = max(size(RL))

for i=1:test,
Vo(i)                                                                  =
((M+(Cp/min_capacitance))*(RL(i)*min_capacitance*f/(RL(i)*(min_capacitance+
Cp)*f+1))*Vin)
power_cap                                                              =
((Vo(i)^2)/RL(i))*((RL(i)*(min_capacitance+Cp)*f)/((RL(i)*(min_capacitance+
Cp)*f)+1))
pout(i) =((Vo(i)^2)*RL(i))/((RL(i)+Rin)^2)
efficiency(i) = (pout(i)/(power_cap))*100
end

subplot(2,1,1)
plot(RL, Vo, RL(high1), Vo(high1), 'rs')
xlabel('Load Resistance')
ylabel('Voltage (V)')
grid on
subplot(2,1,2)
plot(RL, efficiency, RL(high2), efficiency(high2), 'g^')
xlabel('Load Resistance')
ylabel('Efficiency (%)')
grid on
```

A.3 Magnitude and Phase Calculation

```
%Matlab Magnitude and Phase plot generator from MSA-400 %frequency doubled
files
clear;
Num_files = 26;                      %number of individual frequency files
Starting_frequency = 90;
Ending_frequency = 140;
Increment =(Ending_frequency-Starting_frequency)/(Num_files-1)

%random variables
x=1;
End_position=0;
Start_position=0;
freq_add=0;


while x<=Num_files
Start_position = End_position+8;    %numbers start at 8th entry
End_position = Start_position+40;
Freq(x) = (Starting_frequency+freq_add)*2;
time(:,x)=xlsread('mixed.xlsx',sprintf('A%d:A%d',Start_position,End_positio
n));
output_wave(:,x)=xlsread('mixed.xlsx',sprintf('B%d:B%d',Start_position,End_
position));


f = Freq(x);
input(:,x) = sin((2*pi*f)*time(:,x));

[peak_input, index_input] = max(input,[],1);
[peak_output,index_output]= max(output_wave,[],1);
time_peak_input = time(index_input(x),x);
time_peak_output = time(index_output(x),x);
orig_Phase_diff(:,x)=((time_peak_output- time_peak_input)/(1/f))*360;
Phase_diff(:,x)= orig_Phase_diff(:,x);

Mag = 20*log10(peak_output);

if (Phase_diff(:,x) >180)
Phase_diff(:,x)= Phase_diff(:,x)-360;
if (Phase_diff(:,x) >180)
Phase_diff(:,x)= Phase_diff(:,x)-360;
end

elseif (Phase_diff(:,x) <-180)
Phase_diff(:,x)= Phase_diff(:,x)+360;
if (Phase_diff(:,x) <-180)
Phase_diff(:,x)= Phase_diff(:,x)+360;
end
end

Phase_diff(:,x)= Phase_diff(:,x);
freq_add=freq_add+Increment;
x=x+1;
```

```
end

subplot(2,1,1)
plot(Freq,Mag)
xlabel('Frequency (Hz)')
ylabel('Magnitude (dB)')
subplot(2,1,2)
plot(Freq,Phase_diff)
xlabel('Frequency (Hz)')
ylabel('Phase (°)')
```

Appendix B: Process Listing

Step	Process	Description	Remarks
1	Wafer clean	Fuming Nitric Acid: 15mins	
2	Wafer Dehydration	Bake @ 200ºC in oven: 30mins	
3	PECVD Oxide Deposition	Depositing $Si0_2$ Recipe Table Temperature: 350 ºC RF Power: 20W Pressure: 1000mTorr SiH_4: 4.2 N_20: 350 Time: 20min	Measure thickness of oxide layer (≈1µm)
4	Photolithography Front Side Mask	Ti Prime: spin 20sec @3krpm Softbake: 2min @ 120ºC on a hotplate AZ9260: spread 7sec @500rpm, spin 60sec @4krpm Soft bake: 2.5min @ 110ºC on a hotplate Expose: EVG620TB 20mW/cm^2 9sec Vacuum contact Develop: AK400Z:DI 3:1 2min	
5	ICP Etching of PECVD $Si0_2$	Recipe Temperature: 15ºC Pressure: 7mTorr RF Power: 100W ICP Power: 1500W Time: 7min	Measure thickness of remaining oxide layer (>20nm).
6	Remove frontside	Recipe	

	photoresist (PR) in O_2 plasma asher	O2: 600ml/min Power: 800W Time 10min	
7	Wafer clean	Fuming Nitric Acid: 15mins	
8	Photolithography Back Side Mask	Dehydration Bake @ 200ºC: 30mins Ti Prime: spin 20sec @3krpm Softbake: 2min @ 120ºC on a hotplate AZ9260: spread 7sec @500rpm, spin 60sec @2.4krpm Soft bake: 3min @ 110ºC on a hotplate Expose: EVG620TB 20mW/cm^2 12sec Vacuum contact Develop: AK400Z:DI 3:1 2.5min	
9	DRIE backside (STS™)	Target Depth: 400µm to buried oxide layer Recipe Etch Passivation C4F8: - 200sccm SF6: 450sccm - O2: 45sccm - Coil Power: 2800W 2000W Platen Power: 35W 20W Time: 45mins	High Frequency Platen Generator
10	Remove backside photoresist (PR) in O_2 plasma asher	Recipe O2: 600ml/min Power: 800W Time 10min	
11	DRIE frontside (STS™)	Target Depth: 50µm to buried oxide layer Recipe Etch Passivation	Low Frequency Platen Generator

		C4F8: 30sccm 250sccm SF6: 390sccm - O2: 39sccm - Coil Power: 2800W 2000W Platen Power: 40W - Time 18mins	
12	HF VPE Release	48% HF Vapour Temperature: 40ºC Time:4x20mins with 20min cool down periods in between etching.	
Bonding			
13	Apply adhesive to PCB	Place carrier wafer on hotplate @70ºC. Place 1x1cm2 PCB face-up on carrier wafer. Brush on a layer of crystal bond to the surface of the PCB.	
14	Bonding	Manually place device into centre of the PCB bonding surface. Remove from hotplate and allow PCB to cool.	
15	Wire Bond	Wire bond device electrodes to PCB pads using 25µm thick Aluminium Silicon wire.	

Appendix C: Journal Paper

Journal of Micromechanics and Microengineering proof paper attached.